

Mathematical modelling of biophysical dynamics of nanoparticle interaction with T-Cells

Shalon (Shang Wan) Liu

Master of Science

Department of Mathematics & Statistics

McGill University

Montreal, Quebec

2015-07-13

A thesis submitted in partial fulfillment of the requirements of the degree of
Masters of Science at McGill University

Copyright © Shalon (Shang Wan) Liu 2015

DEDICATION

For my mom, whose hard work and sacrifices
made it possible for me to complete this dissertation.

ACKNOWLEDGEMENTS

I would like to first thank my supervisor Dr. Anmar Khadra for the helpful discussions and suggestions about this work, for supporting me in pursuit of my goals and for pushing me to work harder. He introduced me to the field of mathematical biology and helping me realize my dream of combining my interests in both mathematics and immunology.

I would like to thank the following people: Dr. Russell Steele for accepting me in to the Master's program despite my questionable undergraduate record, continuing to support me throughout, Dr. Pere Santamaria from the University of Calgary who provided the experimental work this thesis is based on, Dr. Jean-Christophe Nave for being a part of my progress tracking committee and his efforts in trying to secure an instructor for the graduate level Nonlinear Dynamics course and everybody in the Khadra lab for all the help and discussions throughout the course of this project.

I am also grateful to Dr. J. Bruce White and Christopher Ing for setting me on the mathematical path in high school, without whom I would've never studied math.

Lastly, I would like to thank my friend Gabriela Stefanini for always being supportive and my boyfriend Calem Bendell, who never fails to make me laugh (ever).

Financial support for this dissertation was provided by FQRNT (Le Fonds de Recherche du Québec Nature et Technologies) and NSERC (National Sciences and Engineering Research Council of Canada) grant to Dr. Khadra

ABSTRACT

Type 1 diabetes (T1D) is an autoimmune disease whereby T-cells of the host's immune system recognize and selectively kill insulin-producing β -cells of the Islets of Langerhans in the pancreas. Treatment of this disease using nanoparticles (NPs) coated with multiple peptide-major histocompatibility complexes (pMHC) has been shown to effectively reverse disease progression in animal models by expanding cognate autoregulatory T-cells, a sub-population of T-cells arising from memory cells that kill antigen presenting cells (APCs) presenting β -cell specific autoantigens in the pancreatic lymph nodes. We use mathematical and computational approaches to optimize the activation and expansion of this population of autoregulatory T-cells in both *in vivo* and *in vitro* contexts. Our model of T-cell expansion showed that smaller NPs are more effective at increasing T-cell population size than larger NPs, but the effect of NP-valency (i.e. number of pMHC molecules on each NP) is rather minimal. Transmission electron microscopy revealed that interactions between T-cells and pMHC-coated NPs take place at two different levels: (i) a supramolecular structural level in which NPs bind to the T-cell receptors on the T-cells in a cluster formation, and (ii) an individual pMHC-TCR binding level equivalent to that of a generic ligand-receptor interaction. We have developed a Markov model to represent both the supramolecular clustering of NPs on T-cells, as well as the individual pMHC-NPs binding to the TCRs. Markov Chain Monte Carlo methods were used to fit the parameters of the model to experimental T-cell activation profiles and generate probability distributions

for these parameters. Analysis of the sampling distribution of the parameter space showed a functional relationship between the binding rate of NPs, pMHC valency, and size of NP clusters. It also revealed that there is a unique maximal NP binding rate to T-cells corresponding to a unique combination of cluster size and ligand density for each NP-size. These characterizations of pMHC-NP-TCR interactions and their stimulatory activities are key to optimizing the design of pMHC-NPs in therapeutic treatment of autoimmune diseases.

ABRÉGÉ

Le diabète de type 1 (DT1) est une maladie auto-immune par laquelle les cellules T du système immunitaire de l'hôte reconnaissent et sélectivement tuent les cellules bêta qui sont les productrices d'insuline des îlots de Langerhans dans le pancréas. Le traitement de cette maladie utilisant des nanoparticules (NP) qui sont recouvertes de plusieurs peptide-complexes majeur d'histocompatibilité majeur (pCMH) ont démontré l'inversion efficace l'avancement de la maladie dans des modèles animaux par l'expansion des cellules T autorégulatrices cognates, une sous-population de cellules T provenant de cellules mémoire qui tue les cellules présentatrices d'antigène (CPA), qui expriment des auto-antigènes spécifiques des cellules bêta, dans les ganglions lymphatiques du pancréas. Nous utilisons des approches mathématiques et computationnelles pour optimiser l'activation et l'expansion de cette population de cellules T autorégulatrices telles qu'observées *in vivo* et *in vitro*. Notre modèle d'expansion des cellules T a montré que les plus petites NP étaient plus efficaces pour augmenter la taille de la population des cellules T tandis que l'effet de valence (le nombre de molécules de pCMH sur chaque NP) était assez minimes. La microscopie électronique à transmission a révélé que les interactions entre les cellules T et les NP recouvertes de pCMHs existent à deux niveaux différents: (i) un niveau structural supramoléculaire dans lequel les NP sont liés à la surface des cellules T dans une formation d'un groupe, et (ii) un niveau nanoscopique où les pCMH sont individuellement liés aux TCR, qui est en effet une interaction générique de ligand-récepteur. Nous avons développé un

modèle de Markov pour représenter le regroupement supramoléculaire des NP sur les cellules T ainsi que les liaisons individuelles pCMH-NP au niveau des TCR. Nous avons utilisé les méthodes de Monte-Carlo par chaînes de Markov pour ajuster les paramètres du modèle à des profils expérimentaux d'activation des cellules T et pour générer des distributions de probabilité pour ces paramètres. L'analyse de la distribution d'échantillonnage de l'espace des paramètres a montré une relation fonctionnelle entre le taux de liaison des NP, la densité des pCMH, et la taille des groupes NP. De plus, nous avons trouvé qu'il y a un taux de liaison maximal des NP aux cellules T correspondant à une combinaison unique de la taille de groupe et de la densité de ligand pour chaque taille de NP. Ces caractérisations d'interaction pCMH-NP-TCR et les réactions stimulatoires qui en résultent sont cruciales pour optimiser la conception de pCMH-NP dans le traitement thérapeutique générique des maladies auto-immunes.

TABLE OF CONTENTS

DEDICATION	ii
ACKNOWLEDGEMENTS	iii
ABSTRACT	v
ABRÉGÉ	vii
LIST OF TABLES	xi
LIST OF FIGURES	xiii
1	Introduction	1
	1.1 Autoimmune diseases from a modeling perspective	1
	1.1.1 Modeling APCS	4
	1.1.2 Modeling T-cell dynamics	6
	1.2 Nanoparticle treatment of T1D	8
	1.2.1 T-cell expansion <i>in vivo</i>	9
	1.2.2 <i>in vitro</i> stimulation experiments	10
	1.3 Aims	12
2	Markov Chain Monte Carlo for parameter estimation	14
	2.1 Statistical approaches of estimation	14
	2.2 Numerical optimization	16
	2.2.1 Numerical MCMC algorithm	18
	2.3 Markov Chain Monte Carlo in differential equations models	20
	2.3.1 Example and usage	22
3	Model of <i>in vivo</i> T-cell proliferation	27
	3.1 Model development	27
	3.2 Parameter estimation	33
	3.3 Results	34

4	Model of <i>in vitro</i> activation	40
4.1	Model of cluster binding	40
4.1.1	IFN γ production kinetics	42
4.1.2	Activation kinetics of T-cells	44
4.2	Parameter estimation with data fitting	49
4.2.1	Error function	49
4.2.2	MCMC fitting results	51
4.3	Mathematical analysis	53
4.4	Correlations	55
4.4.1	Filtering parameters for lowest errors	58
4.4.2	Cluster binding rate and cluster size by valency	61
4.4.3	ec₅₀	62
4.5	Model of nanoparticle binding	65
4.5.1	NP binding rate	66
4.5.2	NP dissociation rate	73
4.6	Co-operativity	76
4.7	Other models	78
4.7.1	Model selection	80
5	Conclusion and Discussion	82
5.1	Future Considerations	84
5.1.1	Kinetic proof reading as a model of T-cell activation	84
5.1.2	Probability of activation	88
5.1.3	Estimation of number of nanoclusters	90
A	IFN γ production data	92
B	Code	94
B.1	Running MCMC Toolbox	94
B.2	Sum-of-square error function	94
B.3	DE model	95
	References	97

LIST OF TABLES

Table	page
2-1 Six simulated experiments on the growth of <i>Escherichia coli</i> in LB broth.	23
2-2 Modes of estimated parameters in the logistic model	24
3-1 Values of known parameters	32
3-2 Parameter values close to the median (50th percentile) and at the 90% confidence envelopes (between 5th percentile and 95th percentile).	34
4-1 Table showing the modes of the parameters corresponding to Eqs. (4.1) – (4.7) as determined by the MCMC toolbox.	53
4-2 Table of parameter estimates for fitting Eq. (4.31) to the joint distribution of k_1 and m in Fig. 4-9.	61
4-3 Table of parameter for fitting Eq. (4.32) to the ec_{50} from Table 4-2.	62
4-4 Table of parameter for fitting k_1 as a function of m and valency.	65
4-5 The maximum number of pMHC/cluster that can be attained when k_{on} is optimal along with the valency per NP that can achieve this maximum and the distance between pMHCs at that valency.	73
4-6 NP binding (k_{on}), unbinding (k_{off}) and dissociation rate (K_D) parameter values.	76
4-7 Comparison of model selection criteria AIC and BIC applied to serial digestion model and unsaturated digestion.	81
5-1 Estimates of E_{max} and EC_{50} based on kinetic proof reading model.	88

A-1 IFN γ produced by 2.5×10^5 T-cells/ml incubated <i>in vitro</i> with 20 nm radius NPs of various valency and dose for 48 hours corresponding to Fig. 1-4.	92
A-2 IFN γ produced by 2.5×10^5 T-cells/ml incubated <i>in vitro</i> with 14 nm radius NPs of various valency and dose for 48 hours corresponding to Fig. 1-4.	93

LIST OF FIGURES

<u>Figure</u>	<u>page</u>
1–1 Role of APC mediating anti- β cell autoimmune response adapted from Fig. 1B of [28] with permission.	5
1–2 Percentages of tetramer ⁺ splenic CD4 ⁺ T-cells in NOD mice treated with 8 nm diameter core NPs with different pMHC valencies and dose.	10
1–3 Transmission electron micrograph of T-cell after treatment with pMHC-NPs.	11
1–4 Amount of IFN γ produced by naïve splenic CD8 ⁺ T-cells from TCR-transgenic 8.3-NOD mice detected by ELISA after stimulation with cognate pMHC-NPs with 8 nm diameter core or 20 nm diameter core with different pMHC valencies and doses.	12
2–1 Distribution of estimated parameters r and k	24
2–2 Fitting the logistic model (solid line) to bacteria growth data (black dots). The grey bands represent confidence intervals with the darker colors representing higher confidence.	25
3–1 Model of T-cell proliferation <i>in vivo</i>	28
3–2 Schematics representing A) the estimation of the maximum number of NPs of radius r that fills a binding site of radius R and B) the contact area (red) between the spherical NP and the relatively flat surface of the T-cell surface.	30
3–3 The distributions of the estimated parameters: A) ε_1 B) ε_2 C) b_{on} D) $k = b_{on}/b_{off}$ and E) α from MCMC [22].	35

3-4	Model simulation of T-cell expansion as a function of NP dose graphed for various NP valency fitted to experimental data of proliferation from injection with 20 nm diameter NPs. The solid lines show the mean and the dotted lines are the 90% confidence envelope for each data series. The legend shows the color-coding employed to represent each valency level (v).	37
3-5	Model predictions of T-cell proliferations comparing stimulation by small 4 nm radius (gray) and large 20 nm radius (black) NPs at two valencies: A) 20 pMHCs per NP and B) 61 pMHCs per NP) . The solid lines show the mean and the dotted lines are the 90% confidence envelopes.	38
3-6	Autoregulatory CD4 ⁺ expansion potency of 8 nm core NPs compared to 20 nm diameter core NPs at similar valencies and dose.	39
4-1	Markov model of nanocluster serial binding and swallowing.	41
4-2	Quantifying the relationship between the number of activated IFN γ ⁺ T-cells following stimulation and the amount of IFN γ these cells excrete in the medium. Panel A) is a reproduction of Fig. 4b from Campbell et al. [6] used with permission from the publisher and B) is the same data displayed on a linear scale showing the equation of the best fitting trend line.	45
4-3	A) Fitting of T-cell activation using various concentrations of PMA, published in [7] (circles), to the model given by Eq. (2.16) (line). Graph shows the mean and standard deviation of 100 simulation using randomly drawn parameters from the stationary distribution. B) Distribution of estimated parameters κ , k , T and n	47
4-4	The output of the MCMC Toolbox showing the parameters sampled, starting points, their ranges, and priors. $\mathbf{N}(0, \mathbf{Inf})$ means the distribution is uniform.	51

4–5	Fitting the $\text{INF}\gamma$ data of Fig. 1–4 to model simulations. $\text{INF}\gamma$ production by T-cells stimulated with pMHC-NPs with radius A) , B) 14 nm and C) , D) 20 nm coated with various valencies were fitted to the model given by Eqs. (4.1) – (4.7), where B) and D) show the distributions of estimated parameters according to their respective NP-size. Panels A) and C) show mean and standard deviation of model predictions using 100 random draws from the parameter distributions depicted in B) and D) , respectively. . . .	52
4–6	Joint distributions A) k_1 and k_2 showing linearly correlation and joint distribution of B) k_1 and m	56
4–7	Joint distribution of k_1 and m according to several Markov chains obtained using one valency on A) 14 nm radius NP and C) 20 nm radius NP. The color of the dot indicates the relative error obtained at that particular parameter value. B) and D) show these chains obtained in panels A) and C) displayed on the same plot, respectively.	57
4–8	Distribution of error from MCMC fitting.	58
4–9	Fitting of Eq. (4.31) to the joint densities of k_1 and m displayed in Fig. 4–7. Panel A) and C) show the fitting (in red) to the Markov chains corresponding to pMHC-NPs of radius A) 14 nm and C) 20 nm. Panels B) and D) show the corresponding distributions of estimated parameters (L , ec_{50} for each NP valency, and the Hill coefficient n) for their respective NP-size.	60
4–10	Fitting of a decreasing Hill function with coefficient $n = 2$ to the ec_{50} of k_1 – m fitting of A) 14 nm radius NPs and B) 20 nm radius NPs.	62
4–11	Fitting of Eq. (4.31) to the joint distribution of k_1 , m and v . Panel A) and C) show fitting to pMHC-NPs of radius A) 14 nm and C) 20 nm. Panels B) and D) show the corresponding distributions of estimated parameters (L , E , b , c , and the Hill coefficient n) for their respective NP-size.	64

4–12	Model of NP-binding to T-cells in the process of forming a new cluster, depicted as a series of transitions representing single NP bindings within the Markov model of Fig. 4–1.	65
4–13	Numerical calculation of k_{on} using Eq. (4.37) for $m = 1, \dots, 250$ for A) 14 nm radius NP coated with with 54 (blue), 31 (red), 11 (yellow), and 8 (purple) pMHCs/NP and B) 20 nm radius NP coated with with 210 (blue), 61 (red), 13 (yellow), and 9 (purple) pMHCs/NP . Panels C) and D) show the number of pMHCs presented at each cluster ($pMHC_{max}$) when the optimal k_{on} is attained for NP of radius A) 14 nm and B) 20 nm.	70
4–14	Schematics of the estimation of distance between adjacent pMHCs on a NP. Panel A) visualizes the fraction of the NP surface associated with each pMHC as a spherical cap and panel B) shows that spherical cap as defined on a Cartesian axis.	71
4–15	The k_{on} and k_{off} rates of NP binding. The NP A) unbinding rate k_{off} as given by Eq. (4.59), and B) binding rate k_{on} used to calculate k_{off} according to Eq. (4.59) for each NP-size and valency. C) Dissociation constant $K_D = k_{off}/k_{on}$ of NP-binding for each NP-size and valency. D) Change in co-operativity as NP size and valency are varied according to Eq. (4.61).	75
4–16	Markov model of nanocluster unsaturated binding and swallowing.	78
4–17	Fitting the $INF\gamma$ data of Fig. 1–4 to model simulations. $INF\gamma$ production by T-cells stimulated with pMHC-NPs with radius A) , B) 14 nm and C) , D) 20 nm coated with various valencies were fitted to the model depicted by Fig. 4–16, where B) and D) show the distributions of estimated parameters according to their respective NP-size. Panels A) and C) show mean and standard deviation of model predictions using 100 random draws from the parameter distributions depicted in B) and D) , respectively.	79
5–1	Kinetic proof reading model of T-cell activation.	84
5–2	Fitting Hill functions with Hill coefficient $n = 1$ to <i>in vitro</i> stimulation data of T-cells using A) 14 nm radius NPs and B) 20 nm radius NPs	86

5-3	Behaviour of P_i based on Eq. (5.12).	89
5-4	Schematics of the NP-cluster binding to the membrane of T-cells as visualized by an EM image.	90

CHAPTER 1 Introduction

1.1 Autoimmune diseases from a modeling perspective

Predictive mathematical models of complex diseases, such as those involved in the development of autoimmune disorders, can help improve our understanding of the underlying physiological processes that lead to clinical manifestation of symptoms and direct development of therapeutic strategies. In autoimmune type 1 diabetes (T1D), T and B cells of the host's own immune system recognizes and selectively attacks the host's own tissue. In the human subjects as well as animal models such as the non-obese diabetic (NOD) mouse, up to 90% of the total insulin-secreting β -cell population in the pancreatic islets of Langerhans is destroyed by effector $CD4^+$ and cytotoxic $CD8^+$ T lymphocytes that infiltrate the islets [12, 43, 46, 50, 57], leading to deficiency in insulin secretion and elevated levels of glucose in diabetic individuals. In particular, $CD8^+$ T-cells can target β -cells directly to induce cell death.

T-cells recognize and react to foreign or, in the case of autoimmunity, self-antigens through antigen-specific interactions via T-cell receptor (TCR) with peptide-major histocompatibility complexes (pMHC) class I [41], expressed on the surface of all nucleated cells such as β -cells and recognized by $CD8^+$ T-cells, and class II [40], expressed only on professional antigen presenting cells (APCs) such as B-cells, macrophages, and dendritic cells which is recognized by $CD4^+$ T-cells.

In healthy individuals, the T-cell repertoire is carefully regulated through positive and negative selection in the thymus to respond against pathogen-derived foreign antigens and not those found naturally within the body. Negative selection, a process designed to kill T-cells recognizing self-antigen with high affinity [53], is an imperfect process that leaves some potential for autoimmunity in every person, yet not everyone develops autoimmunity [2]. Better understanding of T1D can provide some insights into other chronic autoimmune diseases.

Genetics is recognized to play a role in determining life-time susceptibility. However there is still a great amount of debate and uncertainty about the factors that trigger the clinical onset of T1D. The basic understanding for the development of T1D, first proposed by Eisenbarth [16], postulates that genetic background provides all individuals with some level of susceptibility to the disease. Exposure to environmental triggers such as certain viruses or foods leads to abnormal activation of the T-cell mediated adaptive and B-cell mediated humoral immune response in the pancreas. During T1D progression, autoreactive T-cells undergo a process of “avidity maturation” [1], defined as an increase in the avidity level of T-cells over the course of the autoimmune response, accompanied by a gain in pathogenic potential. Islet autoantibodies manufactured by mature B-cells have been able to serve as reliable surrogate predictive markers of clinical presentation of disease [30, 45, 61]. The presence of one or more type of antibody can precede the clinical onset by years or even decades, with increased titres or positivity of multiple antibodies corresponding to increased likelihood of hyperglycemia and progression to clinical disease[32].

The role of APCs such as macrophages in T1D development remains an outstanding question. Macrophages serve dual roles of phagocytosis of cellular debris following an immune reaction, and processing antigens in engulfed particles for presentation on class II MHC as well as class I MHC through cross presentation [5]. Defects in macrophage engulfment, such as those reported in NOD mice [36, 38], could lead to a buildup of fragments of β -cells destroyed as part of natural processes such as the β -cell apoptotic wave during the neonatal period [18, 58] or due to external stressors such as infections. Defective cleanup of cellular debris could trigger the production of chemotactic factors such as CCL2 to further recruit macrophages and inflammatory factors such as tumor necrosis factor (TNF) that prime APCs for T-cell activation. Overall, the polyclonal nature of the immune responses against multiple autoantigens and the uncertainty in the role of APCs in disease initiation and progression [38] make identifying and designing therapeutic strategies, such as the monoclonal antibody-based approaches [4, 27] and autoimmune-specific nanovaccines [59] very challenging.

Mathematical approaches to understanding T1D typically involve developing dynamical models expressed as sets of ordinary differential equations (ODEs) or partial differential equations (PDEs) that describe the temporal dynamics of the population sizes of immune cells, β -cells, as well as the expression level of autoantigens and titre level autoantibodies implicated in the disease. Numerical simulations incorporating estimated or experimentally derived parameters and bifurcation analysis are typically used to examine their short and long term (steady-state) behaviour. Once these models are perfected and validated against

experimental data, they can eventually serve as diagnostic tool(s) of the disease in clinical settings. A brief overview of the application of mathematical models, including model set-up and main results, is presented in the next sections.

1.1.1 Modeling APCS

Antigen presenting cells play a central role in the immune response. A model of T1D development termed the Copenhagen model [42] was proposed to analyse their dynamics (Fig. 1–1). In brief, the model is described as follows: after ingesting antigenic particles such as dead β -cell fragments in the case of T1D autoimmunity, APCs upregulate antigen processing pathways, secrete chemokines to further recruit other APCs to the islets and increase expression of co-stimulatory molecules to activate β -cell specific autoreactive CD4⁺ and CD8⁺ T-cells. These activated APCs also upregulate the secretion of cytokines such as interleukine-1 (IL-1), TNF and reactive oxygen species (ROS) which lead to further stress-induced β -cell death [11, 56], accumulation of dead β -cell debris of APC engulfment, and amplification of the autoimmune response.

Apoptotic or necrotic β -cells that are not removed promptly were shown to trigger the secretion of high levels of inflammatory cytokines of from activated macrophages in NOD mice [51]. A possible mechanism for the initiation of this positive autoimmune feedback loop was hypothesized to be related to defects in macrophage engulfment and clearance of the neonatal wave of apoptotic β -cells [18, 58] which triggers increased inflammatory response in NOD mice but not in healthy Balb/c mice. Based on experimental data, Marée et al. [36, 37] showed mathematically that macrophages from healthy Balb/c mice engulfed apoptotic

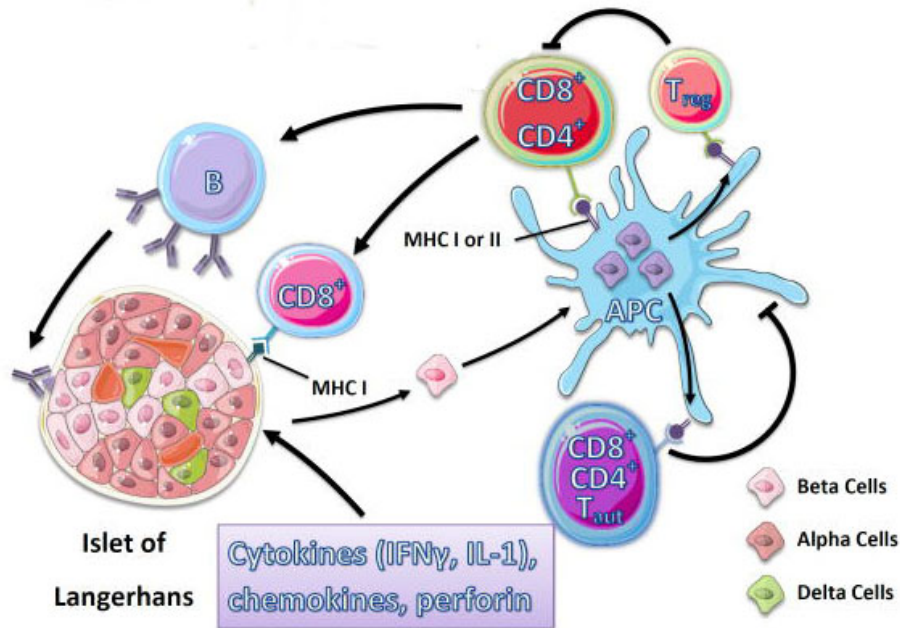


Figure 1–1: Role of APC mediating anti- β cell autoimmune response adapted from Fig. 1B of [28] with permission.

cell bodies 2.6 – 5.5 times faster than macrophages isolated from NOD mice and that the digestion of apoptotic cells bodies was also at least twice as slow in NOD mice compared to Balb/c macrophages [36, 37]. This quantitative analysis was performed using Markov state models developed to describe the process of macrophage engulfment and digestion of apoptotic cells bodies, where each state of the model represented the number of macrophages with a given number of engulfed apoptotic bodies inside vesicles within the cell. The model showed that though an activation step and an accelerated engulfment following macrophage activation exists in both Balb/c and NOD strains, albeit smaller in NOD than in Balb/c mice. This decrease in macrophage activation and engulfment in NOD mice

contribute to the build-up of apoptotic β -cell debris in the pancreatic environment and sustains the inflammatory feedback leading to β -cell death.

1.1.2 Modeling T-cell dynamics

Mathematical models of T1D progression have two main goals: testing possible mechanisms underlying the function of effector $CD4^+$, cytotoxic $CD8^+$ and (auto)regulatory T-cells during the development of T1D, and analyzing as well as optimizing the effect(s) of certain interventional therapies.

T-cells play a central role in all autoimmune diseases and are the main therapeutic targets. T-cells require two signals for activation: the engagement of TCR with its cognate antigen-specific pMHC ligand and a co-stimulatory signal selectively expressed on the surface of professional APCs. Because naïve T-cells experience anergy and apoptosis when stimulated with pMHC in the absence of costimulation, treatment with peptides or soluble pMHCs is an attractive therapeutic approach that, unfortunately, only led to limited success at reversing hyperglycemia in NOD mice [9]. Counter-intuitively, administration of certain peptides designed to induce tolerance or deletion of autoreactive T-cells mostly failed to blunt the poly-specific autoimmune response. For example, despite effective deletion of IGRP_{206–214}-reactive T-cells, where IGRP is a dominant β -cell specific autoantigenic peptide, there was only moderate delays in onset of diabetes [24].

Mathematical model of this process consisting of two competing clones of T-cells, with various levels of avidities, revealed that deletion of all IGRP_{206–214}-reactive clones creates a vacuum in the homeostatic pool of T-cells that promote

the expansion of pathogenic sub-dominant specificities [38], a result verified experimentally [24]. It has long been known that homeostatic mechanism maintain the total population size of the T-cell pool at a near constant steady state level. Deletion of all T-cells reactive to one specific antigen by peptide treatment allows other clones to occupy the T-cell niche emptied by the treatment and return the T-cell population to its natural levels [38, 54]. In order to be successful, the mathematical model predicted that it would be critical to foster the expansion and recruitment of low-avidity clones that are non-pathogenic. Evidence such a population of non-pathogenic low-avidity T-cells exist from studies by Santamaria et al. [59], showing that a reversal of diabetes through treatment with antigen-specific pMHC conjugated to nanoparticles (NPs) correlated with an expansion in a small pool of low-avidity T-cells. These low-avidity CD8⁺ T-cells are thought to be part of the population of T-cell that prevent the expansion of high-avidity pathogenic populations through APC deletion [1, 59].

The protective role of low-avidity CD8⁺ T-cells was investigated from mathematical perspective by developing a model comprised of two interacting populations of T-cells [31]: low-avidity T-cells enriched for memory cells and high avidity T-cells consisting mostly of naïve and effector cells. The role of APCs in T-cell activation, and the ability of dead β -cells to increase the autoimmune response was also studied [31]. The model was used to test two important hypotheses suggested by experimental data : (i) the expanded pool of low-avidity memory T-cells infiltrate the islets, crowding out effector high avidity cells and interfering

with their ability to kill β -cells, (ii) low-avidity memory T-cells delete APCs presenting the IGRP_{206–214} peptide on their surface thereby inhibiting the activation of high-avidity T-cells. It was shown under hypothesis (i), the level of β -cells in the diseased state rapidly increases with increasing expansion rate of low-avidity T-cells, which is incompatible with observed data, making hypothesis (ii) more plausible. The model revealed that progressive accumulation of memory T-cells during disease progression makes treatments aimed at expanding these protective T-cell types more effective close to, or at the onset of clinical disease.

1.2 Nanoparticle treatment of T1D

The idea of conjugating pMHCs to NPs have several advantages over soluble peptides or pMHCs: (i) NPs provide scaffolding to enhance TCR-crosslinking, a critical requirement for T-cell activation and (ii) NP-bound pMHCs would be protected from degradation thus increasing its half-life in circulation [10, 8]. Treatment with monospecific NPs, composed of a variable sized iron oxide core surrounded by 10 nm layer of pegylation, conjugated to islet-specific antigenic pMHCs (pMHC-NPs) were able to both blunt T1D progression in prediabetic mice and newly diagnosed diabetic animals by expanding the subset of memory autoregulatory CD8⁺ T-cells [59]. These autoregulatory CD8⁺ T-cells arose spontaneously during chronic disease progression through repeated autoantigen exposure and function as a negative feedback by inhibiting the activation and recruitment of naïve pathogenic T-cells to islets via deletion of autoantigen-presenting APCs [8, 10, 59]. The pMHC-NPs lack the necessary co-stimulatory molecules required to activate pathogenic T-cells thus leading to their suppression.

These results were predicted by the mathematical model in [31] as well as verified experimentally in [59].

Mathematical model of pMHC-NP treatment was used to predict the outcome of the pMHC-NP therapy, to understand the dynamics of competition between T-cell clones as a guide to optimize treatment frequency and dose [52]. It was shown that increasing the frequency of injection is more effective therapeutically than increasing the dose [31]. By taking into account that the expansion of autoregulatory T-cells and deletion of autoantigen-loaded APCs by these T-cells are biphasic, that is, no T-cell expansion at low NP doses, expansion at intermediate dose and cell deletion at high NP doses, effective range of doses and ranges in pMHC-NP valency were also be identified. It was found in this study that NP injection dose should exceed $8\mu\text{g}$ for the treatment to become effective. At this dose, moderate increase (≥ 1.6 -fold) in the NP-dependent expansion rate of autoregulatory T-cell population led to a significant increase in the efficacy and the area corresponding to the effective treatment regiment [52].

1.2.1 T-cell expansion *in vivo*

Follow-up experimental studies by the Santamaria group aimed at providing quantitative information on the expansion of the memory population were completed by treating cohorts of 10 week old female NOD mice injected i.v. with pMHC-coated NPs of various valency in PBS twice a week for 5 weeks. Changes in the percentage of antigen-specific autoregulatory T-cell population of CD4^+ T-cells collected from the spleen and quantified using flow cytometry (FACS) (Fig. 1–2) showed that population expansion to be proportional to dose, but not valency.

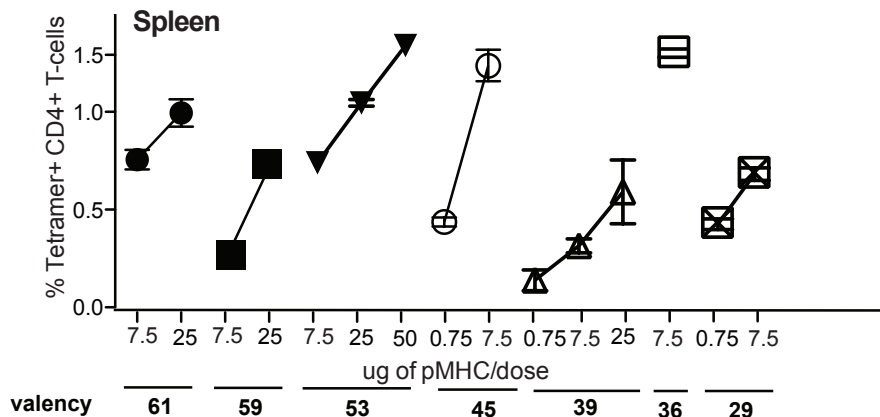


Figure 1–2: Percentages of tetramer⁺ splenic CD4⁺ T-cells in NOD mice treated with 8 nm diameter core NPs with different pMHC valencies and dose.

Understanding the effects of valency on the expansion of the autoregulatory T-cell population and extending to the effect of NP size is the first goal of this thesis.

1.2.2 *in vitro* stimulation experiments

Experimental attempts to gain insights into the possible mechanisms underlying the effects of pMHC-NPs on T-cell activation observed *in vitro* were pursued. It was found that pMHC-NPs bind to cognate T-cells from TCR-transgenic 8.3-NOD mice as clusters of several NPs spanning approximately up to 400 nm (Fig. 1–3). This binding geometry was seen within 30 minutes of incubation at 4°C, and reach their maximum size after a further 90 minutes at 37°C (unpublished data).

To investigate the agonistic properties of pMHC-NPs, *in vitro* stimulation experiments were conducted with naïve FACS-sorted splenic CD8⁺ T-cells from TCR-transgenic mice. Cells were suspended to a concentration of 2.5×10^5 cells/mL and incubated with various concentrations of pMHC-NPs for 48 h at

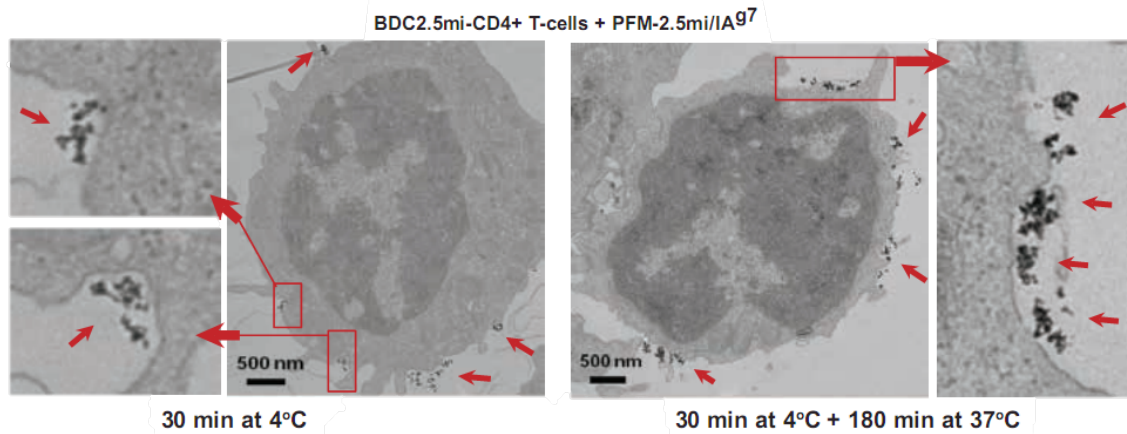


Figure 1–3: Transmission electron micrograph of T-cell after treatment with pMHC-NPs.

37°C. The supernatants were assayed for the cytokine interferon gamma ($\text{IFN}\gamma$) by enzyme-linked immunosorbent assay (ELISA) (Fig. 1–4). 8.3- CD8^+ T-cells produced negligible amounts of $\text{IFN}\gamma$ when cultured in the presence of NPs coated with 8 pMHC monomers per NP, but produced substantially higher amounts of $\text{IFN}\gamma$ in response to NPs coated with higher pMHC valencies, even as low as 11 pMHCs/NP, in a dose-response manner. However, whereas 25×10^{11} NPs (per ml) carrying 11 pMHCs/NP had similar agonistic activity as 5×10^{11} NPs (per ml) carrying 54 pMHCs/NP, increasing the number of NPs carrying 8 pMHCs/NP to values as high as 40×10^{11} NPs/ml had minimal effects. Similarly for larger 20 nm NPs, increasing NP dose to as high as 75×10^{11} NPs/ml using NPs coated with 9 pMHC/NP resulted in negligible $\text{IFN}\gamma$ production. These results indicate that there is a threshold of pMHC valency for 8 nm NPs lying between 9 and 11 pMHCs/NP, and for 20 nm NPs lying above 13 pMHC/NP below which increases

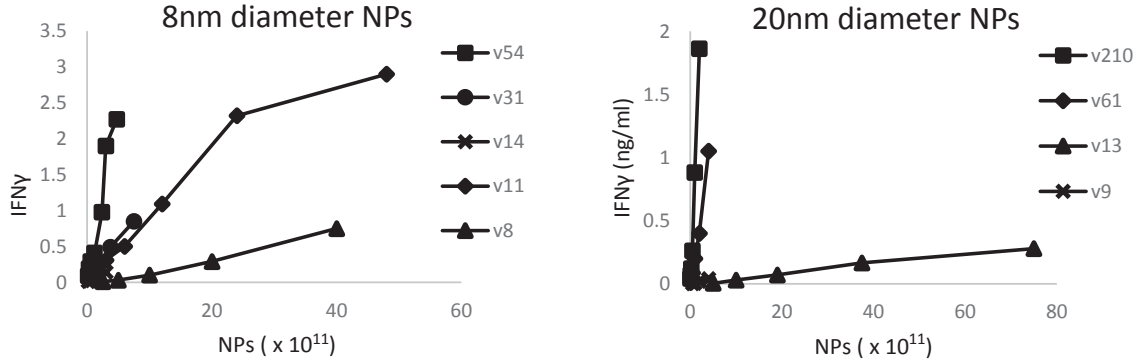


Figure 1–4: Amount of IFN γ produced by naïve splenic CD8⁺ T-cells from TCR-transgenic 8.3-NOD mice detected by ELISA after stimulation with cognate pMHC-NPs with 8 nm diameter core or 20 nm diameter core with different pMHC valencies and doses.

in the number of NPs (i.e. 5-fold) cannot overcome the low agonistic activity of pMHC-NPs coated at low valencies.

Collectively, these results indicate that pMHC density is a critical parameter in the design of pMHC-based nanomedicines. The importance of the experimental system and the modeling associated with it arise from the fact that they could be generalized to other autoimmune disorders and could eventually serve as computational tools to understand and optimize pMHC-NP-based therapies in these diseases.

1.3 Aims

T-cells are the key mediator of a host of autoimmune disease and the treatment schema presented here need not be limited to one disease. With this understanding of the biological foundations of autoimmune diseases such as T1D and an experimental framework of treatment using pMHC-NPs, in this thesis, we will use mathematical models to understand the results of two experimental paradigm of

T-cell-NP interactions. Our mathematical approach to understanding the action of the NPs begins with an overview of parameter estimation methods with a focus on the method of Markov Chain Monte Carlo (MCMC), a method of parameter estimation arising from statistical inference, which is well-suited to biological application that contain variation due to heterogeneity (Chapter 2). We will see how MCMC can be generalized from statistics to fit the kinetic parameters of ODE systems, and determine how the underlying statistical theory can be transferred to provide stationary distributions of parameter estimates. In Chapter 3, we develop a model to explain the level of T-cell proliferation *in vivo* following intravenous injections of pMHC-NPs shown in Fig. 1–2. In Chapter 4, we develop a model to understand the biophysical dynamics of the pMHC-NP and T-cell interaction starting from the formation of nanoclusters seen in Fig. 1–3, to the binding of individual NP and also analyse the co-operativity of binding in pMHCs that are coated on each NP, and how these different levels of interaction produce the activity in Fig. 1–4. Chapter 5 addresses concerns with the model developed in Chapter 4 especially with regards to some quantitative feature of nanoclusters and the activation kinetics of pMHC-NP stimulation, and recommend adjustments to the model.

CHAPTER 2

Markov Chain Monte Carlo for parameter estimation

2.1 Statistical approaches of estimation

A primary concern in model development is finding a set of parameter values that produce a good fit to a set of empirical data using results of model simulation. The broad branch of statistics that deals with producing reasonable parameter estimates based on data that has a random component is called Inference Theory. The probabilistic approach to this type of estimation used here assumes that the data is drawn from some probability distribution that depends on the parameters of interest.

The two main components of statistical estimation are the experimental or empirical data, $(x_1, x_2, \dots, x_n) = \mathbf{x}$, that we wish to reproduce using the mathematical model and the corresponding parameters, $\boldsymbol{\theta}$. The quantity of interest in parameter estimation is the posterior probability $p(\boldsymbol{\theta} | \mathbf{x})$ which is the probability of the parameters $\boldsymbol{\theta}$ after taking into account the observed data \mathbf{x} . By Bayes' rule, this posterior distribution can be expressed as a consequence of a prior probability of the parameter, $\pi(\boldsymbol{\theta})$ and the likelihood for the observed data $p(\mathbf{x} | \boldsymbol{\theta})$:

$$p(\boldsymbol{\theta} | \mathbf{x}) = \frac{p(\mathbf{x} | \boldsymbol{\theta})\pi(\boldsymbol{\theta})}{p(\mathbf{x})}. \tag{2.1}$$

The likelihood $p(\mathbf{x} \mid \boldsymbol{\theta})$ is calculated as joint density function for all (independent and identically distributed) observations given the parameters $\boldsymbol{\theta}$:

$$p(\mathbf{x} \mid \boldsymbol{\theta}) = p(x_1, x_2, \dots, x_n \mid \boldsymbol{\theta}) = \prod_{i=1}^n p(x_i \mid \boldsymbol{\theta}) \quad (2.2)$$

and $\pi(\boldsymbol{\theta})$ represents the prior knowledge we have about $\boldsymbol{\theta}$. The denominator of the expression $p(\mathbf{x})$ represents the probability of the data averaged over all parameters. Since the denominator is independent of $\boldsymbol{\theta}$, this factor is the same for all possible parameters being considered. Therefore, we can simplify Eq. (2.1) to:

$$p(\boldsymbol{\theta} \mid \mathbf{x}) \propto p(\mathbf{x} \mid \boldsymbol{\theta})\pi(\boldsymbol{\theta}) \quad (2.3)$$

Since our goal is to estimate the parameters, the problem of estimation can often be framed as an optimization problem to minimize the error function:

$$\mathbf{e} = \hat{\boldsymbol{\theta}} - \boldsymbol{\theta}, \quad (2.4)$$

where $\hat{\boldsymbol{\theta}}$ represents an estimate of the true parameter values. Since the true parameter values are often unknown, the alternative is to find an estimate that minimizes the mean square error (MSE) between the observed data and the model simulation, given by

$$\text{MSE} = \frac{1}{n} \sum_{i=1}^n (\hat{X}_i - X_i)^2, \quad (2.5)$$

where \hat{X}_i represent the outcomes of the model which correspond to the i -th observation given by X_i . Estimators such as the minimum mean square error (MMSE), as its name implies, minimizes the MSE.

In the case of Bayesian inference, the optimization problem is one of maximization. The posterior $p(\boldsymbol{\theta} \mid \mathbf{x})$ expressed in Eq. (2.1) can be viewed as a function where the observed values x_1, x_2, \dots, x_n are fixed quantities whereas $\boldsymbol{\theta}$ is the variable allowed to vary freely. The method of maximum a posterior (MAP) estimation is to find $\hat{\boldsymbol{\theta}}_{MAP}$ such that:

$$\hat{\boldsymbol{\theta}}_{MAP}(x) = \arg \max_{\boldsymbol{\theta}} p(\boldsymbol{\theta} \mid \mathbf{x}) = \arg \max_{\boldsymbol{\theta}} p(\mathbf{x} \mid \boldsymbol{\theta})\pi(\boldsymbol{\theta}). \quad (2.6)$$

It is normal to ignore $p(\mathbf{x})$, the term in the denominator of Eq. (2.1), in optimizing $p(\boldsymbol{\theta} \mid \mathbf{x})$, since it is a constant normalizing factor to ensure $p(\boldsymbol{\theta} \mid \mathbf{x}) \leq 1$.

2.2 Numerical optimization

The basic procedure of a numerical approach to optimization involves three basic steps:

- *initiation*: define the model and an initial guess $\boldsymbol{\theta}^{(0)}$.
- *iteration*: refine the initial guess by making adjustments using some update function.
- *termination*: stop iteration with some stopping or convergence criteria.

In Bayesian parameter estimation, the posterior $p(\boldsymbol{\theta} \mid \mathbf{x})$ is only a function of the parameters $\boldsymbol{\theta}$.

If $p(\boldsymbol{\theta} \mid \mathbf{x})$ is differentiable, then the maximum and minimum must be attained when

$$\frac{\partial p(\boldsymbol{\theta} \mid \mathbf{x})}{\partial \theta_i} = 0. \quad (2.7)$$

We can then employ a number of iterative root-finding algorithms, such as Newton's method, to solve for $\dot{p}(\boldsymbol{\theta} \mid \mathbf{x}) = 0$.

When $p(\boldsymbol{\theta} \mid \boldsymbol{x})$ is not differentiable, the parameter space will have to be sampled directly to obtain the maximum likelihood. Markov Chain Monte Carlo (MCMC) is a technique that solves the problem of sampling from a complicated distribution. The Monte Carlo involves performing a large number of simulations each with randomly drawn parameters. If these randomly drawn parameters are part of a random walk in a Markov Chain, then the stationary distribution of this chain can be constructed to simulate the posterior distribution of the parameters.

The parameter estimate is obtained by “wandering around” on the surface given by the posterior $p(\boldsymbol{\theta} \mid \boldsymbol{x})$ in such a way that the amount of time spent in each location is proportional to the height of the distribution at that location. In the Metropolis-Hastings algorithm [25, 39], the random walk is directed in such a way that it is always favourable to be walking in the direction that increases $p(\boldsymbol{\theta} \mid \boldsymbol{x})$. However if the proposed location (selected uniformly across the entire surface) is lower than the current location, then the move is assigned a probability p , where p is the ratio of the height of proposed point to the current location. As the walk confined to the hilltops of the surface and quickly moves out of the valleys, stationary distribution of this random walk, representing its behaviour over long time, converges to the distribution of $p(\boldsymbol{\theta} \mid \boldsymbol{x})$. One distinct advantage of MCMC methods over other point-estimators, which produce parameter estimates that are single-valued, is that MCMC provides with parameter estimates with an associated probability density. Studying distributions of parameters is a much more informative approach than knowing a single value of parameters in biological systems where heterogeneity is inevitable.

2.2.1 Numerical MCMC algorithm

The Metropolis-Hasting algorithm is a popular MCMC method when the posterior distribution has no conjugacy to known distribution consisting of more than two parameters. Since these types of problems are quite frequent in Bayesian inference, the Metropolis-Hastings algorithm is a popular algorithm to implement MCMC.

The Metropolis-Hastings Algorithm follows the following steps:

Initiation Step

Given some data, X_1, X_2, \dots, X_n sampled from a distribution $f(X | \theta)$, the Bayesian approach is implemented by calculating the posterior probability, given by:

$$p(\theta | \mathbf{X}) \propto f(\mathbf{X} | \theta)\pi(\theta) = \left(\prod_{i=1}^n f(X_i | \theta) \right) \pi(\theta). \quad (2.8)$$

Often, it is the log-likelihood $\ell(\theta | \mathbf{X}) = \log p(\theta | \mathbf{X})$ that is computed to simplify the product in Eq. (2.8) to a sum.

The algorithm begins with an *initiation* step where an initial guess $\theta^{(0)}$ is made inside the parameter space Θ , and $\ell(\theta^{(0)} | \mathbf{X})$ is computed as

$$\ell(\theta^{(0)} | \mathbf{X}) = \ell(\theta^{(0)}) + \sum_{i=1}^n \ell(X_i | \theta), \quad (2.9)$$

where $\ell(X_i | \theta) = \log (f(X_i | \theta))$ and $\ell(\theta^{(0)}) = \log \pi(\theta^{(0)})$.

Update (Iteration) Step

In the *iteration* phase, the choice of a new parameter $\theta^{(i+1)}$ is selected based on the current parameter values $\theta^{(i)}$, a random noise term ω , and the standard

deviation of the prior Σ . The resulting new parameter is thus given by:

$$\theta^{(i+1)} = \theta^{(i)} + \omega \Sigma \quad (2.10)$$

Since this parameter update for $\theta^{(i+1)}$ is dependent on the previous parameter $\theta^{(i)}$, this sampling method is called random walk Metropolis sampling.

To ensure the new parameter stays within the domain of valid values, Θ , parameter updates that fall outside of the domain are rejected.

Acceptance-Rejection Step

The key element of the acceptance-rejection decision is based on the acceptance criteria α , sometimes called the “likelihood ratio”, to determine whether the new parameters improve the log-likelihood computed, where.

$$\alpha = \log \left(\frac{p(\theta^{(i+1)} | \mathbf{X})}{p(\theta^{(i)} | \mathbf{X})} \right) = \ell(\theta^{(i+1)} | \mathbf{X}) - \ell(\theta^{(i)} | \mathbf{X}). \quad (2.11)$$

If $\alpha \geq 0$, i.e. $p(\theta^{(i+1)} | \mathbf{X}) \geq p(\theta^{(i)} | \mathbf{X})$, then $\theta^{(i+1)}$ is accepted. If $\alpha < 0$, then $\theta^{(i+1)}$ is accepted with a probability determined by the criterion:

1. draw a value u using the $\mathcal{U}(0, 1)$ distribution.
2. if $\alpha \geq \log(u)$, accept $\theta^{(i+1)}$, otherwise, the parameter update is rejected and $\theta^{(i+1)}$ is set to $\theta^{(i)}$.

This incorporation of random chance in acceptance of a new parameter allows the sampler to traverse through more unfavourable regions of the parameter space in order to find multiple minimas.

Termination Step

The update and acceptance-rejection steps are repeated till the specified number of iteration is reached, which represents the *termination* criterion.

Performance and validity of an application of the Metropolis-Hastings algorithm can be assessed using the acceptance rate, the proportion of parameters proposals from the update step that pass the acceptance-rejection criterion. If the acceptance rate is too high, it means that the chain is not moving around enough in the parameter space because the update steps are too small. If the acceptance rate is too low, it means the algorithm is too inefficient with the possibility that each update step is too large. In general, an acceptance ratio between 0.25 and 0.50 is recommended [3, 47].

Convergence to the stationary distribution usually occurs regardless of the initial starting point; however, the time it takes for the chain to converge does depend on the starting point. In practice, a certain set of initial iterations in the MCMC chain is thrown out, called the burn-in. Such a step guarantees that the draws are closer to the stationary distribution and less dependent on the starting point.

2.3 Markov Chain Monte Carlo in differential equations models

MCMC methods and the Metropolis-Hastings algorithm are not restricted to probabilistic models. In fact, the basic premise of MCMC methods rely on taking random walks in the parameter space constructing a Markov Chain that has the same equilibrium distribution as the desired distribution.

In biological systems we typically have some data $D(t_i)$ which are measurements made at discrete time points t_i and a proposed model of a system of ODEs $\dot{\mathbf{x}}(t | \theta)$, where θ represents a set of free, typically kinetic, parameters that changes the outcomes of the model, and $\mathbf{x}(t | \theta)$ is the solution of the ODE model given by $\mathbf{x}(t|\theta) = \int \dot{\mathbf{x}}(t | \theta)dt$. The MCMC methods can thus be used to find the stationary distribution of the parameters by finding the best fit according to some criterion defined by the error function. The most common is the sum of square errors given by

$$\chi^2 = \sum_i \frac{(D(t_i) - \mathbf{x}(t_i|\theta))^2}{2\sigma^2} \quad (2.12)$$

where σ is a normalizing factor that represents some estimate of the standard deviation of the data.

The likelihood for observing the recorded data is assumed to have a Gaussian distribution:

$$p(D|\theta) = \prod_i \frac{1}{\sigma\sqrt{2\pi}} e^{-\left(\frac{(D(t_i) - \mathbf{x}(t_i|\theta))^2}{2\sigma^2}\right)} \propto e^{-\left(\sum_i \frac{(D(t_i) - \mathbf{x}(t_i|\theta))^2}{2\sigma^2}\right)} = \exp(-\chi^2). \quad (2.13)$$

Thus the log-likelihood is simply equal to the negative of the sum of square error function, which is maximal when the error is minimal.

Applying the Metropolis-Hasting algorithm to do a maximum likelihood estimation, and finding the set of parameters that minimizes the error follows similar steps as in most statistical applications. In other words, when implementing this method, we:

1. start with some initial guess for the parameter values and compute χ_{current}^2 ;
2. propose a new set of parameter values and calculate χ_{proposed}^2 ;

3. compute the acceptance criterion, given by;

$$\alpha = \log \left(\frac{p(D|\theta_{\text{proposed}})}{p(D|\theta_{\text{current}})} \right) = -\chi_{\text{proposed}}^2 + \chi_{\text{current}}^2; \quad (2.14)$$

4. pick a uniform random number u from $\mathcal{U}(0, 1)$;

5. accept if $\alpha \geq \log u$ and set $\theta_{\text{current}} = \theta_{\text{proposed}}$, otherwise reject θ_{proposed} ;

6. repeat steps 2–5 until the desired number of iterations is reached.

In the 45 years since the Metropolis-Hastings algorithm was established, many aspects of this method have been improved upon to enhance parameter convergence and computational efficiency including taking adaptive step sizes when proposing new parameters as well as delaying rejection sampling [23, 22]. The implementation of MCMC in this thesis was done using the MCMC Toolbox in MATLAB developed by Haario et al. (<http://helios.fmi.fi/~lainema/mcmc/>).

2.3.1 Example and usage

We will use a simple example to demonstrate the steps of the MCMC algorithm as applied to an ODE system. Consider the logistic equation modeling population growth:

$$\frac{dP}{dt} = rP \left(1 - \frac{P}{k} \right), \quad (2.15)$$

with P as the population size, r as the growth rate and k as the carrying capacity.

Starting with an small initial population of P_0 , growth is unimpeded and is governed by the first term rP in the early phase of the system. As the population grows, the second term rP^2/k dominates due to an increase in competition for critical resources. This antagonistic effect is governed by the value of the parameter k . The competition diminishes the total growth rate, until P reaches a

Time (h)	Population (10^3 cells/ml)						mean	σ
	1	2	3	4	5	6		
0	1	1	1	1	1	1	1	
1	18	18	4	11	19	20	15	6.26
2	63	43	43	32	70	27	46.3	16.97
3	240	260	270	310	290	270	273.3	24.22
4	700	740	770	760	710	720	733.3	28.04
5	930	940	950	960	990	960	955	20.74
6	960	1000	940	1040	990	1000	988.3	34.88
7	940	990	1090	1010	1010	970	1000	50.76
8	970	930	990	920	1060	1050	986.7	58.88

Table 2–1: Six simulated experiments on the growth of *Escherichia coli* in LB broth.

steady state. With an initial population of P_0 , the analytical solution to Eq. (2.15) is:

$$P(t | r, k) = \frac{kP_0e^{rt}}{k + P_0(e^{rt} - 1)}, \quad (2.16)$$

where

$$\lim_{t \rightarrow \infty} P(t) = k. \quad (2.17)$$

The logistic equation models only very simple conditions which do not have other factors that affect population growth such as predator/prey dynamics, migration etc., conditions that are typically found in a petri dish in a lab. We simulated concentration of the bacterium *Escherichia coli* cultured in Luria broth (LB), a nutrient-rich media, with an initial seed of 1000 cell/ml in 6 experiments (Table 2–1). Data was generated with $r = 2 \text{ h}^{-1}$ and $k = 1000 \times 10^3 \text{ cell/ml}$, and adding Gaussian noise to each time point proportional to the size of the population at the time.

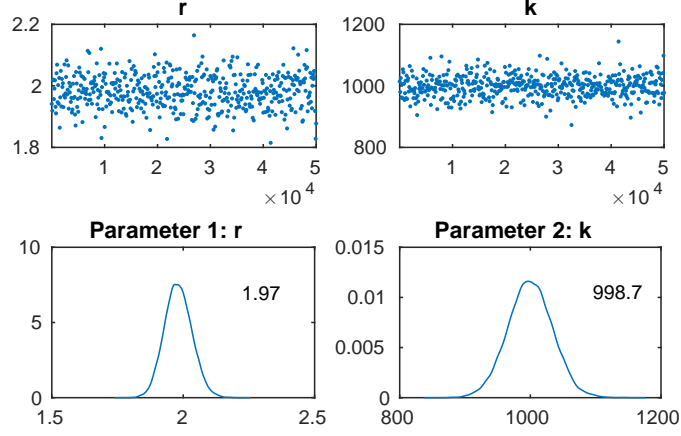


Figure 2-1: Distribution of estimated parameters r and k

Parameter	Mode
r	1.97 h^{-1}
k	$998.7 \times 10^3 \text{ cell/ml}$

Table 2-2: Modes of estimated parameters in the logistic model

To illustrate how MCMC algorithm works, we will re-estimate the values of the growth rate r and the carrying capacity k using these iterative methods and the noisy (artificial) data listed in Table 2-1. Starting with an initial guess of $r = 10 \text{ h}^{-1}$ and $k = 100 \times 10^3 \text{ cell/ml}$, the negative of the log-likelihood function, which follows the formulation in Eq. (2.13) and defined to be the sum-of-square error, is calculated by:

$$\chi^2 = \sum_{i=1}^6 \sum_{t=1}^8 \frac{(Data_i(t) - P(t | r = 10, k = 100))^2}{2\sigma^2(t)}, \quad (2.18)$$

where $Data_i$ represents the data from the i -th experiment, and $P(t | r, k)$ is the expression given by Eq. (2.16).

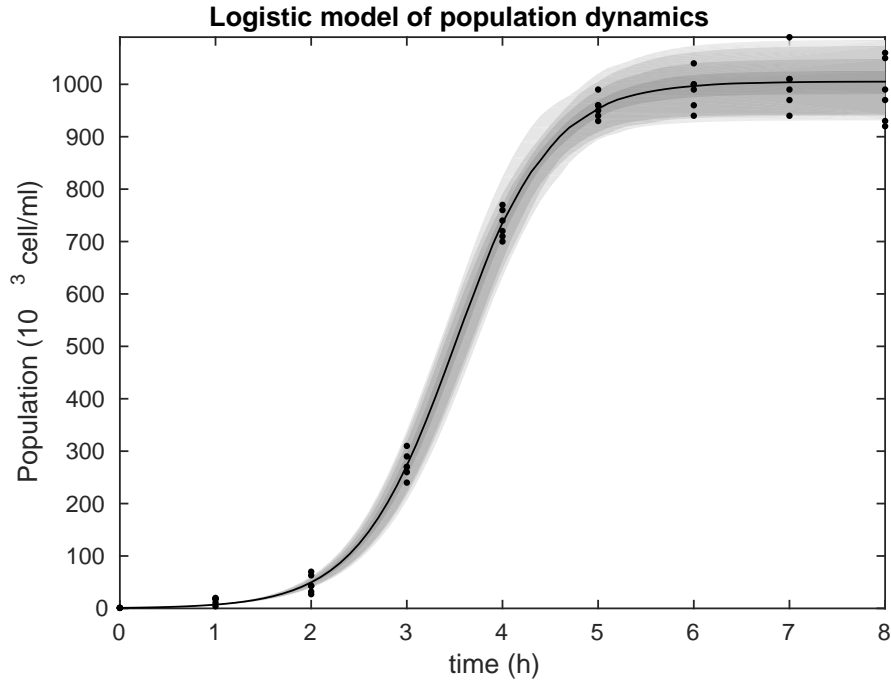


Figure 2-2: Fitting the logistic model (solid line) to bacteria growth data (black dots). The grey bands represent confidence intervals with the darker colors representing higher confidence.

Following this initial guess, the MCMC Toolbox is run for 100 000 iterations, repeating the procedure of making a guess at a new parameter, calculating the difference in χ^2 and accepting or rejecting this new parameter based on this difference. The resulting Markov Chain and distribution is shown in Fig. 2-1.

Table 2-2 shows that the mode of the two distribution is $r = 1.97 \text{ h}^{-1}$ and $k = 998.7 \text{ cell/ml}$ (Table 2-2), which is remarkably close to the true parameter values ($r = 2 \text{ h}^{-1}$ and $k = 1000 \times 10^3 \text{ cell/ml}$). Using the distribution of parameters in Fig. 2-1, we can use the model given in Eq. (2.16) to create a fit through the

experimental data as well as assign confidence intervals of where the data is likely to be observed.

For more complicated model, the ODE system generally does not lend itself to an explicit analytical solution. In those cases, numerical ODE solvers such as `ode45` or `ode15s` are typically used to obtain numerical solution to the model $P(t | r, k)$ for parameter estimation.

CHAPTER 3

Model of *in vivo* T-cell proliferation

The treatment of T1D in NOD mice using nanoparticles coated with pMHC depends critically on the ability of pMHC-NPs to expand the population of autoregulatory T-cells to therapeutic levels [8, 59]. Understanding how the design of pMHC-NPs, in relation to pMHC valency, size of NP and dose, affect the steady-state population of autoregulatory T-cells is key to optimizing the therapeutic efficacy of treatment.

In this chapter, we develop a model to understand how stimulation with pMHC-NPs of various valencies, sizes, and concentrations affect T-cell proliferation *in vivo* following the protocol described in Section 1.2.1. We use steady-state analysis to predict the long-term behaviour of our model corresponding to experimental data (Fig. 1–2). Our model is based on aspects of previous work by Marée et al. [38] and provides insights on the relative effects of NP size and valency for T-cell expansion.

3.1 Model development

We present in Fig. 3–1 the scheme describing the interaction of pMHC-NPs with T-cells *in vivo*. The NPs bind to and unbind from T-cells with a certain rate, given by b_{on} and b_{off} respectively. The scheme shows that, after binding, a certain fraction of T-cells F will activate and proliferate whereas the rest $(1 - F)$ will remain dormant. The dynamics of this system can be described by the equations:

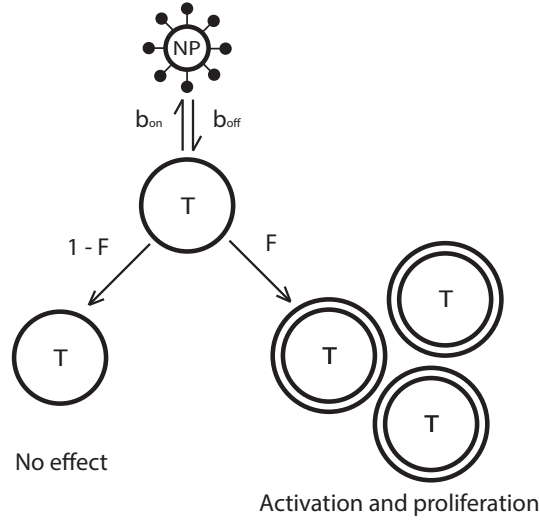


Figure 3–1: Model of T-cell proliferation *in vivo*.

$$\frac{dX}{dt} = (1 - F)b_{off}X_b + FMb_{off}X_b - b_{on}s_fX - X(\delta + \varepsilon X) \quad (3.1)$$

$$\frac{dX_b}{dt} = b_{on}s_fX - b_{off}X_b, \quad (3.2)$$

where X is the number of free T-cells and X_b is the number of NP-bound T-cells. In this model, M represents the number of cells produced through proliferation by one T-cell, s_f represents the number of available NPs for binding, δ represents the death rate of activated T-cell and ε represents the homeostatic competition between T-cells to maintain a constant T-cell population size.

At steady state, the number of NP-bound and free T-cells are:

$$X_b = \frac{b_{on}}{b_{off}} s_f X \quad (3.3)$$

$$X = \frac{F(M-1)b_{on}s_f - \delta}{\varepsilon}. \quad (3.4)$$

Since in each replication cycle, the dividing cell produces two daughter cells, we may conclude that the number of cells produced through replications is:

$$M = 2^d, \quad (3.5)$$

where d is the number of divisions each proliferating cell undergoes.

In this model, we assume the fraction of T-cells that are activated after binding, F , is a sigmoidal function of the number of pMHC-TCR complexes (m_t), described by:

$$F = \frac{m_t^2}{a^2 + m_t^2}. \quad (3.6)$$

Since NPs tend to cluster on the T-cell surface (Fig. 1–3), we can estimate the maximum number of NPs at a binding site by calculating the number of circles of radius r that can lie entirely inside a larger circle of radius $R > r$. Following the schematic in Fig. 3–2, the number of layers that small circles can form within the larger circle in a concentric ring structure is given by

$$N = \frac{R}{2r} - \frac{1}{2} \quad (3.7)$$

layers. Each layer, n , is occupied by $6n$ circles, with the center defined to be layer 0. This makes the total number of NPs to be

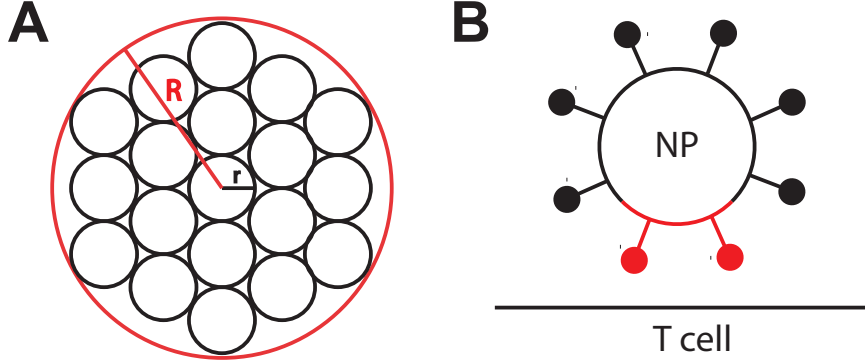


Figure 3-2: Schematics representing **A)** the estimation of the maximum number of NPs of radius r that fills a binding site of radius R and **B)** the contact area (red) between the spherical NP and the relatively flat surface of the T-cell surface.

$$nNP = 1 + 3 \left(\frac{R}{2r} - \frac{1}{2} \right) \left(\frac{R}{2r} + \frac{1}{2} \right) \quad (3.8)$$

at each binding site.

Because T-cells are much larger in size than NPs, one can assume that only a proportion of the spherical structure of NPs make effective contact with the T-cell (Fig. 3-2B). Assuming the angle of contact is no more than 45° , we can calculate the area of contact as follows:

$$\begin{aligned} A &= 2\pi \int_{\pi/4}^{\pi/2} r \cos \theta \sqrt{r^2 + \left(\frac{dr}{d\theta} \right)^2} d\theta = 2\pi \int_{\pi/4}^{\pi/2} r^2 \cos \theta d\theta \\ &= (2 - \sqrt{2})\pi r^2 \approx \frac{1}{7}4\pi r^2. \end{aligned} \quad (3.9)$$

The surface of the spherical NPs making effective contact with the relatively flat surface of the T-cells is approximately $1/7$ of the total surface area of the NP. This means that only $1/7$ of the total pMHCs carried by each NP can make

contact with the TCR. As a result, the effective valency of NPs is given by:

$$\hat{v} = v/7. \quad (3.10)$$

Combining (3.8) and (3.10) gives

$$m_t = nNP \times \hat{v} = \left(1 + 3 \left(\frac{R}{2r} - \frac{1}{2}\right) \left(\frac{R}{2r} + \frac{1}{2}\right)\right) \times \hat{v}, \quad (3.11)$$

which represents the total number of pMHC-TCR complexes formed as a result of binding by NPs.

The number of available NPs for binding is

$$s_f = s_{tot} - \alpha X_b, \quad (3.12)$$

where α represents the number of NPs bound to each T-cell. Substituting the steady state values from (3.3) and (3.4) for the number of NP-bound and free T-cells, we get

$$\begin{aligned} s_f &= s_{tot} - \alpha s_f \frac{b_{on}}{b_{off}} X \\ &= s_{tot} - \alpha s_f \frac{b_{on}}{b_{off}} \left(\frac{F(M-1)b_{on}s_f - \delta}{\varepsilon} \right) \implies \\ 0 &= \varepsilon s_{tot} + \left(\alpha \frac{b_{on}}{b_{off}} \delta - \varepsilon \right) s_f - \left(\alpha \frac{b_{on}}{b_{off}} F(M-1)b_{on} \right) s_f^2, \end{aligned}$$

where, $k = \frac{b_{on}}{b_{off}}$. This equation is quadratic in s_f which can be solved explicitly for the positive real root:

$$s_f = \frac{-(\alpha k \delta - \varepsilon) + \sqrt{(\alpha k \delta - \varepsilon)^2 + 4(\alpha k F(M-1)b_{on})(\varepsilon s_{tot})}}{2\alpha k F(M-1)b_{on}}. \quad (3.13)$$

Homeostatic competition is assumed to increase as T-cell population increase, induced by increasing dosage of NPs (NP-dependent increase in population size will increase competition between T-cells due to limited space [14]) and thus is set as a linear function of the total NPs injected, i.e.

$$\varepsilon = \varepsilon_1 s_{tot} + \varepsilon_2. \quad (3.14)$$

By combining Eqs. (3.5),(3.6), (3.11), (3.13), (3.14) with Eq. (3.4), we obtain:

$$\begin{aligned} X &= \frac{-(\alpha k \delta - \varepsilon) + \sqrt{(\alpha k \delta - \varepsilon)^2 - 4(\alpha k F(M-1)b_{on})(\varepsilon s_{tot})}}{2\alpha k \varepsilon} - \frac{\delta}{\varepsilon} \\ &= \frac{1}{2\alpha k} + \sqrt{\left(\frac{\delta}{2\varepsilon} - \frac{1}{2\alpha k}\right)^2 - \frac{F(M-1)b_{on}s_{tot}}{\alpha k \varepsilon} - \frac{2\delta}{\varepsilon}} \\ &= \frac{1}{2\alpha k} + \sqrt{\left(\frac{\delta}{2\varepsilon} - \frac{1}{2\alpha k}\right)^2 - \left(\frac{m_t}{a+m_t}\right) \left(\frac{(2^d-1)b_{on}s_{tot}}{\alpha k \varepsilon}\right) - \frac{2\delta}{\varepsilon}}. \end{aligned} \quad (3.15)$$

Equation (3.15) expresses the total number of free T-cells as a function of only model parameters. In the next section, we will address how these parameters are estimated.

Parameter	Meaning	Value	Ref.
a	pMHC concentration for half-maximum activation of T-cells	130 pMHC	[38]
d	Number of cell divisions per proliferating cell	6	[38]
δ	death rate of effector T-cells	$0.3s^{-1}$	[38]

Table 3-1: Values of known parameters

3.2 Parameter estimation

Based on previous work by Marée et al. [38], which studies competition between autoreactive T-cells in the pancreatic lymph nodes, we have published estimates of some of the parameters used in our model. In particular, the model Marée et al. developed to represent T-cell processes such as activation, death, and replicative potential are expected to be identical to those in our model. As such, these values were used for the known parameters (see Table 3–1). Of these parameters, the number of cell divisions per proliferating T-cell d is a well-studied quantity with consensus reached by several reports [44, 60, 62], the death rate of effector T-cells δ is calculated based on its lifespan [13], and the pMHC level at which half of the T cells become activated is a parameter estimated by Marée et al. [38].

The unknown parameters are those involved in the NP-binding and interaction with T-cells for which no previous work can be relied on. These parameters have been estimated using MCMC as described in Chapter 2 [22, 23]. The MCMC Toolbox (<http://helios.fmi.fi/~lainema/mcmc/>) created by Haario et al. was used to produce probability distributions of estimated parameters (Fig. 3–3) by fitting the steady-state population of free T-cells given by Eq. (3.15) to the experimental results shown in Fig. 1–2.

The outcomes of the MCMC estimation are displayed in Table 3–2. In the following sections, we will use the values of the parameters at the median (50th percentile) to simulate the total number of free T-cells. Moreover, Table 3–2 also displays the 90% confidence envelopes that have been generated using values of the

parameters at the 5th percentile and the 95th percentile. These envelopes enclosed all the data points generated experimentally.

Parameter	Meaning	Percentile		
		5	50	95
ε_1	Slope of competition	9.23×10^{-11}	2.20×10^{-10}	3.76×10^{-10}
ε_2	Basal level of competition	107	353	853
b_{on}	On-rate of NPs	0.39	0.53	0.69
$k = \frac{b_{on}}{b_{off}}$	Association constant	0.16	0.22	0.30
α	No. of NPs bound per cell	23	31	42

Table 3–2: Parameter values close to the median (50th percentile) and at the 90% confidence envelopes (between 5th percentile and 95th percentile).

3.3 Results

One important question that we would like to analyse is the role of valency in determining the efficacy of NPs in expanding T-cell population. In this section, we utilize the T-cell model, described by Eqs. (3.1) – (3.2) to address this question based on the parameter estimates obtained in the previous section. Our results show that the level of T-cell expansion does not vary greatly with varying valencies of NPs with 8 nm diameter core (28 nm diameter including pegylation described in Section 1.2). In fact, Fig. 3–4 shows that T-cell population plateaus at around 10^5 cells when stimulated with NPs coated with both 29 and as well as 61 pMHCs per NP. The 90% confidence envelopes show similar results. Using the model to explore the effect of modifying the size of the NPs, we found that at the same valency, larger NPs are worse at expanding the T-cell population compared to smaller NPs (Fig. 3–5). Interestingly, we also found that for small, 8 nm diameter

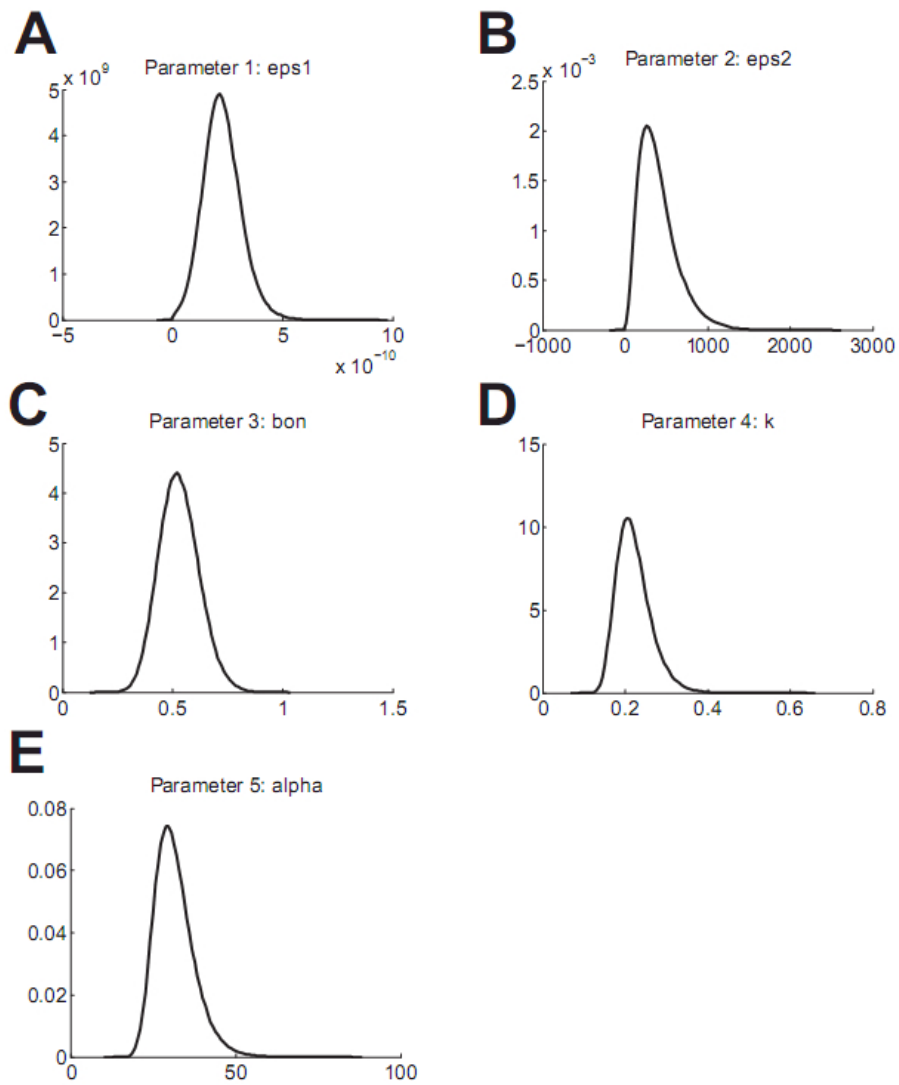


Figure 3-3: The distributions of the estimated parameters: **A)** ε_1 **B)** ε_2 **C)** b_{on} **D)** $k = b_{on}/b_{off}$ and **E)** α from MCMC [22].

NPs, the maximum level of expansion remains at 1.2×10^5 cells when expanded with either 20 or 61 pMHCs per NP. Using the larger, 40 nm diameter NPs, the expansion reaches a maximum of 7×10^4 cells at the higher valency while at the lower valency, the level of expansion only reaches a maximum of 4×10^4 cells. The model seems to support the hypothesis that beyond a certain valency threshold, increasing the number of pMHCs per NP has no effect on the maximal expansion level, and that this threshold depends on the size of the NPs. Moreover, for small, 8 nm diameter NPs, increasing the valency does not improve the level of T-cell expansion. However, for larger 40 nm diameter NPs, 20 pMHCs per NP appears to be below the threshold for effective T-cell activation, whereas a valency as high as 61 pMHC per NP is more effective at T-cell activation and proliferation.

Analysis of Eq. (3.15) to understand why valency does not seem to matter while NP size is important shows that both factors play a role in determining a single term, m_t , given by Eq. (3.11). From Eq. (3.11), we conclude that m_t is linearly proportional to valency and inversely proportional to the square of the NP radius, i.e.

$$m_t \propto v \quad \text{and} \quad m_t \propto 1/r^2. \quad (3.16)$$

This means that m_t depends quadratically on $1/r$ and linearly on v , making it much more sensitive to changes in NP size than valency. In other words, variations in valency are inconsequential while variations in NP size can induce more than 2-fold change in T-cell proliferation. Other parameters may have similar effects by are not investigated here.

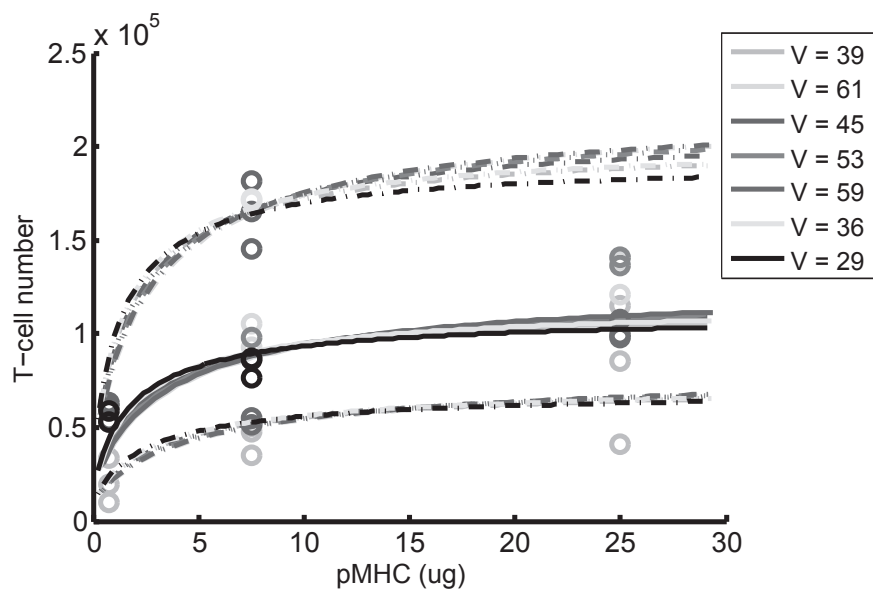


Figure 3–4: Model simulation of T-cell expansion as a function of NP dose graphed for various NP valency fitted to experimental data of proliferation from injection with 20 nm diameter NPs. The solid lines show the mean and the dotted lines are the 90% confidence envelope for each data series. The legend shows the color-coding employed to represent each valency level (v).

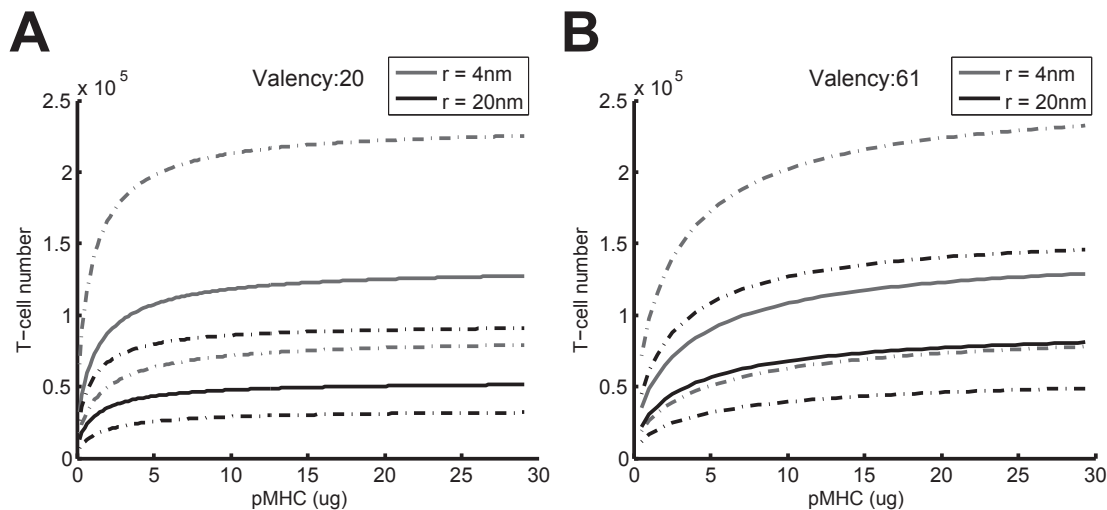


Figure 3-5: Model predictions of T-cell proliferations comparing stimulation by small 4 nm radius (gray) and large 20 nm radius (black) NPs at two valencies: **A)** 20 pMHCs per NP and **B)** 61 pMHCs per NP). The solid lines show the mean and the dotted lines are the 90% confidence envelopes.

The outcome of this mathematical model predicts that the optimal pMHC-NP design (i.e. the one displaying the highest T-cell expanding properties) would consist of small NPs, even when coated at lower valencies than their larger counterparts. In other words, it predicts that pMHC-NPs designed according to these principles would have higher agonistic activity and T-cell expansion capacity at lower doses of total pMHC (i.e. smaller, low valency NPs at lower NP doses is more effective than larger, high valency NPs at high doses).

These predictions were tested experimentally by comparing the autoregulatory T-cell expanding properties of 20 nm and 8 nm diameter NPs coated with pMHCs (see the unpublished data in Fig. 3-6). Studies using 8 nm preparations carrying 22 – 44 pMHCs/NP indicated significantly higher autoregulatory T-cell expanding

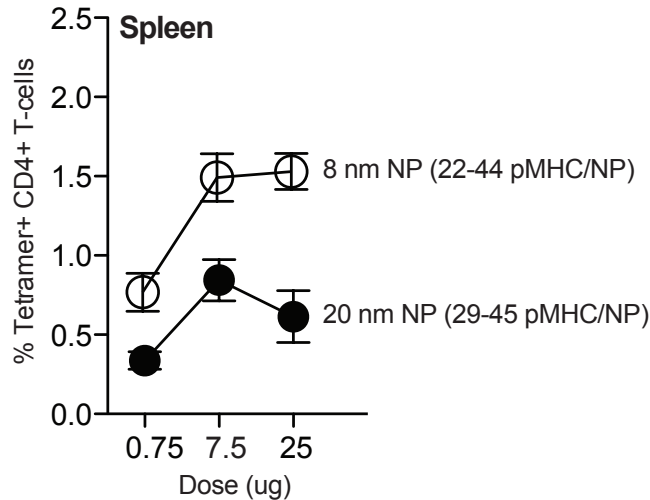


Figure 3-6: Autoregulatory CD4⁺ expansion potency of 8 nm core NPs compared to 20 nm diameter core NPs at similar valencies and dose.

effects, at all doses tested (0.75 μ g, 7.5 μ g and 25 μ g of total pMHC/dose), than 20 nm diameter particles carrying 29 – 45 pMHCs/NP (Fig. 3-6). Experiments testing the autoregulatory T-cell expansion properties using 8 nm diameter NPs carrying 7 different valencies between 29 – 61 pMHCs/NP (Fig. 1-2) showed clear dose-dependent effects for each individual valency, but no significant differences within the range of pMHC valencies tested.

Collectively, these results support the idea that pMHC density is a critical parameter in the design of pMHC-based nanomedicines. Thus, the *in vivo* therapeutic potency of these compounds (smallest dose required to yield meaningful expansions) is clearly more a function of pMHC density and dose than valency. This is significant because high-density coating significantly reduces the total amount of pMHC required to induce therapeutic levels of regulatory T-cell expansion *in vivo*.

CHAPTER 4

Model of *in vitro* activation

In this chapter, we use mathematical models to understand the activation of naïve T-cells treated *in vitro* with pMHC-NPs of various valencies, sizes and concentrations as described in Section 1.2.2. We make a more detailed examination of the binding kinetics of pMHC-NP on T-cells, including a thorough treatment of the observed phenomenon of NP cluster formation shown in Fig. 1–3. Whereas Chapter 3 treated the binding and unbinding of pMHC-NPs using terms involving one single parameter, b_{on} and b_{off} respectively, the controlled environment of *in vitro* stimulation without cell proliferation or death allows us to incorporate more factors that influence NP-binding and study it in finer time scales. Our modeling approach is used to understand key biophysical parameters of pMHC-NP interaction with T-cells.

4.1 Model of cluster binding

We know that the NPs bind to the surface of T-cells in clusters and that there are multiple clusters per cell (Fig. 1–3). We begin by modeling the cluster binding to cells as a Markov model in which each state represents the class of T-cells with certain number of NP-clusters bound to them, and the transition between two states represents the gain or loss of one cluster at a time. The maximum number of clusters that can be bound to each cell should be finite. Within the Markov model, two types of T-cells are considered: unactivated and activated

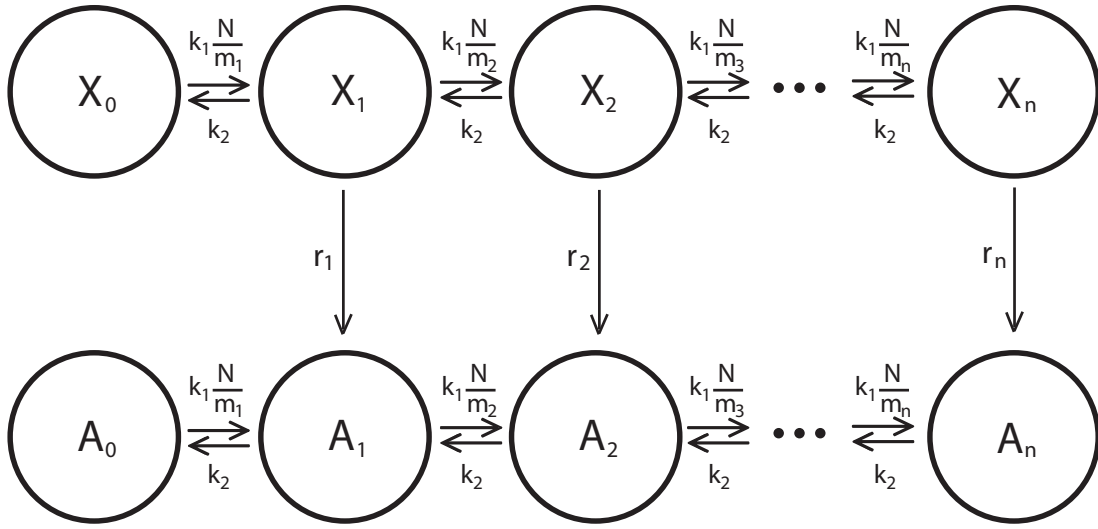


Figure 4-1: Markov model of nanocluster serial binding and swallowing.

T-cells. Transitions from unactivated to activated T-cells occur as a function of the number of clusters bound as well as the number of NPs per cluster. From these consideration, we generated the schematic diagram of the Markov model shown in Fig. 4-1.

In the Markov model, we let X_i and A_i represent the fraction of unactivated and activated T-cells, respectively, with i clusters bound, N denote the number of free NPs, and m_i represents the number of NPs in the i -th cluster. For simplicity and as an approximation, we assume that $m_i = m$ so every cluster has the same number of NPs. The kinetics of binding is given by the cluster binding rate k_1 . We consider the unbinding of clusters to be negligible. Clusters can only be removed through internalization (and digestion) with rate k_2 . T-cells transition from the unactivated to activated state with rates r_i , where $r_{i+1} \geq r_i$. The maximum

number of clusters that can form on T-cells is n . Based on this, the corresponding ODE model of this system is:

Model 1: Serial Swallowing

$$\frac{dX_0}{dt} = -k_1 \frac{N}{m} X_0 + k_2 X_1 \quad (4.1)$$

$$\frac{dX_i}{dt} = -k_1 \frac{N}{m} X_i + k_2 X_{i+1} + k_1 \frac{N}{m} X_{i-1} - k_2 X_i - r_i X_i \quad (4.2)$$

$$\frac{dX_n}{dt} = k_1 \frac{N}{m} X_{n-1} - k_2 X_n - r_n X_n \quad (4.3)$$

$$\frac{dA_0}{dt} = -k_1 \frac{N}{m} A_0 + k_2 A_1 \quad (4.4)$$

$$\frac{dA_i}{dt} = -k_1 \frac{N}{m} A_i + k_2 A_{i+1} + k_1 \frac{N}{m} A_{i-1} - k_2 A_i + r_i X_i \quad (4.5)$$

$$\frac{dA_n}{dt} = k_1 \frac{N}{m} A_{n-1} - k_2 A_n + r_n A_n \quad (4.6)$$

$$\frac{dN}{dt} = -k_1 N \sum_{i=0}^{n-1} (i+1) (X_i + A_i), \quad (4.7)$$

where $i = 1, \dots, n-1$. Note that $A_n = T_{tot} - \sum_{i=0}^{n-1} (X_i + A_i) - X_n$ since the total number of T-cells remains constant (T_{tot} is the total number of T-cells).

4.1.1 IFN γ production kinetics

The model Eqs. (4.1) – (4.7) describe the number of cells in various states of binding and activation. The readout for this activation is the amount of IFN γ in ng/ml produced by T-cells as detected by ELISA. In order to fit the mathematical model to experimental data, we will need to determine the relationship between the number of cells in an activated state and the amount of IFN γ that would be produced by these activated cells. Campbell et al. [6] and Schuerwegh et al. [48] are two experimental reports that study T-cell activation via the detection of IFN γ produced. In the same experiments, the authors present quantification

of number of activated T-cells (defined as cells that express IFN γ intracellularly) obtained using Fluorescence-activated cell sorting (FACS). Both papers show that the relationship between the number of IFN γ ⁺ T-cells and the amount of IFN γ excreted to the medium to be exponential. We prefer using Campbell et al.'s results for the following reasons:

1. Campbell et al. reported the cell number and concentration (2×10^6 cells/ml) in the methods section as opposed to using blood volume as in Schuerwegh et al. which contains a variable number of cells.
2. The stimulant used by Campbell et al., Staphylococcus enterotoxin B (SEB), activates T-cells by binding to multiple TCRs in an antigen-indiscriminant manner. This mechanism triggers TCR-proximal signaling events similar to the antigen-specific binding of TCRs to pMHCs. This differs from the use of PMA/ionomycin¹ in Schuerwegh et al., which activates the downstream ERK pathway directly without activating upstream signaling.
3. Campbell et al. incubated the cells for 20 hours, a time course that is closer to the 48 hour incubation time used in our experimental data than the 6-hour stimulation used by Schuerwegh et al. Part of the reason for the difference in time duration used between the two groups is due to the difference in kinetics of activation as a result of the two stimulants.

¹ PMA is a small organic compound that can diffuse through the cell membrane into the cytoplasm, where it directly activates Protein Kinase C (PKC). Ionomycin, a calcium ionophor, triggers calcium release.

4. Campbell et al. used ELISA to detect of extracellular IFN γ , the same method used in the experimental results that we are interested in fitting, while Schuerwegh et al. used beads.

By plotting T-cell number and IFN γ detected on a log-log plot, Campbell et al. reported a linear fit with a slope of 2.5 (CI 1.0 - 3.1) for healthy human subjects (Fig. 4b from [6]), which means that the amount of extracellular IFN γ produced as a function of the number of IFN γ^+ T-cells is of the form $y = cx^{2.5}$, where x is the number of IFN γ^+ cells and y is the amount of IFN γ produced in ng/ml.

We verified these results by digitizing the data from Fig. 4b in [6] and fitting a power trend line. Our results showed similar outcomes to those obtained for R^2 and exponential relationship presented in [6]. This allowed us to estimate the value of the unreported constant c in the equation. More specifically, we found that the best fitting trend line to the data was given by the equation:

$$y = 4.47 \times 10^{-13} x^{2.53}. \quad (4.8)$$

4.1.2 Activation kinetics of T-cells

We consider the activation rate r_i of T-cells to be affected by three factors: a rate constant κ in units of hr^{-1} , a probability function P_i , assumed to be monotonic with respect to the number of bound clusters i , and the activation due to the number of pMHCs making contact with TCRs on the T-cell surface F . The rate of transition from an unactivated state X_i to the activated state A_i is thus given by:

$$r_i = \kappa P_i F(m, v). \quad (4.9)$$

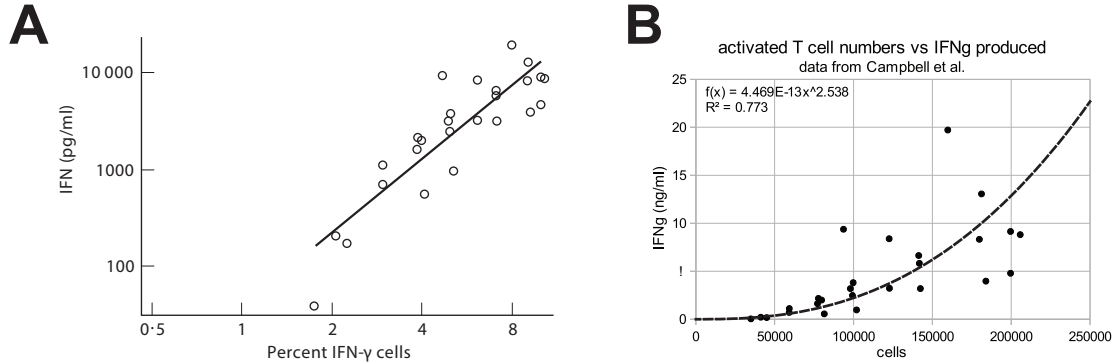


Figure 4-2: Quantifying the relationship between the number of activated IFN γ^+ T-cells following stimulation and the amount of IFN γ these cells excrete in the medium. Panel **A**) is a reproduction of Fig. 4b from Campbell et al. [6] used with permission from the publisher and **B**) is the same data displayed on a linear scale showing the equation of the best fitting trend line.

Estimating κ

If we were to consider activation to follow some sigmoid function of the stimulant with a maximum rate, then that maximum would be described with κ . Within our experimental paradigm, we do not have the necessary time-course data to be able to identify what value κ should take. Experimental data by Caraher et al. [7] can offer some insights. The authors stimulated splenocytes, which contains a mix of T-cells, B-cells, and APCs, with different concentrations of PMA/ionomycin over a period of 8 hours, and quantified the amount of activated IFN γ^+ cells using FACS in two-hour intervals. This information on the kinetics of activation was used to estimate κ . However, much like the previous section, we expect, by bypassing all upstream activation, stimulation with the potent PMA/ionomycin to lead to much faster activation compared to TCR-stimulation. We can therefore assume, with a certain level of accuracy, that the

effect of PMA/ionomycin can be quantified by the maximum activation rate κ , and that this effect is separate from F_p which describes the stimulation due to PMA/ionomycin that depends on its own set of parameters. In other words, we can model the activation of T-cells in the following way:

$$\frac{dA}{dt} = \kappa F_p (A_{tot} - A), \quad (4.10)$$

where A is the number of activated T-cells, A_{tot} is the maximum percentage of T-cells that can be activated, F_p describes PMA/ionomycin-specific effects and κ is the maximum activation rate underlying the process of T-cell activation (assumed to be identical to κ expressed in Eq. (4.9), because they represent the same effect). We define F_p to be:

$$F_p(P) = \frac{P^n}{k^n + P^n}, \quad (4.11)$$

where P is the concentration of PMA, k is the half-activation constant, and n is the Hill coefficient. Combining Eqs. (4.10) and (4.11), we obtain the following equation for PMA-dependent T-cell activation:

$$\frac{dA}{dt} = \kappa \frac{P^n}{k^n + P^n} (A_{tot} - A). \quad (4.12)$$

Equation (4.12) is a simple linear ODE with initial condition $A(0) = 0$, and an analytical solution given by:

$$A(t) = A_{tot} \left(1 - e^{-\kappa \frac{P^n}{k^n + P^n} t} \right). \quad (4.13)$$

Fitting this model to the data from Fig. 4a in [7], we found that the activation rate κ attains a mean value of 0.2 hr^{-1} , as shown in Fig. 4-3.

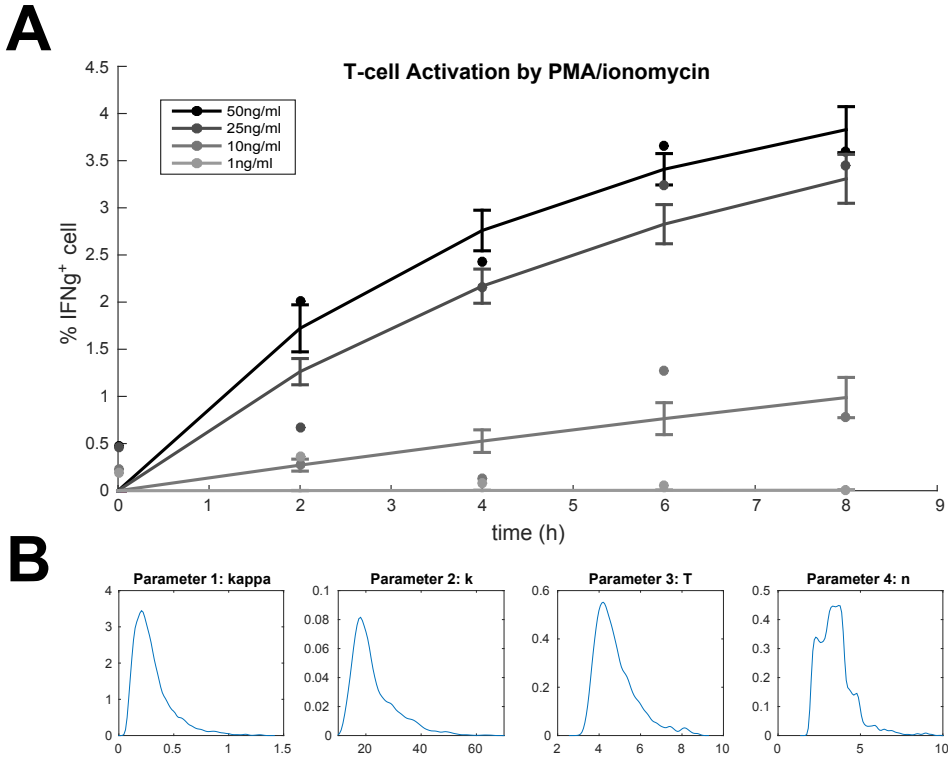


Figure 4-3: **A**) Fitting of T-cell activation using various concentrations of PMA, published in [7] (circles), to the model given by Eq. (2.16) (line). Graph shows the mean and standard deviation of 100 simulation using randomly drawn parameters from the stationary distribution. **B**) Distribution of estimated parameters κ , k , T and n .

Probability of activation P_i

As more NP-clusters bind to the T-cell surface, we expect these cells to more likely become activated. We also expect such a binding to follow saturating kinetics since the formation of enough NP-clusters on T-cells to eventually reach its maximum rate of activation. As a result, we choose a sigmoidal function to

represent the effect of multiple cluster-binding P_i , described by:

$$P_i = \frac{i}{p+i}, \quad (4.14)$$

where i is the number of bound clusters and p is the number of clusters required to reach the half-maximum probability of activation.

Activation by NPs $F(m, v)$

T-cells activation is mediated by TCR binding to pMHC, initiating a signaling cascade. We again use Marée et al's formalism of T-cell activation in [38], where the strength of the signal is thought of as a Hill function with Hill coefficient $n = 2$ that depends on the number of TCR-pMHC complexes formed. In any cluster, there are \hat{v} pMHCs exposed to the T-cell surface for each NP bound, where \hat{v} is the effective pMHC delivered as described in Eq. (3.10). Since there are m NPs in each cluster, there are $m\hat{v}$ pMHCs being delivered to the T-cell. Thus we can express the activation of T-cells by the action of pMHC-TCR binding as:

$$F(m, v) = \frac{(m\hat{v})^2}{a^2 + (m\hat{v})^2}, \quad (4.15)$$

where a is the concentration for half-maximum activation.

Combining equations (4.9), (4.14), and (4.15), we can express the activation rate of T-cells with i clusters bound by

$$r_i = \kappa \left(\frac{i}{p+i} \right) \left(\frac{(m\hat{v})^2}{a^2 + (m\hat{v})^2} \right). \quad (4.16)$$

4.2 Parameter estimation with data fitting

Similar to Section 3.2, we have a mix of known parameters from previous published results and newly defined parameters unique to the model described by Eqs. (4.1) – (4.7). We use Marée et al.’s estimate of $a = 130$ pMHC/cluster, where a is the pMHC concentration for half-maximum activation [38]. There are other kinetic parameters involved in NP-T-cell interaction; namely, the binding rate of a NP cluster given by k_1 , the swallowing rate of a NP cluster k_2 , the size of each NP cluster m , and the maximum number of clusters that bind n , as well as a set of kinetic parameters involved in T-cell activation; namely, the rate of T-cell activation κ and the number of clusters bound for half maximum probability of activation p . These are estimated using MCMC methods as described in Chapter 2. Since we have no prior knowledge for any of these parameters except for κ , their prior distributions will be set to a uniform distribution. With the knowledge of κ gained in Section 4.1.2 (Fig. 4–3), we defined the prior of κ to be Normally distributed with mean 0.2 and standard deviation 0.1.

4.2.1 Error function

To implement MCMC methods using MCMC Toolbox (<http://helios.fmi.fi/~lainema/mcmc/>) as described in Section 2.3, we needed to provide a proper sum-of-square error function. Other aspects of the algorithm such as size of update (Step 2), acceptance-rejection decision making (Step 3-5), and termination criteria (Step 6) have already been provided by the Toolbox itself.

Numerical solutions to $X_i(t)$, $A_i(t)$, and $N(t)$ were obtained by solving Eqs. (4.1) – (4.7) using the ODE solver `ode15s` built in MATLAB. The system was

numerically solved for 48 hours, the length of the experimental incubation time. Equation (4.8) was then used to find the amount of IFN γ produced s_{INF} based in model simulations, given by:

$$s_{INF} = 4.47 \times 10^{-13} \left(\sum_{i=0}^n A_i(48) \right)^{2.53}. \quad (4.17)$$

To assess the goodness of fit, a least-square error measure was used. The use of absolute error was not very successful since the amount of IFN γ produced ranged between 0.005 ng/ml - 2.9 ng/ml. From a numerical perspective, large fold changes produce very small numerical differences in absolute error, unlike relative error. However, the latter is very lax to variations at the higher NP doses, but creates a very tight fit to lower doses. We lack experimental repetitions to calculate variance in the data, making it infeasible to use the normal sum-of-square error presented in Eq. (2.12). However, since the exact value of the standard deviation σ is not critical, we can construct our own error function which incorporates more appropriate normalizing factor. More specifically, we use

$$error \equiv \chi^2 = \frac{(Data - s_{INF})^2}{\arctan^2(Data/2)}, \quad (4.18)$$

where $\arctan^2(Data/2)$ is an approximation for $2\sigma^2$, and s_{INF} is given by (4.17). To account for the number of data points available for fitting, the sum-of-squares error was normalized to the number of available data points.

4.2.2 MCMC fitting results

We implemented the MCMC Toolbox created by Haario et al. (<http://helios.fmi.fi/~lainema/mcmc/>), using the error function in Eq. (4.18), to estimate the parameters involved in NP-T-cell interaction, as well as the parameters involved in the activation of T-cells (see Section 4.2).

A summary of the parameters sampled, initial guesses (Initiation Step in Section 2.2.1), their ranges, and priors is provided as output by the Toolbox (Fig. 4–4). To take for computational and convergence time into consideration, we set the MCMC algorithm (see Chapter 2) to run for 20 000 iterations.

```
Sampling these parameters:
name      start [min,max]      N(mu,s^2)
k1:       1e-06 [1e-15,1]   N(0,Inf)
k2:       1e5   [500,1e+07] N(0,Inf)
kappa:    0.2   [0.1,0.7]   N(0.2,0.1^2)
n:        10   [2,50]    N(0,Inf)
m:        50   [3,300]   N(0,Inf)
p:        1    [0,100]   N(0,Inf)
```

Figure 4–4: The output of the MCMC Toolbox showing the parameters sampled, starting points, their ranges, and priors. $N(0, \text{Inf})$ means the distribution is uniform.

The results of the fitting (Fig. 4–5) converged reasonably well to data observed in Fig. 1–4, implying a level of validity in the model development from which further analysis is pursued. The model accurately captured the “threshold” effect, whereby low-valency NP were unable to induce significant $\text{IFN}\gamma$ production even at high doses whereas low dose of high-valency NP were much more effective at inducing $\text{IFN}\gamma$ production. For an 8 nm diameter core NP with 10 nm layer

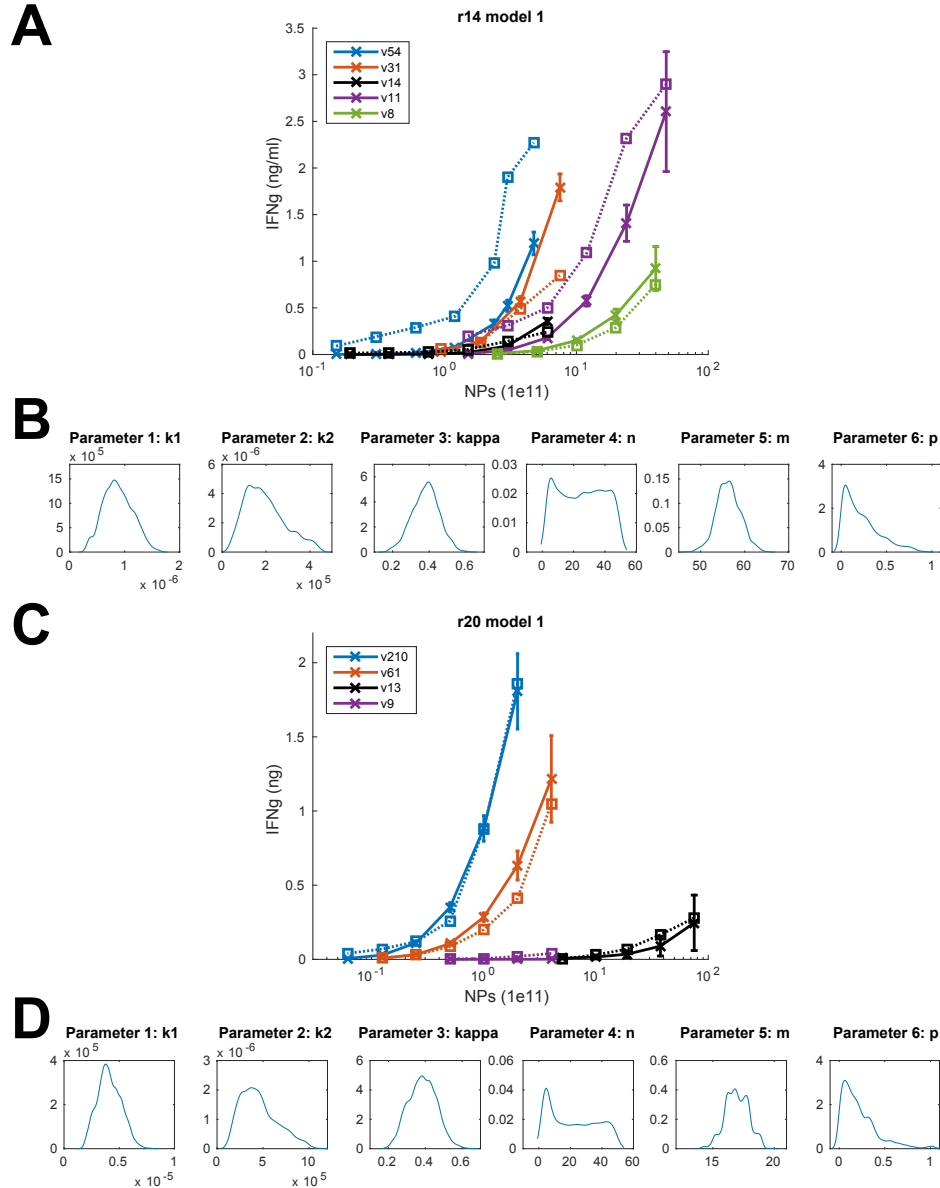


Figure 4-5: Fitting the INF γ data of Fig. 1-4 to model simulations. INF γ production by T-cells stimulated with pMHC-NPs with radius **A**), **B**) 14 nm and **C**), **D**) 20 nm coated with various valencies were fitted to the model given by Eqs. (4.1) – (4.7), where **B**) and **D**) show the distributions of estimated parameters according to their respective NP-size. Panels **A**) and **C**) show mean and standard deviation of model predictions using 100 random draws from the parameter distributions depicted in **B**) and **D**), respectively.

of pegylation (as described in Section 1.2), the NP radius r is 14 nm (r14), while larger NPs with a 20 nm diameter core with the same amount of pegylation, the radius r is 20 nm (r20). The modes of the distribution are listed in Table 4–1. To determine the spread of data, we numerically solved Eqs. (4.1) – (4.7) using 100 randomly selected parameter sets to obtain the mean and standard deviation of the model prediction as shown in Fig. 4–5.

Parameter	14 nm radius NP	20 nm radius NP
k_1	7.69×10^{-7}	3.67×10^{-6}
k_2	1.275×10^{-5}	2.51×10^5
κ	0.37	0.38
n	4	4
m	56	16
p	0.04	0.05

Table 4–1: Table showing the modes of the parameters corresponding to Eqs. (4.1) – (4.7) as determined by the MCMC toolbox.

4.3 Mathematical analysis

A key question we are trying to answer about this system is what design of NPs, with respect to *valency* and *radius*, would result in the most amount of T-cell activation (and by extension, amount of IFN γ produced). The typical approach to these problems is to find the steady state and perform bifurcation analysis to examine how this steady state changes as we modify each of these two parameters of the system. However, the system described by Eqs. (4.1) – (4.7) has non-isolated and infinite number of steady states, where different initial conditions lead to different steady states. We will show here the existence of non-isolated steady states by solving for the fixed points of the system.

To solve for the steady state of Eq. (4.7), we set:

$$\frac{dN}{dt} = -k_1 N \sum_{i=0}^{n-1} (i+1) (X_i + A_i) = 0. \quad (4.19)$$

The non-negative physiological solutions to this equation are either (i) $X_i = A_i = 0$, for $i = 0, \dots, n-1$, since $X_i, A_i \geq 0$, or (ii) $N = 0$.

Case 1: Using solution (i) where $X_i = A_i = 0$ and $N \neq 0$, we deduce using Eqs. (4.3) and (4.6) that:

$$0 = \frac{dX_{n-1}}{dt} = k_2 X_n \quad (4.20)$$

$$0 = \frac{dA_{n-1}}{dt} = k_2 A_n, \quad (4.21)$$

which means that $X_n = A_n = 0$. Based on (i), it follows that

$$\sum_{i=0}^n X_i + A_i = 0. \quad (4.22)$$

However, this is not possible since it violates the condition that the total population of T-cells is conserved (i.e. no cell death processes are involved) and non-zero.

Thus we may conclude that solution (i) is not valid.

Case 2: Using the solution (ii) in which $N = 0$, we can show by induction that $X_i = 0, i = 1, \dots, n$ and $A_i = 0, i = 1, \dots, n$ using Eqs. (4.1) – (4.6). More specifically, according to Eq. (4.1), we have:

$$0 = \frac{dX_0}{dt} = -k_1 \frac{N}{m} X_0 + k_2 X_1 = k_2 X_1 \implies X_1 = 0. \quad (4.23)$$

For the induction step, we assume $X_i = 0$ for $i = 1, \dots, h$ for some $h < n$, then apply Eq. (4.2) to obtain:

$$0 = \frac{dX_h}{dt} = k_2 X_{h+1} \implies X_{h+1} = 0. \quad (4.24)$$

This concludes our proof showing $X_i = 0$, for $i = 1, \dots, n$. Similar arguments can be used to show that $A_i = 0$, for $i = 1, \dots, n$.

This analysis shows that in the system described by Eqs. (4.1) – (4.7), the only populations with non-zero steady state values are X_0 and A_0 . However, by employing solution (ii) along with Eqs. (4.1) and (4.4) we find that:

$$0 = \frac{dX_0}{dt} = -k_1 \frac{N}{m} X_0 + k_2 X_1 = (0)X_0, \text{ and} \quad (4.25)$$

$$0 = \frac{dA_0}{dt} = -k_1 \frac{N}{m} A_0 + k_2 A_1 = (0)A_0. \quad (4.26)$$

This means that X_0 and A_0 can take on any value at steady state as long as $X_0 + A_0 = T_{tot}$, and they cannot be calculated by analytical means. This is the characteristic of having steady states that are non-isolated and precludes the application of existing theories in bifurcation analysis.

4.4 Correlations

It is still possible to answer the question of optimizing the NPs without using bifurcation analysis per se, but applying the same principles by taking the level of activated T-cells at 48 hours of stimulation (rather than using steady state analysis), and evaluate how T-cell activation level changes with variations in the parameters. While it is mathematically possible to vary the value of each parameter k_1 , k_2 , m , and v independently of one another, it is unlikely that these

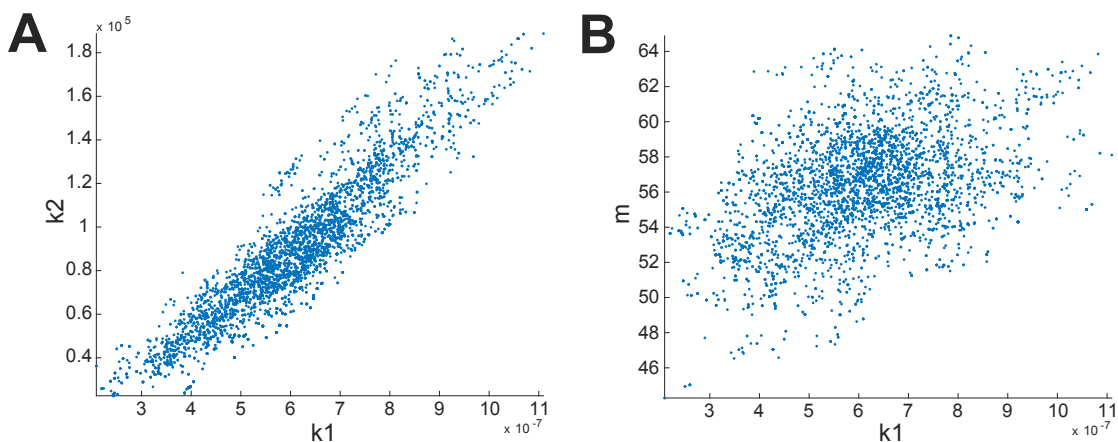


Figure 4-6: Joint distributions **A)** k_1 and k_2 showing linearly correlation and joint distribution of **B)** k_1 and m

parameters are mutually independent of each other physiologically. In fact, we can see from Fig. 4-6A of the joint density of k_1 and k_2 that they are linearly correlated. This is not surprising given that the ratio of these two parameters play a major role in controlling the steady state of the system. We expect other parameters in the system to be correlated as well. More precisely, the binding rate k_1 should be controlled by the size of the NP, which is encoded in the parameter m . This does not seem to be the case when we examine the joint distribution of k_1 and m shown in Fig. 4-6. However correlation becomes clearer when we fit the model to individual series of data generated using NPs of one valency (Fig. 4-7).

The plot of the joint densities of k_1 and m from MCMC fittings using unique combinations of NP size and valency v (Fig. 4-7) show a progressive change in the shape of this chain as v increases. The m vs k_1 relation is linear for low valency, but shifts to a Hill-like structure as valency increases. This trend is most obvious for smaller NPs, though it is similar for larger NPs as well. We excluded the

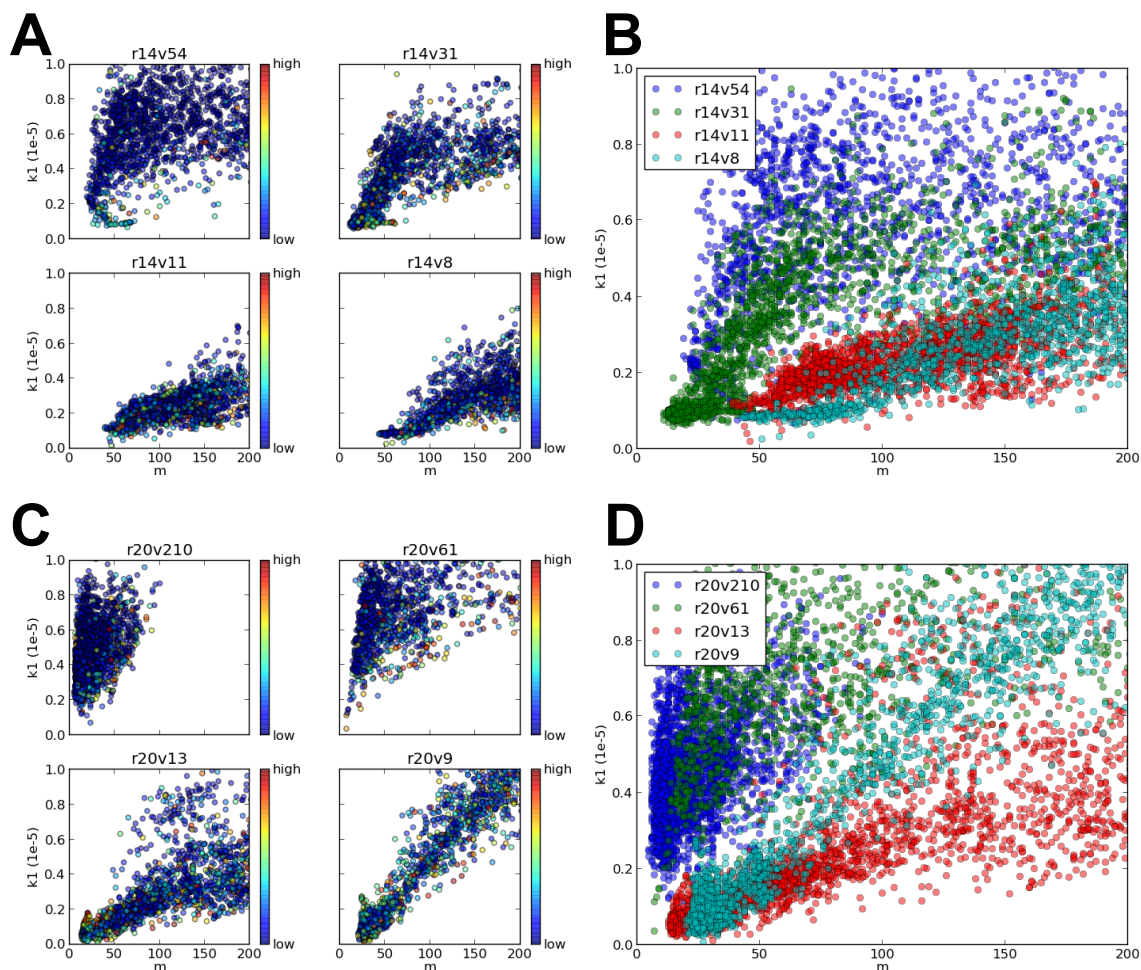


Figure 4–7: Joint distribution of k_1 and m according to several Markov chains obtained using one valency on **A)** 14 nm radius NP and **C)** 20 nm radius NP. The color of the dot indicates the relative error obtained at that particular parameter value. **B)** and **D)** show these chains obtained in panels **A)** and **C)** displayed on the same plot, respectively.

joint density for NPs of radius $r = 14$ nm and $v = 14$ pMHC/NP because it is considered an outlier based on the experimental result where at the same dosage of NPs, the amount of IFN γ secreted with 14 pMHC/NP was lower than that of 11 pMHC/NP. This may be a result of T-cell heterogeneity and experimental variability.

We postulate that there is a functional relationship between k_1 and both m and v . We can imagine the plots in Fig. 4–7A and 4–7C as planar slices of a surface in the (m, v, k_1) space. To better define this relationship, we require further analysis of the parameter distributions and use it to find some sort of non-linear function for k_1 in terms of m and v .

4.4.1 Filtering parameters for lowest errors

To best discern the relationship between the parameters k_1 , m and v , we limit our analysis to only the parameters sets that produce the least amount of error (as defined by Eq. (4.18)) in fitting. Analysis of the distribution of errors from the

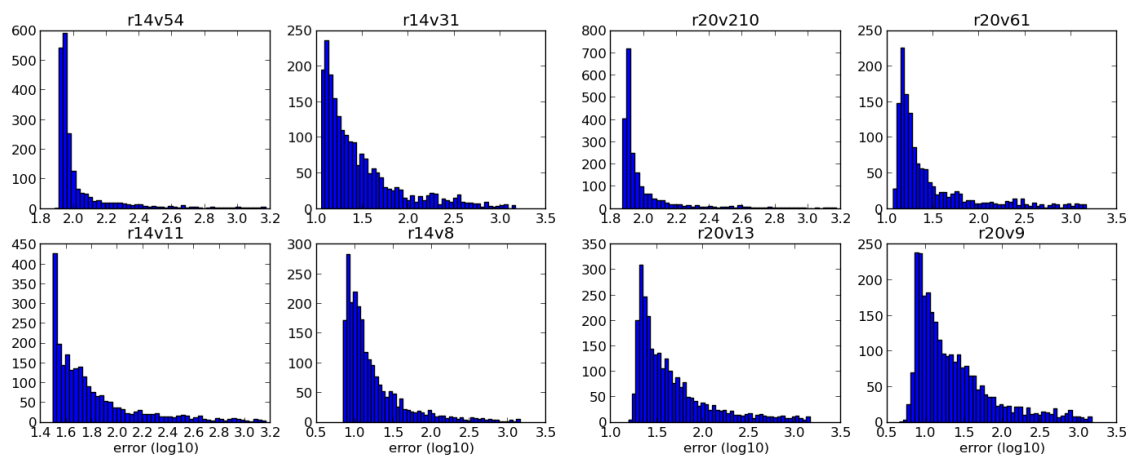


Figure 4–8: Distribution of error from MCMC fitting.

MCMC fitting in Fig. 4–8 is roughly exponentially distributed with some offset η , representing the minimal error attained, which is different for each radius-valency combination. To select the cutoff that filters for parameter producing fitting-error in the lowest 30th percentile, we need to construct quantile functions for the error distribution.

We model the error, χ^2 , as exponentially distributed random variables with density $f_{err}(\chi^2) = \lambda \cdot e^{-\lambda(\chi^2-\eta)}$, where η is an offset taken to be minimum fitting error attained. By letting μ be the sample mean (where $\mu = 1/n \sum \chi^2$) and using the Law of Large Numbers, we can conclude that

$$\mu \rightarrow \mathbb{E}(X) = \int_{\eta}^{\infty} x \lambda e^{-\lambda(x-\eta)} dx = \eta + \frac{1}{\lambda}. \quad (4.27)$$

From Eq. (4.27), we find $\lambda = \frac{1}{\mu - \eta}$, which is a known quantity that can be calculated from the sample mean and the minimum error attained. We use λ to calculate the cutoff, $Q(p)$, required to select for only the parameter sets that generate an error in the lowest $p = 30\%$ range as follows:

$$p = \int_{\eta}^{Q(p)} \lambda e^{-\lambda(x-\eta)} dx = 1 - e^{-\lambda(Q(p)-\eta)} \quad (4.28)$$

$$\log(1 - p) = -\lambda(Q(p) - \eta)$$

$$\frac{\log(1 - p)}{-\lambda} + \eta = Q(p). \quad (4.29)$$

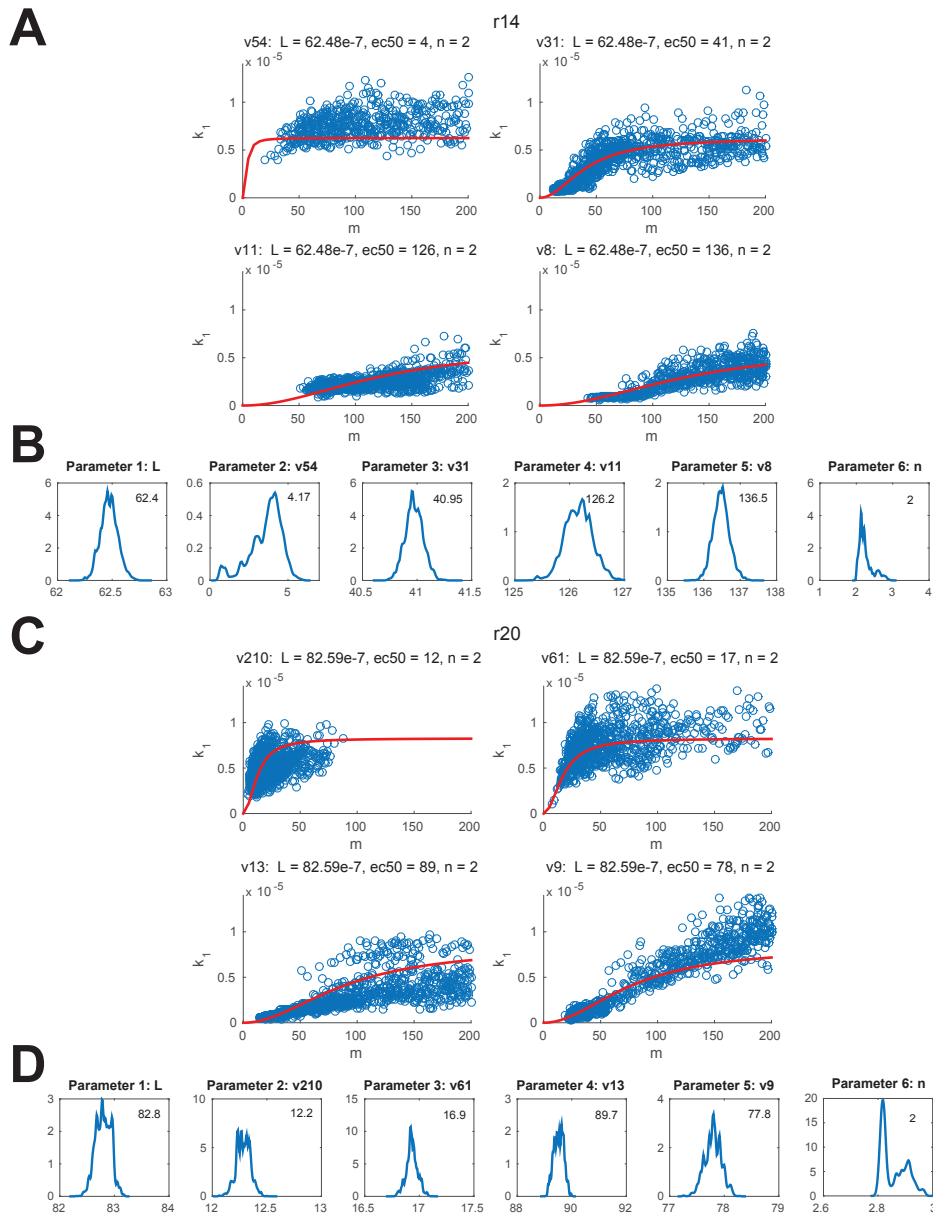


Figure 4–9: Fitting of Eq. (4.31) to the joint densities of k_1 and m displayed in Fig. 4–7. Panel **A**) and **C**) show the fitting (in red) to the Markov chains corresponding to pMHC-NPs of radius **A**) 14 nm and **C**) 20 nm. Panels **B**) and **D**) show the corresponding distributions of estimated parameters (L , ec_{50} for each NP valency, and the Hill coefficient n) for their respective NP-size.

To ensure that the MCMC fitting of k_1 , as a function of m , can account for very low variance in certain regimes (compared to larger spreads in others), we need calculate the variance (σ^2) at each value of m and scale the absolute error (err_{raw}) as follows:

$$err = \frac{err_{raw}}{2\sigma^2}. \quad (4.30)$$

This formulation is based on MCMC theory described by Eq. (2.12).

4.4.2 Cluster binding rate and cluster size by valency

As suggested earlier, panels A and C from Fig. 4–7 were thought to possess Hill-like characteristics, leading to the selection of the candidate function:

$$k_1 = L \frac{m^n}{(ec_{50})^n + m^n} \quad (4.31)$$

to describe the joint densities of k_1 and m , limiting the analysis for now to $k_1 - m$ relations only. We assume that the maximum L , in Eq. (4.31), to remain constant for each valency of the same NP-size (with each NP-size possessing a different maximum L). The half-maximum of activation, ec_{50} , would vary greatly between different valencies and radii of NPs analysed. The result of fitting Eq. (4.31) to the

Parameter	valency	14 nm NP	Parameter	valency	20 nm NP
L	all	62.4	L	all	82.8
ec_{50}	54	4.17	ec_{50}	210	12.2
	31	40.95		61	16.9
	11	126.2		13	89.7
	8	136.5		9	77.8
n	all	2	n	all	2

Table 4–2: Table of parameter estimates for fitting Eq. (4.31) to the joint distribution of k_1 and m in Fig. 4–9.

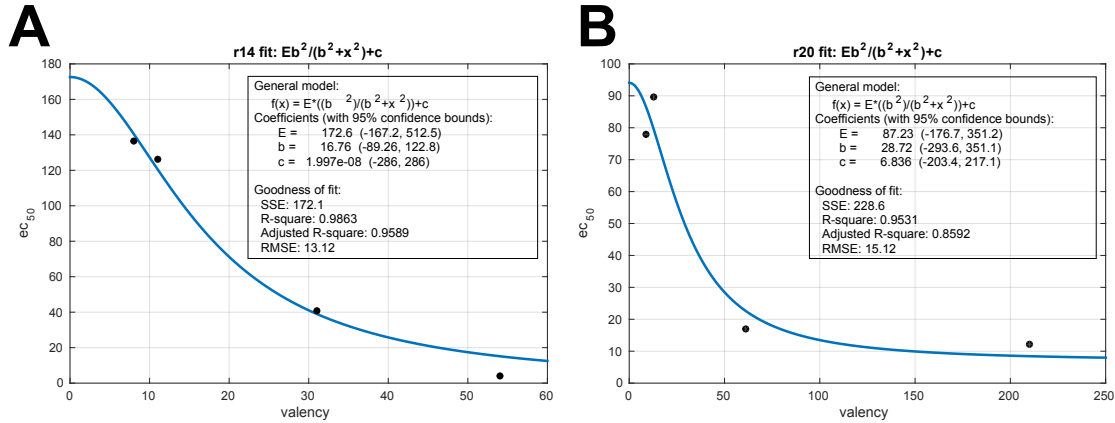


Figure 4–10: Fitting of a decreasing Hill function with coefficient $n = 2$ to the ec_{50} of k_1 – m fitting of **A)** 14 nm radius NPs and **B)** 20 nm radius NPs.

joint densities of k_1 and m (Fig. 4–7) after applying the error cutoff in Eq. (4.29) and scaling in Eq. (4.30) is shown in Fig. 4–9. In other words, Fig. 4–9 shows the fitting of Eq. (4.31) to only parameter sets that attain an error in the lowest 30th percentile as defined by the cutoff $Q(p)$.

4.4.3 ec_{50}

Fitting of Eq. (4.31) shown in Fig. 4–9 generated reasonable fits to the joint density of k_1 and m by only changing the ec_{50} of the Hill function for each valency of the NPs analysed. In effect, the ec_{50} can be viewed as a function of the valency, with higher valencies achieving lower values of ec_{50} (see Table 4–2). The plot of

Parameter	14 nm radius NP	20 nm radius NP
E	172.6	87.23
b	16.76	28.72
c	2×10^{-8}	6.83

Table 4–3: Table of parameter for fitting Eq. (4.32) to the ec_{50} from Table 4–2.

ec_{50} as a function of the valency (Fig. 4–10) shows a distinct trend. We use a simple least-square fit method to fit to the decreasing Hill function given by:

$$ec_{50} = E \frac{b^2}{b^2 + v^2} + c \quad (4.32)$$

to the ec_{50} values obtained in Fig. 4–9 using `cftool` in MATLAB, where E is the maximum possible value that the ec_{50} can be, b is the valency at which the half-maximum value of ec_{50} is attained, and c is a vertical offset (since it is not necessary that ec_{50} vanish as $v \rightarrow \infty$). This function creates an almost perfect fit as seen in Fig. 4–10 (see also Table 4–3). Substituting Eq. (4.32) in the proposed form for k_1 in Eq. (4.31), we obtain the complete expression of k_1 as a function of both the valency and the number of NPs per cluster:

$$k_1(m, v) = L \frac{m^n}{\left(E \frac{b^2}{b^2 + v^2} + c\right)^n + m^n}. \quad (4.33)$$

Using the expression in Eq. 4.33 to fit the distribution of k_1 , m , and v (Fig. 4–11), we find the estimates of the distribution of each parameter L (the maximum value k_1 attains), E (the maximum value ec_{50} attains), b (the valency at which half-maximum of ec_{50} is attained), c (the lowest possible ec_{50}), and n (the Hill coefficient for k_1) to be listed in Table 4–4. This has further implications as when analysing the individual NP binding dynamics.

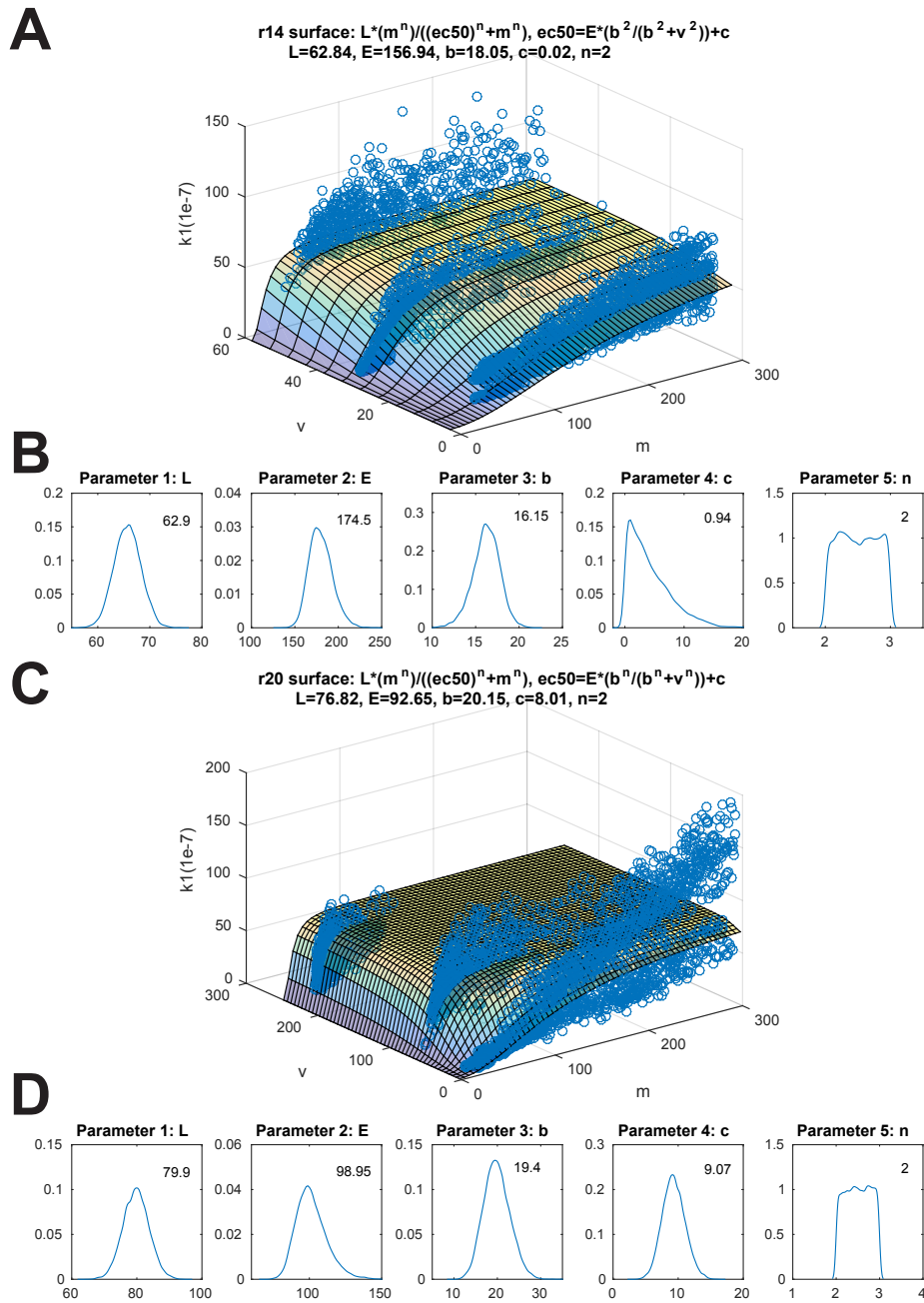


Figure 4-11: Fitting of Eq. (4.31) to the joint distribution of k_1 , m and v . Panel A) and C) show fitting to pMHC-NPs of radius A) 14 nm and C) 20 nm. Panels B) and D) show the corresponding distributions of estimated parameters (L , E , b , c , and the Hill coefficient n) for their respective NP-size.

Parameter	14 nm radius NP	20 nm radius NP
L	6.29×10^{-6}	7.99×10^{-6}
E	174.5	98.9
b	16.15	19.4
c	0.94	9.07
n	2	2

Table 4–4: Table of parameter for fitting k_1 as a function of m and valency.

4.5 Model of nanoparticle binding

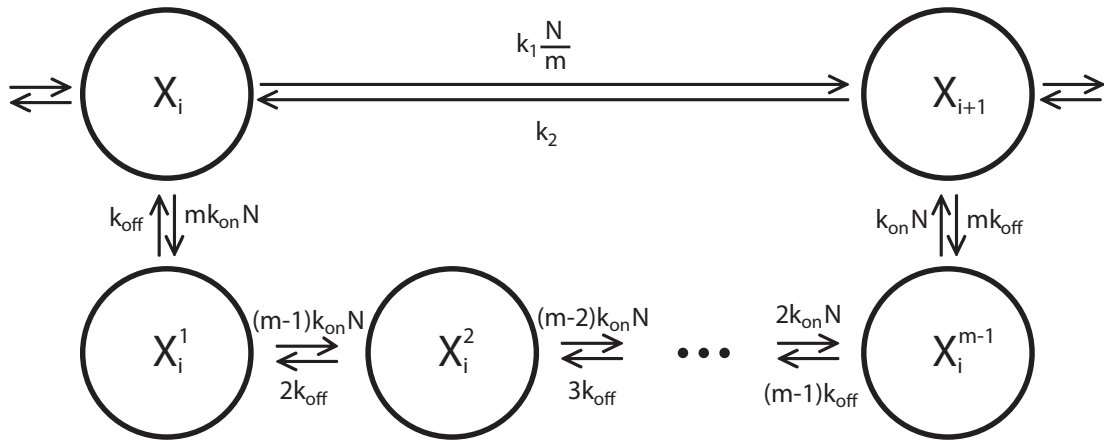


Figure 4–12: Model of NP-binding to T-cells in the process of forming a new cluster, depicted as a series of transitions representing single NP bindings within the Markov model of Fig. 4–1.

Recall how the schematic model of Fig. 4–1 depicts the Markov model of nanoclusters binding to T-cells, whereby transition between two states represent the gain and loss of a single cluster. Within this Markov model, a single transition step, i.e. the transition from X_i to X_{i+1} (or A_i to A_{i+1}), involves the binding of the m individual NPs that compose a new nanocluster. At the NP-binding level, we interpret a single transition step in the Markov model as an m -step binding

process represented by the schematic in Fig. 4–12. The transition at the single NP-binding is mediated by the binding rate k_{on} , and the NP unbinding rate k_{off} . X_i^j represents the number of T-cells with i clusters of NP bound, and j individual NPs in the process of forming a new cluster. Therefore, according to this notation, $X_i^0 \equiv X_i$ and $X_i^m \equiv X_{i+1}$.

4.5.1 NP binding rate

We use studies of multi-step chemical reactions [63] to understand how binding at the cluster level relate to individual NP binding. The observable quantities in chemical reactions are the products and the reactants. However, a reaction may involve multiple intermediary steps that are not observable. Understanding these intermediary steps of a chemical reaction require similar approach to unravel the intermediary NP-bindings underlying transitions within the Markov model.

Since the nanocluster digestion rate is much slower than the cluster binding rate, we may conclude that the transition time of $X_i^0 \rightarrow X_{i+1}^0$ at the supramolecular cluster binding level (Fig. 4–1) is given by

$$t_c = \frac{1}{k_1 N/m}. \quad (4.34)$$

At the NP-binding level, the unbinding of NPs is much slower than the binding. As a result, the transition time of $X_i^j \rightarrow X_i^{j+1}$ is given by the forward binding rate as:

$$t_j = \frac{1}{(m-j)k_{on}N}. \quad (4.35)$$

Since both transition through binding of a nanocluster in the supramolecular Markov model (Fig. 4–1) and the binding of m NPs as described through individual NP bindings (Fig. 4–12) is describing the same process, the transition times given by the nanocluster binding model in Eq. (4.34) is identical to the transition time given by m -steps through the NP-binding model, i.e.:

$$t_c = \sum_{j=0}^{m-1} t_j \implies \quad (4.36)$$

$$\frac{1}{k_1 \frac{N}{m}} = \sum_{j=0}^{m-1} \frac{1}{(m-j)k_{on}N} \implies$$

$$k_{on} = \frac{k_1}{m} \sum_{j=1}^m \frac{1}{j} = L \frac{m^{n-1}}{(ec_{50})^n + m^n} \sum_{j=1}^m \frac{1}{j}. \quad (4.37)$$

Equation (4.37), obtained by substituting Eq. (4.33) for k_1 , can be analysed by applying Riemann sum approximations to $\sum_{j=1}^m \frac{1}{j}$. By treating this summation as the Left Riemann Sum (LRS) or the Right Riemann Sum (RRS) approximation of the function $f(x) = 1/x$, a monotonically decreasing function, we find as the LRS

$$\sum_{j=1}^m \frac{1}{j} \geq \int_1^{m+1} \frac{1}{x} dx = \log(m+1) \quad (4.38)$$

and as the RRS

$$\sum_{j=1}^m \frac{1}{j} = 1 + \sum_{j=2}^m \frac{1}{j} \leq 1 + \int_1^m \frac{1}{x} dx = 1 + \log(m). \quad (4.39)$$

Substituting these bounds on the summation to Eq. (4.37), we establish upper and lower bounds on k_{on} as follows:

$$L \frac{m^{n-1}}{(ec_{50})^n + m^n} \log(m+1) \leq k_{on} \leq L \frac{m^{n-1}}{(ec_{50})^n + m^n} (1 + \log(m)). \quad (4.40)$$

Establishing these bounds using continuous functions provides an analytical tools to study the behaviour of k_{on} at its extreme values, i.e. when $m \rightarrow \infty$ and $m \rightarrow 0$.

upper bound: $k_{on} = L \frac{m^n}{(ec_{50})^n + m^n} \cdot \frac{1 + \log(m)}{m}$

By taking the limit as $m \rightarrow \infty$, we obtain:

$$\lim_{m \rightarrow \infty} k_{on} = \lim_{m \rightarrow \infty} L \frac{m^n}{(ec_{50})^n + m^n} \cdot \frac{1 + \log(m)}{m} = L \lim_{m \rightarrow \infty} \frac{1/m}{1} = 0. \quad (4.41)$$

At the other extreme, by taking the limit as $m \rightarrow 0$, we obtain:

$$\begin{aligned} \lim_{m \rightarrow 0} k_{on} &= \lim_{m \rightarrow 0} L \frac{m^{n-1}}{(ec_{50})^n + m^n} \cdot (1 + \log(m)) = L \lim_{m \rightarrow 0} \frac{1 + \log(m)}{(ec_{50})^n m^{1-n} + m} \implies \\ &= L \lim_{m \rightarrow 0} \frac{1/m}{(1-n)(ec_{50})^n m^{-n} + 1} = L \lim_{m \rightarrow 0} \frac{m^{n-1}}{(1-n)(ec_{50})^n + m^n} = 0. \end{aligned} \quad (4.42)$$

lower bound: $k_{on} = L \frac{m^n}{(ec_{50})^n + m^n} \cdot \frac{\log(m+1)}{m}$

Similarly, by taking the limit as $m \rightarrow \infty$, we obtain:

$$\lim_{m \rightarrow \infty} k_{on} = \lim_{m \rightarrow \infty} L \frac{m^n}{(ec_{50})^n + m^n} \cdot \frac{\log(m+1)}{m} = L \lim_{m \rightarrow \infty} \frac{\frac{1}{m+1}}{1} = 0, \quad (4.43)$$

and as $m \rightarrow 0$, we obtain:

$$\lim_{m \rightarrow 0} k_{on} = \lim_{m \rightarrow 0} L \frac{m^{n-1}}{(ec_{50})^n + m^n} \cdot (\log(m+1)) = 0 \cdot \log(1) = 0. \quad (4.44)$$

Applying the Squeeze theorem as $m \rightarrow \infty$ using Eq. (4.41) and Eq. (4.43), as well as when $m \rightarrow 0$ using Eq. (4.42) and Eq. (4.44), we obtain the following:

$$\lim_{m \rightarrow \infty} k_{on} = \lim_{m \rightarrow 0} k_{on} = 0. \quad (4.45)$$

We assume that k_{on} is a non-negative, non-constant function reaching its minimum at the boundary of its domain. As a result, there must be at least one maximum attained by k_{on} for some $m \in \mathbb{N}$. This maximum is not particularly easy to calculate analytically, since k_{on} is a function of the integer variable m . Standard methods of finding critical values by differentiation and solving for $\frac{dk_{on}}{dm} = 0$ cannot be applied. We can, however, numerically calculate the maximum by solving for k_{on} for $m \in [0, \infty)$ (Fig. 4–13) and obtain the value of m which produces the maximum k_{on} , i.e., derive:

$$m_{max} = \arg \max_m k_{on}. \quad (4.46)$$

Recall that the parameters m represents the number of pMHC-NPs binding to a cluster and v is the number of pMHCs on each NP. The m_{max} given by Eq. (4.46) depends on the valency (mathematically, this arises from k_1 , which is required to calculate k_{on} given by Eq. (4.37), being dependent on valency in Eq. (4.33)). In fact, within the range of m assessed ($m \in [1, 300]$ NPs/cluster), we find there is a unique m_{max} for each valency (see. Fig. 4–13). Varying valency v and finding the corresponding m_{max} , we can calculate the total number of pMHCs within each cluster when k_{on} is optimal to be:

$$pMHC_{max} = m_{max}(v) \times v. \quad (4.47)$$

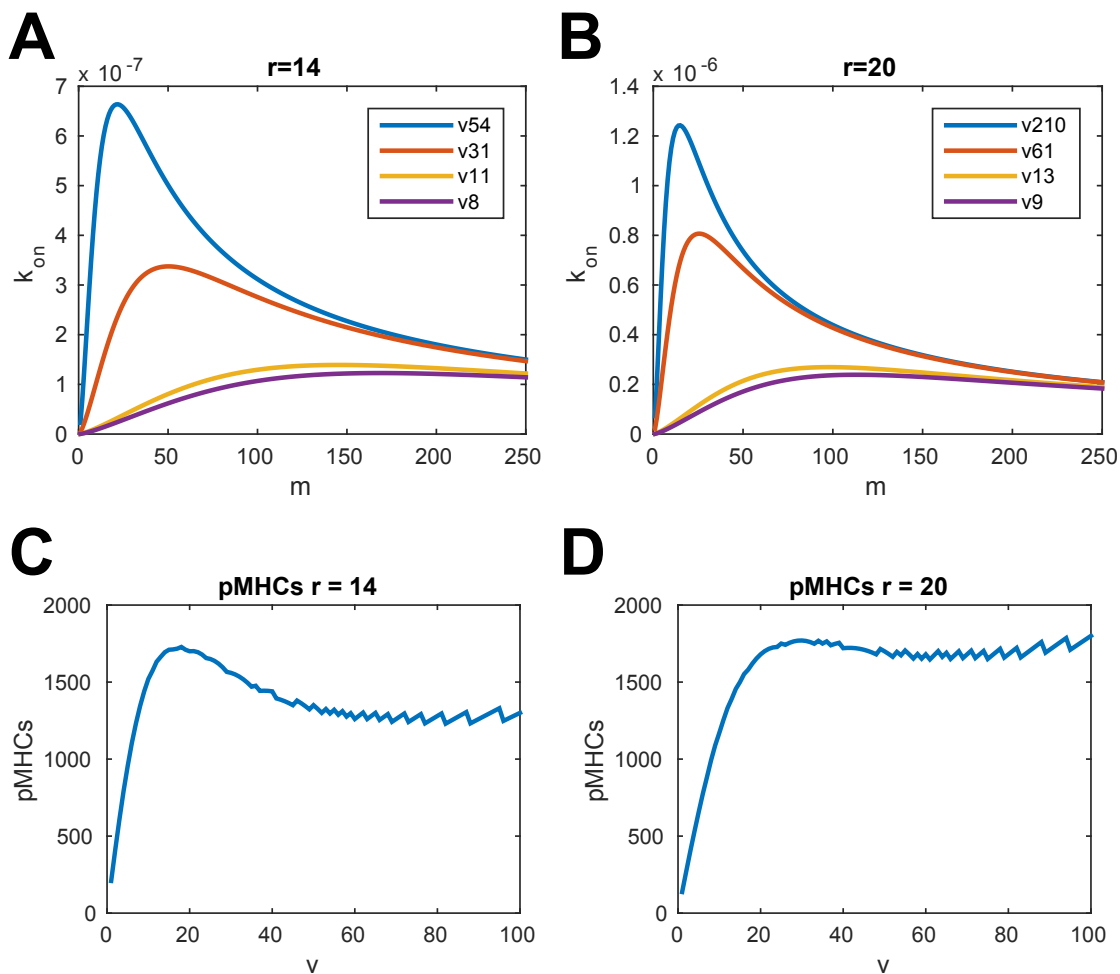


Figure 4-13: Numerical calculation of k_{on} using Eq. (4.37) for $m = 1, \dots, 250$ for **A)** 14 nm radius NP coated with 54 (blue), 31 (red), 11 (yellow), and 8 (purple) pMHCs/NP and **B)** 20 nm radius NP coated with 210 (blue), 61 (red), 13 (yellow), and 9 (purple) pMHCs/NP. Panels **C)** and **D)** show the number of pMHCs presented at each cluster ($pMHC_{max}$) when the optimal k_{on} is attained for NP of radius **A)** 14 nm and **B)** 20 nm.

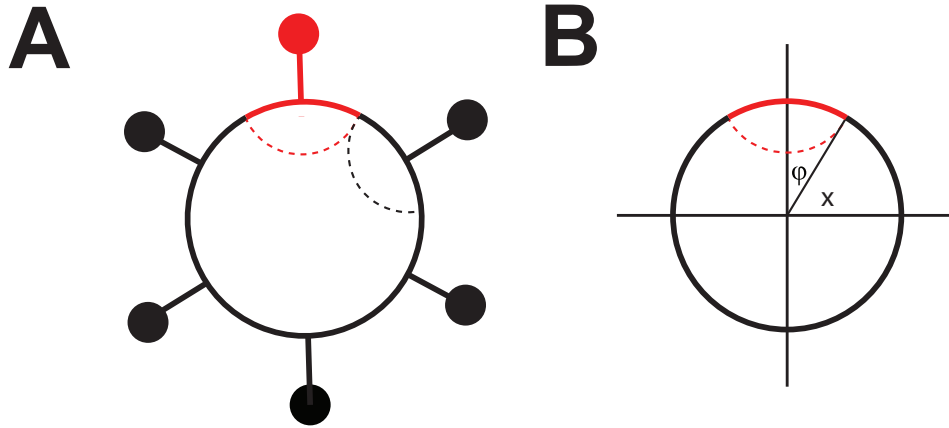


Figure 4-14: Schematics of the estimation of distance between adjacent pMHCs on a NP. Panel **A**) visualizes the fraction of the NP surface associated with each pMHC as a spherical cap and panel **B**) shows that spherical cap as defined on a Cartesian axis.

The plot of $pMHC_{max}$ as a function of v (Fig. 4-13C and Fig. 4-13D) shows that a the number of pMHCs in a cluster at an optimal k_{on} is attained at a local maximum given by ~ 1500 pMHCs/cluster. This result was identical for both NP sizes assessed.

We can estimate the distance between two adjacent pMHCs on a NP assuming NPs to be spheres with radius r , having a total surface area of $4\pi r^2$. Thus for a NP coated with v pMHCs, the surface area associated with to each pMHC is:

$$\frac{4\pi r^2}{v}. \quad (4.48)$$

We approximate the region of NP of associated with each pMHC by spherical cap (see Fig. 4-14) whose surface area is given by:

$$\begin{aligned} \frac{4\pi r^2}{v} &= 2\pi r^2 \int_x^{\pi/2} \cos \theta d\theta = 2\pi r^2 - 2\pi r^2 \sin x \implies \\ \sin x &= (1 - 2/v) \implies \\ x &= \arcsin \left(1 - \frac{2}{v} \right). \end{aligned} \quad (4.49)$$

where the angle subtended by the spherical cap φ is $\pi/2 - x$, i.e. :

$$\varphi = \pi/2 - \arcsin \left(1 - \frac{2}{v} \right) = \arccos \left(1 - \frac{2}{v} \right). \quad (4.50)$$

Assuming that each pMHC sits at the center of this spherical cap subtended by φ , and that two pMHC occupy roughly the same sized region, then the distance d along the great circle that links the two pMHCs is given by:

$$d = r\varphi = 2r \arccos(1 - 2/v). \quad (4.51)$$

Then maximum the number of pMHCs/cluster is attained when the NP valency is between 20 - 30 pMHC/NP (in fact, 18 pMHC/NP for the smaller 14 nm radius NP and 29 pMHC/NP for the larger 20 nm radius NP). At these valencies and sizes, the distance between two pMHCs on each NPs is estimated to be:

$$2(14) \arccos(1 - 2/(18)) = 13.3247 \text{ nm} \quad (4.52)$$

NP size	max pMHC/cluster	valency	pMHC distance
14 nm	1526 pMHC/cluster	18 pMHC/NP	13.3247 nm
20 nm	1530 pMHC/cluster	29 pMHC/NP	14.9424 nm

Table 4–5: The maximum number of pMHC/cluster that can be attained when k_{on} is optimal along with the valency per NP that can achieve this maximum and the distance between pMHCs at that valency.

for smaller NPs ($r = 14$ and $v = 18$), and

$$2(20) \arccos(1 - 2/(29)) = 14.9424 \text{ nm}, \quad (4.53)$$

for larger NPs ($r = 20$ and $v = 29$), which is remarkably consistent between the two different NP sizes. These results involving $pMHC_{max}$ are summarized in Table 4–5.

4.5.2 NP dissociation rate

The model in Fig. 4–12 is valid for any transition $X_i \rightarrow X_{i+1}$ defined by the Markov model (Fig. 4–1), including the very first transition $X_0 \rightarrow X_1$. By solving this Markov model for a very short period of time dt at the start of the experiment (where dt is short enough, it does not allow T-cells to accumulate beyond X_1), we can limit ourselves to the first transition $X_0 \rightarrow X_1$ only. Numerically speaking, this means that dt is short enough that $X_2(dt)/X_1(dt) \ll 1$ and $A_i(dt) \sim 0$. The model describing the single NP binding within that specific transition (as described by

Fig. 4-12) is given by:

$$\frac{dX^0}{dt} = k_{off}X^1 - mk_{on}NX^0 \quad (4.54)$$

$$\frac{dX^j}{dt} = (m - j + 1)k_{on}NX^{j-1} + (j + 1)k_{off}X^{j+1} - (jk_{off} + (m - j)k_{on}N)X^j \quad (4.55)$$

$$\frac{dX^m}{dt} = k_{on}NX^{m-1} - mk_{off}X^m, \quad (4.56)$$

where $X^j = X_0^j$ for $j = 0, \dots, m$, and $X^m = X_0^m = X_1 (= X_1^0)$. Solving for steady state solution of this system, we obtain:

$$X^j = \left(\frac{m - j + 1}{j} \right) \left(\frac{k_{on}N}{k_{off}} \right) X^{j-1}, \quad (4.57)$$

which is a recursive relationship. Solving for X^m in terms of X^0 , we obtain:

$$X^m = \left(\frac{1 \cdot 2 \cdot 3 \dots m}{m(m-1)(m-2) \dots 1} \right) \left(\frac{k_{on}N}{k_{off}} \right)^m X^0 = \left(\frac{k_{on}N}{k_{off}} \right)^m X^0. \quad (4.58)$$

Since $X_0(dt) = X^0(dt)$ and $X_1(dt) = X^m(dt)$, we can solve for k_{off} as follows:

$$k_{off} = \left[\frac{k_{on}N(dt)X_0(dt)}{X_1(dt)} \right]^{1/m}. \quad (4.59)$$

Setting $dt = 0.3$ s was sufficiently short for the conditions $X_2(dt)/X_1(dt) \ll 1$ and $A_i(dt) \sim 0$ to be satisfied and sufficiently long for the system described by Eqs. (4.54) – (4.56) to reach steady state. Fig. 4-15A shows the values of k_{off} for each NP-size at every valency using Eq. (4.59) and the value of k_{on} used to calculate k_{off} in Fig. 4-15A (shown in Fig. 4-15B). The dissociation constant of NP-binding $K_D = k_{off}/k_{on}$ is also shown in Fig. 4-15C. Values used for these plots are given in Table 4-6. These results indicate that at smaller valencies

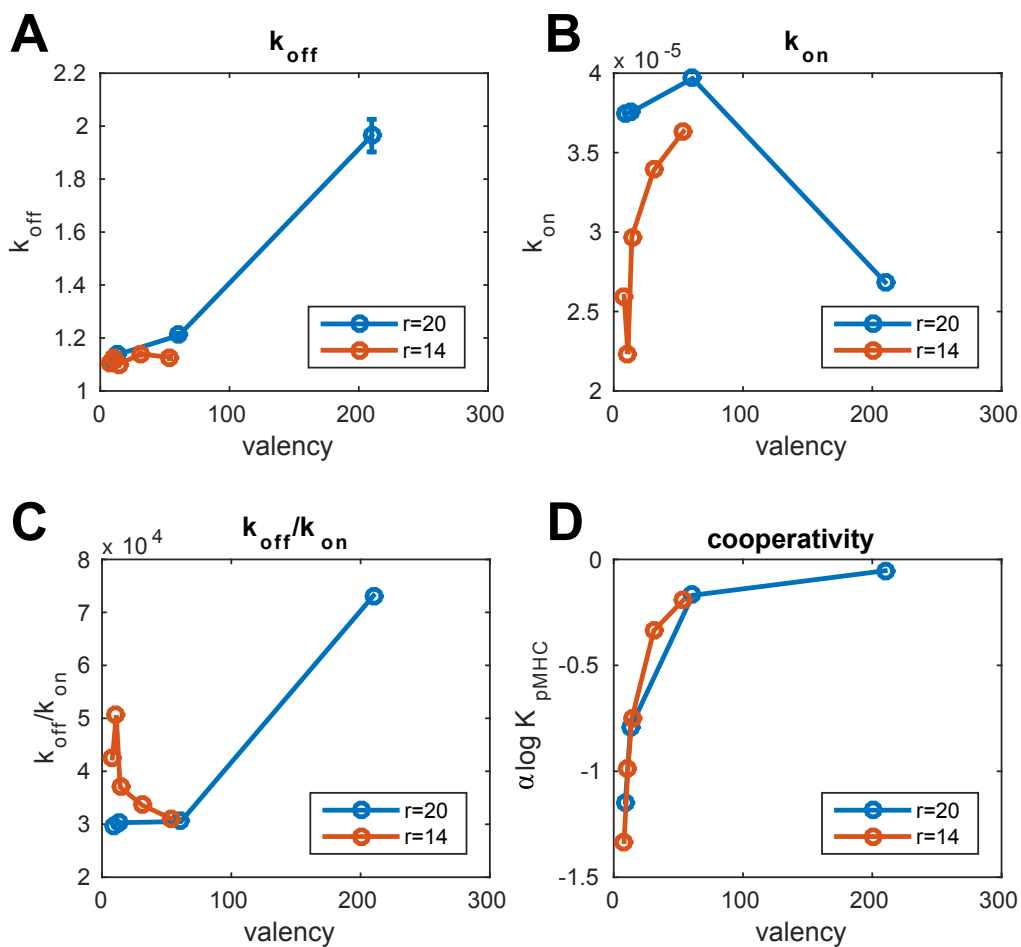


Figure 4-15: The k_{on} and k_{off} rates of NP binding. The NP **A)** unbinding rate k_{off} as given by Eq. (4.59), and **B)** binding rate k_{on} used to calculate k_{off} according to Eq. (4.59) for each NP-size and valency. **C)** Dissociation constant $K_D = k_{off}/k_{on}$ of NP-binding for each NP-size and valency. **D)** Change in cooperativity as NP size and valency are varied according to Eq. (4.61).

NP radius	valency (pMHC/NP)	k_{off}	k_{on}	$K_D = k_{off}/k_{on}$
20 nm	210	1.96	2.68×10^{-5}	7.32×10^4
	61	1.21	3.97×10^{-5}	3.05×10^4
	13	1.14	3.75×10^{-5}	3.03×10^4
	9	1.11	3.75×10^{-5}	2.97×10^4
14 nm	54	1.13	3.63×10^{-5}	3.10×10^4
	31	1.14	3.39×10^{-5}	3.36×10^4
	14	1.10	2.97×10^{-5}	3.70×10^4
	11	1.13	2.23×10^{-5}	5.05×10^4
	8	1.10	2.60×10^{-5}	4.25×10^4

Table 4–6: NP binding (k_{on}), unbinding (k_{off}) and dissociation rate (K_D) parameter values.

($v < 60$), larger NPs bind longer to T-cells and thus more effective, whereas at larger valencies ($v > 60$), smaller NPs bind longer and are more effective.

4.6 Co-operativity

Mammen et al. [34] used the notion of Gibb’s free energy to derive a relation between the association constant of a polyvalent ligand binding to its monovalent counterpart. This relation is given by:

$$K_N^{poly} = (K_{avg}^{poly})^N = (K^{mono})^{\alpha N}, \quad (4.60)$$

where K_N^{poly} represents the association constant of the polyvalent ligand having N ligands, K_{avg}^{poly} represents the association constant of each ligand in the polyvalent system, K_{mono} represents the association constant of a monovalent ligand, and α is a measure of co-operativity of binding conferred by polyvalency. One can apply the theory to NP-binding by treating pMHC-NPs binding to TCRs as a polyvalent version of the monovalent pMHC-TCR interaction. This is achieved

by interpreting K_N^{poly} as the association constant of NP-binding given by $K_A = k_{on}/k_{off}$, where k_{on} is given by Eq. (4.37) and k_{off} is given by Eq. (4.59), and K^{mono} as the association constant for each pMHC-TCR binding (K_{pMHC}), a quantity that is unknown. Our interest in Mammen et al.'s work is in the co-operativity constant of polyvalent (NP) binding. In the case of NP-binding, the relationship described by Eq. (4.60) can be interpreted as:

$$\begin{aligned} (K^{mono})^{\alpha N} &\equiv (K_{pMHC})^{\alpha v} = K_A = \frac{k_{on}}{k_{off}} \equiv K_N^{poly} \implies \\ (K_{pMHC})^\alpha &= K_A^{1/v} \implies \\ \alpha \log(K_{pMHC}) &= \frac{\log K_A}{v}, \end{aligned} \quad (4.61)$$

where v is the NP valency. On the left hand side, both the co-operativity α and K_{pMHC} are unknown, which makes it impossible to solve for α . However, since the pMHCs used in the experimental conditions presented in this thesis are identical, we can safely assume K_{pMHC} is a constant in this system. This means that

$$\frac{\log K_A}{v} \propto \alpha, \quad (4.62)$$

and changes in co-operativity due to the effect of valency would be evident from changes in $\frac{\log K_A}{v}$.

The plot of $\frac{\log K_A}{v}$ (Fig. 4-15D) shows that co-operativity α is increasing with respect to the valency v . However, this increase reaches a plateau at approximately 60 pMHC/NP, meaning that further increases in valency beyond 60 pMHC/NP will lead to no further increases in co-operativity. This characteristic in

co-operativity seems to be the case for both large (20 nm radius) and small (14 nm radius) NPs.

4.7 Other models

We considered a slight variation of the model of nanocluster binding (Fig. 4-1) by changing the swallowing rate of the NPs to reflect the possibility that the T-cells can internalize multiple NP-clusters at a time shown in Fig. 4-16.

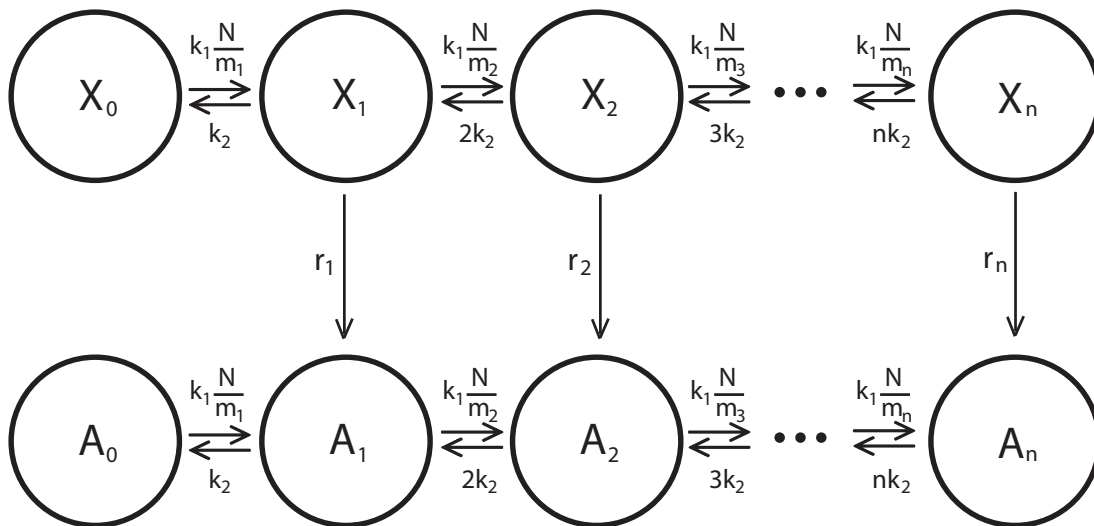


Figure 4-16: Markov model of nanocluster unsaturated binding and swallowing.

Implementing MCMC methods to estimate the parameters of this model (in a manner similar to what was done in Section 4.2), revealed that this model is also able to produce reasonable fits to the $\text{IFN}\gamma$ production data as shown in Fig. 1-4 (compare to Fig. 4-17).

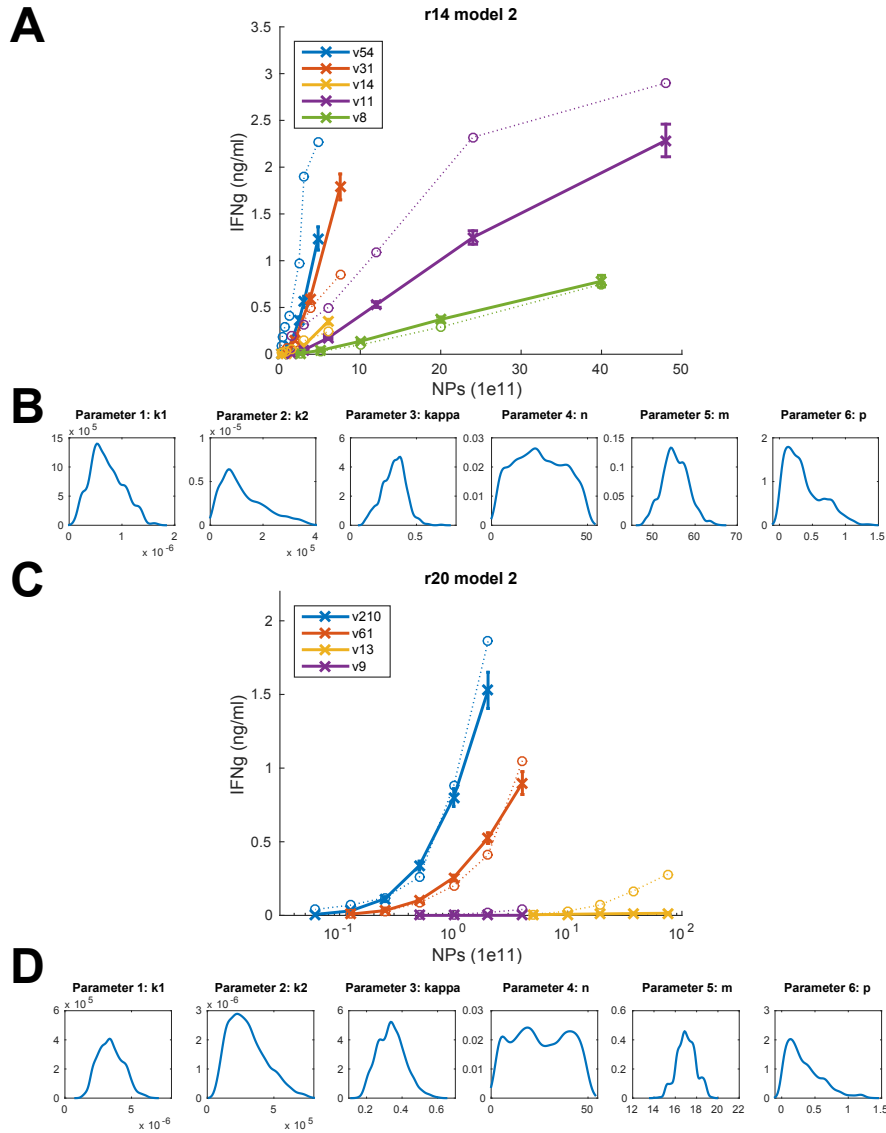


Figure 4-17: Fitting the INF γ data of Fig. 1-4 to model simulations. INF γ production by T-cells stimulated with pMHC-NPs with radius **A**), **B**) 14 nm and **C**), **D**) 20 nm coated with various valencies were fitted to the model depicted by Fig. 4-16, where **B**) and **D**) show the distributions of estimated parameters according to their respective NP-size. Panels **A**) and **C**) show mean and standard deviation of model predictions using 100 random draws from the parameter distributions depicted in **B**) and **D**), respectively.

4.7.1 Model selection

To objectively assess whether the unsaturated digestion model is better or worse than serial digestion model in describing the physiological data, we employ two common measures for model selection called the Akaike Information Criteria (AIC) and Bayesian Information Criteria (BIC). Both measures assess goodness of fit that favours smaller residual error in the model, but penalise for adding complexity (i.e. parameters) to avoid overfitting. The latter, however, adds more weight to the high-dimensionality penalty. These model selection measures are calculated using the expressions:

$$AIC = n \log(SSE) - n \log(n) + 2P \quad (4.63)$$

and

$$BIC = n \log(SSE) - n \log(n) + \log(n)P, \quad (4.64)$$

where P is the number of parameters in the system, n is the number of data points available and SSE is the sum-of-square residual error. The model that produces the lowest AIC/BIC values is considered to be the better model. A p -value given by:

$$p = \exp\left(\frac{AIC_{min} - AIC_i}{2}\right), \quad (4.65)$$

where AIC_{min} is the minimum AIC of all models and AIC_i is the AIC of the i -th model, can be calculated from the AIC test (or BIC test) to determine whether the two models differ significantly from each other. Typically, a value of $p \leq 0.05$ is used to determine whether one model is significantly better than another, which is obtained when $AIC_{min} - AIC_i \leq -6$.

	Serial Digestion		Unsaturated Digestion		<i>p</i> -values	
	AIC	BIC	AIC	BIC	AIC	BIC
14 nm	163.6 (1.57)	170.2 (1.57)	164.4 (0.28)	172.4 (0.28)	0.6656	0.3419
20 nm	117.0 (3.38)	122.2 (3.38)	119.0 (0.35)	125.3 (0.35)	0.3572	0.2119
all	150.5 (1.25)	155.7 (1.25)	151.8 (0.20)	158.1 (0.20)	0.5058	0.3000

Table 4–7: Comparison of model selection criteria AIC and BIC applied to serial digestion model and unsaturated digestion.

We applied these measures to compare the serial and unsaturated digestion models by calculating the *SSE* using Eq. (4.18) and evaluating the error of fit using 100 randomly selected parameters, followed by reporting the average and standard deviation of AIC and BIC in Table 4–7. The results consistently showed that the serial digestion model is numerically better than the unsaturated digestion model by both AIC and BIC tests, but the *p*-values were not significantly different between the two models. A likely explanation for this is that there may be a mix of both types of digestion taking place within the system.

CHAPTER 5

Conclusion and Discussion

This thesis has focused on developing models to understand the interaction between T-cells and nanoparticles coated with peptide-MHC, the cognate ligand of TCRs. The use of pMHC-NPs in experimental treatment of T1D in NOD mice showed very promising results in blunting the autoimmune response against pancreatic β -cells [59]. Spurred by its potential as a therapeutic agent, our mathematical models were developed with the goal of guiding pMHC-NP design to optimize the efficacy of treatment.

In animal models, pMHC-NPs reverse T1D symptoms through the activation and expansion of a subset of autoregulatory T-cells that suppress the autoimmune response. The activation and replication of T-cells is a complicated process that involves the organized interaction of many molecular players besides the TCR, such as co-stimulatory molecules CD28, structural molecules CD8 and CD4, and signaling molecules such as CD3 as well as the formation of a supramolecular adhesion complex (also known as an immune synapse). Additionally, heterogeneity is a factor in all measures of biological responses, including the data presented here (Fig. 1-2, 1-4).

The method of MCMC was discussed in Chapter 2 to account for heterogeneity in T-cell responses. Estimating a distribution of parameters provides a better description of biological variations within the system which can be incorporated

into mathematical approaches to predict the range of responses. The model of T-cell expansion *in vivo* developed in Chapter 3 showed consistently that smaller NPs, (i.e. smaller in diameter), were capable of inducing greater expansion of T-cell population, even when coated at lower valencies. In Chapter 4, we presented a more complicated, Markov Model to better understand the biophysical parameters that govern the pMHC-NP interaction. In particular, we broke down these interactions to three levels: (i) nanocluster binding to T-cells, (ii) NP binding within a nanocluster, and (iii) single pMHCs on multivalent NPs binding to TCRs. At the nanocluster level, analysis of joint distribution of the binding rate of nanoclusters k_1 and the size of these clusters m led us to conclude that k_1 can be mathematically determined using m and the valency of NPs. Zooming in to individual NPs interacting with TCRs revealed that there is a unique, optimal NP binding rate corresponding to a unique combination of cluster size and valency for each NP-size. At the single pMHC-TCR interaction level, we were able to describe the effects of coating single NPs with multiple pMHCs on co-operativity of binding.

In addition to thoroughly investigating the biophysical and kinetic parameters of pMHC-NP interactions with T-cells, this work presents a framework to analysing complex nano-scale interactions from a top-down hierarchical approach. Activation and proliferation of T-cells through treatment of NPs conjugated to multiple pMHCs presents a very unique and new approach to examining pMHC-TCR binding. The structural design (density) of pMHC-NP and the size of contact region of NPs for binding would not play a role in soluble or even tetrameric pMHC binding. Studies using pMHCs on stabilized monolayers allows control of

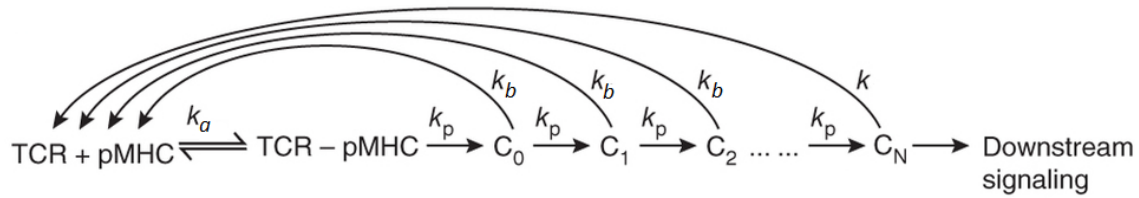


Figure 5–1: Kinetic proof reading model of T-cell activation.

the distance between pMHC molecules which can be accomplished using pMHC-NPs [21] however spherical construction of the NPs presents a different topology which merits separate investigations. Compared to pMHCs were presented on APCs, which are many times larger than T-cells, the use of pMHC-NPs can create a more controlled environment in terms of the number of pMHCs and pMHC density. One further important way in which T-cell activation through pMHC-NP stimulation differ from natural APC-mediated activation is the lack of co-stimulatory molecules. We can theorize T-cells binding to pMHC-NPs without the presence of costimulation to be akin to T-cells naturally binding to resting APCs, which express co-stimulatory molecules at lower levels than activated APCs. Resting B-cells acting as APCs have demonstrated effects in inducing tolerance in naïve T-cells [17] and we can postulate the same tolerogenic pathways may be activated when stimulated with pMHC-NPs. Future work from this thesis should focus on providing better understanding of T-cell activation kinetics.

5.1 Future Considerations

5.1.1 Kinetic proof reading as a model of T-cell activation

The model we chose for the activation kinetics is very simplistic. Biologically, activation is very complex and known to be regulated by a number of protein

modification steps [26, 49]. Experiments using panels of different TCRs and pMHC complexes have reported various relationships between the TCR-pMHC binding parameters and T-cell activation, as measured by downstream functional readouts such as cytokine secretion [15, 19, 20, 29]. These observations have, in part, motivated the formulation of a variety of models to reproduce the observed T-cell activation phenotypes [33]. A prevailing model is the kinetic proof reading model, which proposes that T-cell activation is proportional to the fraction of pMHC-TCRs that have been bound for long enough to achieve a competent signaling state (Fig. 5–1).

The kinetic proof reading model, shown in Fig. 5–1, is an alternative approach to describing T-cell activation. It is described by the following equations:

$$\frac{dP}{dt} = -k_a PT + k_b \sum_{i=0}^N C_i \quad (5.1)$$

$$\frac{dT}{dt} = -k_a PT + k_b \sum_{i=0}^N C_i \quad (5.2)$$

$$\frac{dC_0}{dt} = k_a PT - (k_b + k_p)C_0 \quad (5.3)$$

$$\frac{dC_i}{dt} = k_p C_{i-1} - (k_a + k_p)C_i \quad i = 1, \dots, N - 1 \quad (5.4)$$

$$\frac{dC_N}{dt} = k_p C_{N-1} - k_a C_N, \quad (5.5)$$

where P is the number of free pMHCs, T is the number of free TCRs, which bind to form the complex C_0 . Each biochemical modifications step of the complex proceed with rate k_p and the number of complexes with i chemical modification, is given by C_i . Competent signaling state is achieved only after N modifications, i.e. only complexes in the C_N state yield productive signal. These modification steps

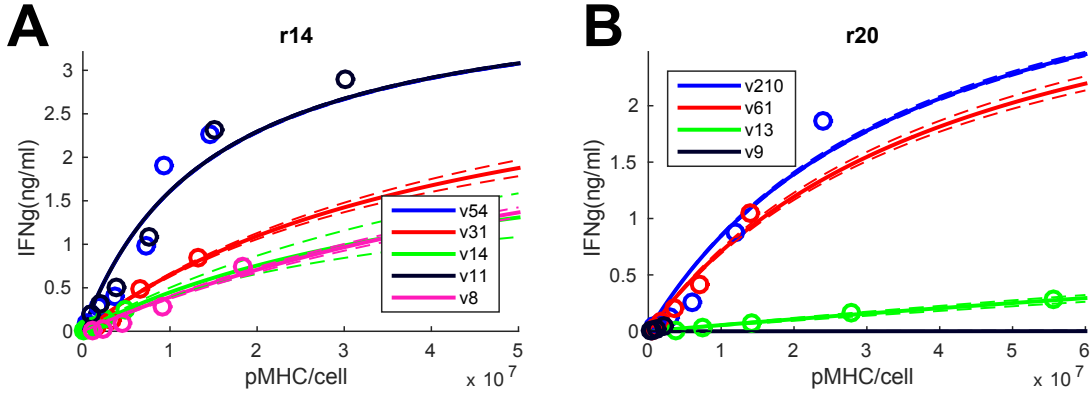


Figure 5-2: Fitting Hill functions with Hill coefficient $n = 1$ to *in vitro* stimulation data of T-cells using **A)** 14 nm radius NPs and **B)** 20 nm radius NPs .

that transition C_0 to C_N are stopped immediately upon pMHC unbinding. In this model, the binding rate of the pMHC to TCR is given by k_a , and the unbinding rate by k_b .

Solving this system at steady state, we find that the total number of pMHC-TCR complexes $C_T = \sum_{i=0}^N C_i$ is related to the number of productive signaling complexes by $C_T = \frac{1}{\lambda^N} C_N$, where $\lambda = \frac{k_p}{k_p + k_b}$. In other words:

$$C_N = \lambda^N C_T \quad (5.6)$$

If we let P_T and T_T denote the total number of pMHCs and TCRs, respectively, it follows that:

$$P_T = P + C_T \quad (5.7)$$

$$T_T = T + C_T. \quad (5.8)$$

Solving for the steady state of Eq. (5.1), we obtain:

$$\begin{aligned}
k_b C_T &= k_a P T = k_a P (T_T - C_T) \implies \\
(k_b + k_a P) C_T &= k_a P T_T \implies \\
C_T &= \frac{k_a P T_T}{k_b + k_a P} = \frac{P T_T}{k_D + P}, \tag{5.9}
\end{aligned}$$

where $k_D = k_b/k_a$ represents the dissociation constant of pMHC-binding (as opposed to K_D from Chapter 4 which represents the dissociation constant of NP-binding). Since C_T is the number of pMHC-TCR complexes, we may conclude that $C_T \leq \min(P_T, T_T)$. As $P_T \rightarrow \infty$, (i.e. $P \rightarrow \infty$) we have:

$$\lim_{P_T \rightarrow \infty} C_T = T_T, \tag{5.10}$$

which represents the E_{max} of the system. To obtain the EC_{50} of the dose response curve, on the other hand, we have to set $C_T = T_T/2$. In this case, $P = k_D$. From Eq. (5.7), we have:

$$\begin{aligned}
P &= P_T - C_T = P_T - T_T/2 \implies \\
P_T &= P + T_T/2 = k_D + T_T/2 \tag{5.11}
\end{aligned}$$

Based on fittings of Hill-functions, with Hill coefficient of $n=1$, to the INF γ data obtained from following *in vitro* T-cell stimulation experiments (Fig. 5-2), the estimated EC_{50} (Table 5-1) obtained were in the order of 10^7 molecules/cell or higher. Since there is on average $8 - 10 \times 10^4$ TCRs per T-cell (T_T) [55], we conclude from the kinetic proof reading formalism that k_D , which is the dissociation constant at the level of pMHC binding, is $\sim 10^7$ molecules. Recall

NP radius	valency (pMHC/NP)	E_{max}	EC_{20}
20 nm	210	3.97	3.68×10^7
	61	3.82	4.37×10^7
	13	2.75	5.01×10^8
	9	2.02	2.48×10^{11}
14 nm	54	3.99	1.48×10^7
	31	3.61	4.58×10^7
	14	2.71	5.03×10^7
	11	3.99	1.48×10^7
	8	3.63	8.28×10^7

Table 5–1: Estimates of E_{max} and EC_{50} based on kinetic proof reading model.

from Chapter 4 that the dissociation constant K_D at the NP-binding level is $\sim 10^4$ (Table 4–6). Mammen et al. [34] provides a way to relate the association constant of polyvalent NP binding ($K_A = 1/K_D$) to monovalent pMHC binding given by $k_A = 1/k_D$, unlike the kinetic proof reading model which cannot explain the observation that the monovalent k_D is different for each valency (Table 5–1).

5.1.2 Probability of activation

In our models (Fig. 4–1 and 4–16), we defined the rate of transition from an unactivated state to an activated state r_i in Eq. (4.9) as

$$r_i = \kappa P_i F(m, v) = \kappa \cdot \frac{i}{p+i} \cdot \frac{(m\hat{v})^2}{a^2 + (m\hat{v})^2}.$$

Based on MCMC fittings, we found that the mode of $p \ll 1$ (see Table 4–1), making the probability that each state transitions to the activated state $P_i = \frac{i}{p+i} \approx 1$ for $i \geq 1$. This implies that T-cell activation is induced by the binding of very few clusters, which appears to be not in agreement with the imaging data shown in Fig. 1–3. One potential explanation for this discrepancy

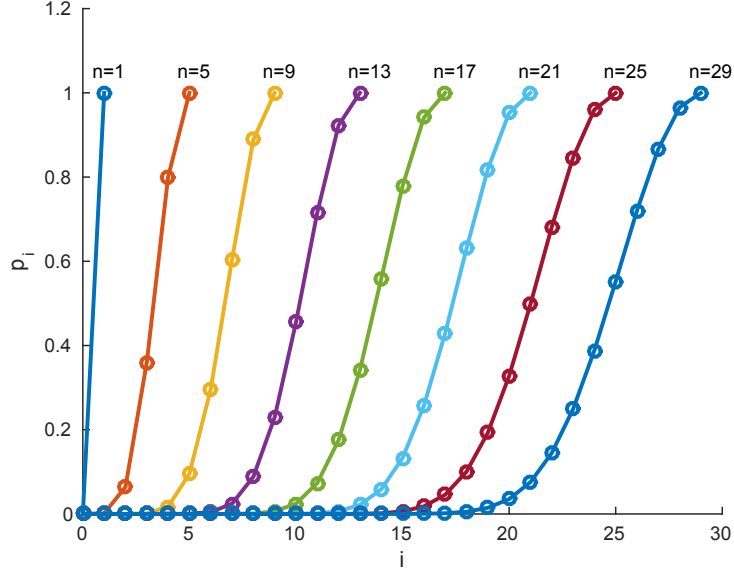


Figure 5-3: Behaviour of P_i based on Eq. (5.12).

between simulation and data is that T-cells do not require the binding of too many NP-clusters to activate. Another explanation could be that the functional choice made for P_i is not accurate.

In future work, we intend to try other expressions to describe the probability of transitions. One such candidate is:

$$P_i = \left(\frac{i}{n} \right)^{n-i}. \quad (5.12)$$

As shown in Fig. 5-3, this function has the characteristics of a steep Hill function, but with transition probabilities that are small for small i (the number of clusters bound to T-cells). Testing such a function will allow us to determine if large number of cluster binding is necessary for T-activation.

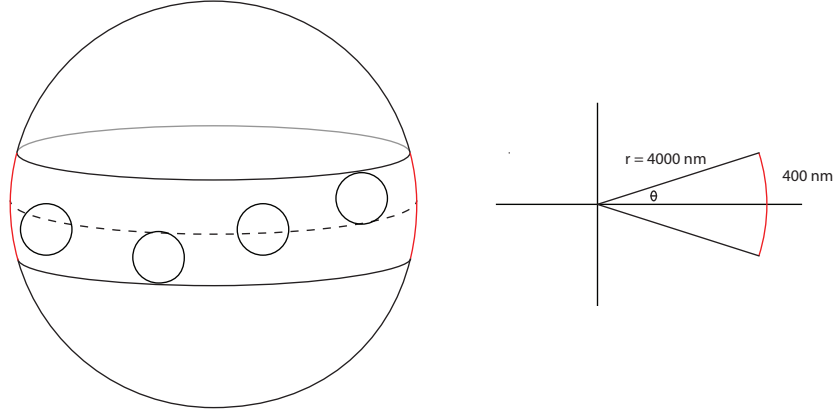


Figure 5-4: Schematics of the NP-cluster binding to the membrane of T-cells as visualized by an EM image.

5.1.3 Estimation of number of nanoclusters

The EM image of nanoclusters bound to T-cells (Fig. 1-3) provides insights onto how to estimate the total number of nanoclusters that bind to the surface of a T-cell. By assuming that each T-cell is roughly a sphere with a radius of $4 \mu\text{m}$ [35] and each image slice of the cell is a slice through the center of the sphere, we can estimate the total number of nanoclusters. Since each image shows 4 – 5 nanoclusters bound, with each nanocluster being maximally 400 nm in diameter, we can postulate that the imaging data provides a sample of the number of nanoclusters that are bound through a band on the surface of the T-cell (see Fig. 5-4). The surface area occupied by this band is give by:

$$SA_{band} = \int_0^{2\pi} \int_{-1/10}^{1/10} 4 \cos \varphi \cdot 4d\varphi d\theta = 64\pi \sin(1/10), \quad (5.13)$$

where $1/10$ is the angle in radian subtended by the band.

The area occupied by the band, SA_{band} , is roughly 1/10 of the area of the sphere representing the T-cell ($SA_{cell} = 4\pi r^2 = 64\pi$). Since 4 – 5 nanoclusters are observed in 1/10 of the surface of the T-cell, we should then expect 40 – 50 nanoclusters to be bound to the entire cell, which is far greater than obtained from the mode of the parameter estimation using MCMC fitting. By imposing this number of nanoclusters on model fitting, we should expect that the total number of parameters required for estimation to decrease but the major results obtained in Chapter 4 to remain roughly the same.

APPENDIX A
IFN γ production data

Valency (pMHC/NP)	Dose ($\times 10^{11}$ NP/ml)	IFN γ (ng/ml)
210	0.061	0.04
210	0.125	0.07
210	0.25	0.12
210	0.5	0.26
210	1	0.88
210	2	1.86
61	0.125	0.01
61	0.25	0.03
61	0.5	0.085
61	1	0.2
61	2	0.41
61	4	1.05
13	5	0.004
13	10	0.03
13	19	0.07
13	37.5	0.166
13	75	0.279
9	0.5	0.001
9	1	0.005
9	2	0.02
9	4	0.04

Table A-1: IFN γ produced by 2.5×10^5 T-cells/ml incubated *in vitro* with 20 nm radius NPs of various valency and dose for 48 hours corresponding to Fig. 1-4.

Valency (pMHC/NP)	Dose ($\times 10^{11}$ NP/ml)	IFN γ (ng/ml)
54	0.15	0.09
54	0.3	0.19
54	0.6	0.29
54	1.2	0.41
54	2.375	0.976
54	3	1.9
54	4.75	2.27
31	0.94	0.06
31	1.875	0.13
31	3.75	0.49
31	7.5	0.85
14	0.19	0.015
14	0.375	0.021
14	0.75	0.025
14	1.5	0.055
14	3	0.143
14	6	0.241
11	1.5	0.2
11	3	0.31
11	6	0.5
11	12	1.09
11	24	2.32
11	48	2.9
8	2.5	0.01
8	5	0.03
8	10	0.1
8	20	0.29
8	40	0.75

Table A-2: IFN γ produced by 2.5×10^5 T-cells/ml incubated *in vitro* with 14 nm radius NPs of various valency and dose for 48 hours corresponding to Fig. 1-4.

APPENDIX B Code

B.1 Running MCMC Toolbox

```
function [res,chain,sschain] = mcmc_run_serial(r,nsim, init, filename, rows)
    data = get_ifndata(r, rows);
    options.nsimu = nsim;
    model.ssfun = @ifn_err_ode15s;
    params = {{ 'k1', init(1), 1e-15, 1},{ 'k2',init(2), 5, 10e6 } ,...
    { 'kappa', init(3),0.1,.7,.2,.1}, { 'n', init(4), 2, 80}...
    { 'm', init(5), 3, 300}, { 'p', init(6), 0, 100}};
    [res,chain,s2chain,sschain] = mcmcrun(model,data,params,options);
    save (sprintf('data/r%.0f_serial_%s',r,filename),'chain','res','sschain')
end
```

B.2 Sum-of-square error function

```
function [ err ] = ifn_err_ode15s(par,data)
    err = 0; x0=2.5; T=48; sim = zeros (length(data),2);

    %% arg parsing
    global k1 k2 m
    k1 = par(1); k2 = par(2); kappa = par(3); n_state = floor(par(4));
    m = zeros (n_state,2); m (2:end,:) = floor(par(5)); p = par(6);
    opts=odeset('RelTol',1e-6,'AbsTol',1e-12,'InitialStep',0.0001,'MaxStep',0.5);
```

```

for i = 1:length(data(:,1))
    d = data(i,:); sim (i,1)=d(3); v=d(1)/7.0; a=130;
    %% calculating activation rate
    fi = (v*m(:,1)).^2./(a^2 + (v * m(:,1)).^2);
    f = kappa * ([0:n_state-1]./(p+[0:n_state-1])).'* fi ;
    %% ODE solve
    u0 = zeros (3*n_state,1); u0(1) = d(2)*1e11; u0(n_state+1) = x0;
    sol15 = ode15s(@fun_ode, [0,T], u0,opts,f);
    sim(i,2) = 4.47e-13*(1e5*sum(sol15.y(2*n_state+1:end,end)))^(2.5);
end

    %% error calculation
    err = sum (((data(:,3)-sim(:,2))./(atan(data(:,3))/2)).^2) * 100;
    err = err/(length(data));
end

```

B.3 DE model

```

function [du] = fun_ode(t,u,f)
    global m k1 k2
    n_state = size (u,1)/3; states = [1:(n_state)].';
    X = u(n_state+1:2*n_state); A = u(2*n_state+1:end); Nf = u(1,1);
    dNf = - k1 * 1e5* Nf * (sum (X(1:end-1).*states (1:end-1)) + ...
        sum(A(1:end-1).*states (1:end-1)));
    dX0 = - k1 * Nf / m(2,1)* X(1) + k2 * X(2);
    dXi = -k1 * Nf * X(2:end-1) ./ m(3:end,1) ...
        + k1 * Nf * X(1:end-2) ./ m(2:end-1,1)...

```

```

        - k2 * X(2:end-1) + k2 * X(3:end)...
        - f (2:end-1).* X(2:end-1);
dXn = k1 * Nf * X(end-1) / m(end,1) ...
        - k2 * X(end) - f (end) * X(end);

dA0 = - k1 * Nf / m(2,2)* A(1) + k2 * A(2);
dAi = -k1 * Nf * A(2:end-1) ./ m(3:end,2)...
        + k1 * Nf * A(1:end-2) ./ m(2:end-1,2)...
        - k2 * A(2:end-1) + k2 * A(3:end)...
        + f (2:end-1) .* X(2:end-1);
dAn = k1 * Nf * A(end-1) / m(end,2)...
        - k2 * A(end) + f (end) * X(end);

du = zeros(size(u)); du (1) = dNf; du (n_state+1) = dX0;
du (n_state+2 : 2*n_state-1) = dXi; du (2*n_state) = dXn;
du (2*n_state+1) = dA0; du (2*n_state+2 : 3*n_state-1) = dAi;
du (3*n_state) = dAn;
end

```

References

- [1] Abdelaziz Amrani, Joan Verdaguer, Pau Serra, Sabrina Tafuro, Rusung Tan, and Pere Santamaria. Progression of autoimmune diabetes driven by avidity maturation of a t-cell population. *Nature*, 406(6797):739–742, 2000.
- [2] Stephen M Anderton and David C Wraith. Selection and fine-tuning of the autoimmune t-cell repertoire. *Nature Reviews Immunology*, 2(7):487–498, 2002.
- [3] Mylene Bedard. Optimal acceptance rates for metropolis algorithms: Moving beyond 0.234. *Stochastic Processes and their Applications*, 118(12):2198–2222, 2008.
- [4] Hélène Bour-Jordan and Jeffrey A Bluestone. B cell depletion: a novel therapy for autoimmune diabetes? *The Journal of clinical investigation*, 117(12):3642, 2007.
- [5] Jason Brayer, Fengdong Cheng, Hongwei Wang, Pedro Horna, Ildefonso Vicente-Suarez, Javier Pinilla-Ibarz, and Eduardo M Sotomayor. Enhanced cd8 t cell cross-presentation by macrophages with targeted disruption of stat3. *Immunology letters*, 131(2):126–130, 2010.
- [6] DE Campbell, AS Fryga, S Bol, and AS Kemp. Intracellular interferon-gamma (ifn- γ) production in normal children and children with atopic dermatitis. *Clinical and experimental immunology*, 115:377–382, 1999.
- [7] Emma M Caraher, Monique Parenteau, Heidi Gruber, and Fraser W Scott. Flow cytometric analysis of intracellular ifn- γ , il-4 and il-10 in cd3+ 4+ t-cells from rat spleen. *Journal of immunological methods*, 244(1):29–40, 2000.
- [8] Xavier Clemente-Casares and Pere Santamaria. Nanomedicine in autoimmunity. *Immunology letters*, 158(1):167–174, 2014.

- [9] Xavier Clemente-Casares, Sue Tsai, Carol Huang, and Pere Santamaria. Antigen-specific therapeutic approaches in type 1 diabetes. *Cold Spring Harbor perspectives in medicine*, 2(2):a007773, 2012.
- [10] Xavier Clemente-Casares, Sue Tsai, Yang Yang, and Pere Santamaria. Peptide-mhc-based nanovaccines for the treatment of autoimmunity: a one size fits all approach? *Journal of molecular medicine*, 89(8):733–742, 2011.
- [11] Miriam Cnop, Nils Welsh, Jean-Christophe Jonas, Anne Jörns, Sigurd Lenzen, and Decio L Eizirik. Mechanisms of pancreatic β -cell death in type 1 and type 2 diabetes many differences, few similarities. *Diabetes*, 54(suppl 2):S97–S107, 2005.
- [12] Denis Daneman. Type 1 diabetes. *The Lancet*, 367(9513):847–858, 2006.
- [13] Rob J De Boer, Mihaela Oprea, Rustom Antia, Kaja Murali-Krishna, Rafi Ahmed, and Alan S Perelson. Recruitment times, proliferation, and apoptosis rates during the cd8+ t-cell response to lymphocytic choriomeningitis virus. *Journal of virology*, 75(22):10663–10669, 2001.
- [14] Rob J De Boer and Alan S Perelson. T cell repertoires and competitive exclusion. *Journal of theoretical biology*, 169(4):375–390, 1994.
- [15] Omer Dushek, Milos Aleksic, Richard J Wheeler, Hao Zhang, Shaun-Paul Cordoba, Yan-Chun Peng, Ji-Li Chen, Vincenzo Cerundolo, Tao Dong, Daniel Coombs, et al. Antigen potency and maximal efficacy reveal a mechanism of efficient t cell activation. *Science signaling*, 4(176):ra39, 2011.
- [16] GS Eisenbarth. Type i diabetes mellitus. a chronic autoimmune disease. *The New England journal of medicine*, 314(21):1360, 1986.
- [17] Dean E Evans, Michael W Munks, Jeffrey M Purkerson, and David C Parker. Resting b lymphocytes as apc for naive t lymphocytes: dependence on cd40 ligand/cd40. *The Journal of Immunology*, 164(2):688–697, 2000.
- [18] Diane T Finegood, Luisa Scaglia, and Susan Bonner-Weir. Dynamics of β -cell mass in the growing rat pancreas: estimation with a simple mathematical model. *Diabetes*, 44(3):249–256, 1995.
- [19] Pablo A González, Leandro J Carreño, Daniel Coombs, Jorge E Mora, Edith Palmieri, Byron Goldstein, Stanley G Nathenson, and Alexis M Kalergis. T cell receptor binding kinetics required for t cell activation depend on the

- density of cognate ligand on the antigen-presenting cell. *Proceedings of the National Academy of Sciences of the United States of America*, 102(13):4824–4829, 2005.
- [20] Christopher C Govern, Michelle K Paczosa, Arup K Chakraborty, and Eric S Huseby. Fast on-rates allow short dwell time ligands to activate t cells. *Proceedings of the National Academy of Sciences*, 107(19):8724–8729, 2010.
- [21] Ryan N Gutenkunst, Daniel Coombs, Toby Starr, Michael L Dustin, and Byron Goldstein. A biophysical model of cell adhesion mediated by immunoadhesin drugs and antibodies. *PloS one*, 6(5), 2011.
- [22] Heikki Haario, Marko Laine, Antonietta Mira, and Eero Saksman. Dram: efficient adaptive mcmc. *Statistics and Computing*, 16(4):339–354, 2006.
- [23] Heikki Haario, Eero Saksman, and Johanna Tamminen. An adaptive metropolis algorithm. *Bernoulli*, pages 223–242, 2001.
- [24] Bingye Han, Pau Serra, Abdelaziz Amrani, Jun Yamanouchi, Athanasius FM Marée, Leah Edelstein-Keshet, and Pere Santamaria. Prevention of diabetes by manipulation of anti-igrp autoimmunity: high efficiency of a low-affinity peptide. *Nature medicine*, 11(6):645–652, 2005.
- [25] W Keith Hastings. Monte carlo sampling methods using markov chains and their applications. *Biometrika*, 57(1):97–109, 1970.
- [26] William F Hawse, Matthew M Champion, Michelle V Joyce, Lance M Hellman, Moushumi Hossain, Veronica Ryan, Brian G Pierce, Zhiping Weng, and Brian M Baker. Cutting edge: evidence for a dynamically driven t cell signaling mechanism. *The Journal of Immunology*, 188(12):5819–5823, 2012.
- [27] Kevan C Herold, William Hagopian, Julie A Auger, Ena Poumian-Ruiz, Lesley Taylor, David Donaldson, Stephen E Gitelman, David M Harlan, Danlin Xu, Robert A Zivin, et al. Anti-cd3 monoclonal antibody in new-onset type 1 diabetes mellitus. *New England Journal of Medicine*, 346(22):1692–1698, 2002.
- [28] Majid Jaber-Douraki, Shang Wan Shalon Liu, Massimo Pietropaolo, and Anmar Khadra. Autoimmune responses in t1dm: quantitative methods to understand onset, progression, and prevention of disease. *Pediatric diabetes*, 15(3):162–174, 2014.

- [29] Alexis M Kalergis, Nicole Boucheron, Marie-Agnés Doucey, Edith Palmieri, Earl C Goyarts, Zsuzsanna Vegh, Immanuel F Luescher, and Stanley G Nathenson. Efficient t cell activation requires an optimal dwell-time of interaction between the tcr and the pmhc complex. *Nature immunology*, 2(3):229–234, 2001.
- [30] Anmar Khadra, Massimo Pietropaolo, Gerald T Nepom, and Arthur Sherman. Investigating the role of t-cell avidity and killing efficacy in relation to type 1 diabetes prediction. *PloS one*, 6(5):e14796, 2011.
- [31] Anmar Khadra, Pere Santamaria, and Leah Edelstein-Keshet. The role of low avidity t cells in the protection against type 1 diabetes: a modeling investigation. *Journal of theoretical biology*, 256(1):126–141, 2009.
- [32] Jeffrey P Krischer, David D Cuthbertson, Liping Yu, Tihamer Orban, Noel Maclaren, Richard Jackson, William E Winter, Desmond A Schatz, Jerry P Palmer, and George S Eisenbarth. Screening strategies for the identification of multiple antibody-positive relatives of individuals with type 1 diabetes. *The Journal of Clinical Endocrinology & Metabolism*, 88(1):103–108, 2003.
- [33] Melissa Lever, Philip K Maini, P Anton van der Merwe, and Omer Dushek. Phenotypic models of t cell activation. *Nature Reviews Immunology*, 14(9):619–629, 2014.
- [34] Mathai Mammen, Seok-Ki Choi, and George M Whitesides. Polyvalent interactions in biological systems: implications for design and use of multi-valent ligands and inhibitors. *Angewandte Chemie International Edition*, 37(20):2754–2794, 1998.
- [35] Boryana N Manz, Bryan L Jackson, Rebecca S Petit, Michael L Dustin, and Jay Groves. T-cell triggering thresholds are modulated by the number of antigen within individual t-cell receptor clusters. *Proceedings of the National Academy of Sciences*, 108(22):9089–9094, 2011.
- [36] Athanasius FM Marée, Mitsuhiro Komba, Cheryl Dyck, Marek Łabecki, Diane T Finegood, and Leah Edelstein-Keshet. Quantifying macrophage defects in type 1 diabetes. *Journal of theoretical biology*, 233(4):533–551, 2005.
- [37] Athanasius FM Maree, Mitsuhiro Komba, Diane T Finegood, and Leah Edelstein-Keshet. A quantitative comparison of rates of phagocytosis and digestion of apoptotic cells by macrophages from normal (balb/c) and

- diabetes-prone (nod) mice. *Journal of Applied Physiology*, 104(1):157–169, 2008.
- [38] Athanasius FM Marée, Pere Santamaria, and Leah Edelstein-Keshet. Modeling competition among autoreactive cd8+ t cells in autoimmune diabetes: implications for antigen-specific therapy. *International immunology*, 18(7):1067–1077, 2006.
- [39] Nicholas Metropolis, Arianna W Rosenbluth, Marshall N Rosenbluth, Augusta H Teller, and Edward Teller. Equation of state calculations by fast computing machines. *The journal of chemical physics*, 21(6):1087–1092, 1953.
- [40] Penelope A Morel, Janice S Dorman, John A Todd, Hugh O McDevitt, and Massimo Trucco. Aspartic acid at position 57 of the hla-dq beta chain protects against type i diabetes: a family study. *Proceedings of the National Academy of Sciences*, 85(21):8111–8115, 1988.
- [41] Sergey Nejentsev, Joanna MM Howson, Neil M Walker, Jeffrey Szeszko, Sarah F Field, Helen E Stevens, Pamela Reynolds, Matthew Hardy, Erna King, Jennifer Masters, et al. Localization of type 1 diabetes susceptibility to the mhc class i genes hla-b and hla-a. *Nature*, 450(7171):887–892, 2007.
- [42] Jørn Nerup, Thomas Mandrup-Poulsen, Jens Mølviq, S Helqvist, L Wogensen, and J Egeberg. Mechanisms of pancreatic beta-cell destruction in type 1 diabetes. *Diabetes care*, 11:16–23, 1987.
- [43] Viveka Öling, Jane Marttila, Jorma Ilonen, William W Kwok, Gerald Nepom, Mikael Knip, Olli Simell, and Helena Reijonen. Gad65-and proinsulin-specific cd4+ t-cells detected by mhc class ii tetramers in peripheral blood of type 1 diabetes patients and at-risk subjects. *Journal of autoimmunity*, 25(3):235–243, 2005.
- [44] Joseph T Opferman, Bertram T Ober, and Philip G Ashton-Rickardt. Linear differentiation of cytotoxic effectors into memory t lymphocytes. *Science*, 283(5408):1745–1748, 1999.
- [45] M Pietropaolo and GS Eisenbarth. Autoantibodies in human diabetes. *Current directions in autoimmunity*, 4:252–282, 2001.
- [46] F Pociot and MF McDermott. Genetics of type 1 diabetes mellitus. *Genes and immunity*, 3(5):235–249, 2002.

- [47] Gareth O Roberts and Jeffrey S Rosenthal. Examples of adaptive mcmc. *Journal of Computational and Graphical Statistics*, 18(2):349–367, 2009.
- [48] AJ Schuerwegh, LS De Clerck, CH Bridts, and WJ Stevens. Comparison of intracellular cytokine production with extracellular cytokine levels using two flow cytometric techniques. *Cytometry Part B: Clinical Cytometry*, 55(1):52–58, 2003.
- [49] Jennifer E Smith-Garvin, Gary A Koretzky, and Martha S Jordan. T cell activation. *Annual review of immunology*, 27:591, 2009.
- [50] Andrea K Steck and Marian J Rewers. Genetics of type 1 diabetes. *Clinical chemistry*, 57(2):176–185, 2011.
- [51] Katinka Stoffels, Lutgart Overbergh, Annapaula Giulietti, Ahmad Kasran, Roger Bouillon, Conny Gysemans, and Chantal Mathieu. Nod macrophages produce high levels of inflammatory cytokines upon encounter of apoptotic or necrotic cells. *Journal of autoimmunity*, 23(1):9–15, 2004.
- [52] Jordan Sugarman, Sue Tsai, Pere Santamaria, and Anmar Khadra. Quantifying the importance of pmhc valency, total pmhc dose and frequency on nanoparticle therapeutic efficacy. *Immunology and cell biology*, 91(5):350–359, 2013.
- [53] Charles D Surh and Jonathan Sprent. T-cell apoptosis detected in situ during positive and negative selection in the thymus. *Nature*, 372(6501):100–103, 1994.
- [54] Charles D Surh and Jonathan Sprent. Homeostatic t cell proliferation how far can t cells be activated to self-ligands? *The Journal of experimental medicine*, 192(4):F9–F14, 2000.
- [55] Yuri Sykulev, Anders Brunmark, Theodore J Tsomides, Shigeki Kageyama, Michael Jackson, Per A Peterson, and Herman N Eisen. High-affinity reactions between antigen-specific t-cell receptors and peptides associated with allogeneic and syngeneic major histocompatibility complex class i proteins. *Proceedings of the National Academy of Sciences*, 91(24):11487–11491, 1994.
- [56] Sarah A Tersey, Yurika Nishiki, Andrew T Templin, Susanne M Cabrera, Natalie D Stull, Stephanie C Colvin, Carmella Evans-Molina, Jenna L Rickus, Bernhard Maier, and Raghavendra G Mirmira. Islet β -cell endoplasmic

reticulum stress precedes the onset of type 1 diabetes in the nonobese diabetic mouse model. *Diabetes*, 61(4):818–827, 2012.

- [57] John A Todd. Etiology of type 1 diabetes. *Immunity*, 32(4):457–467, 2010.
- [58] Jacqueline D Trudeau, Jan P Dutz, Edith Arany, David J Hill, Warren E Fieldus, and Diane T Finegood. Neonatal beta-cell apoptosis: a trigger for autoimmune diabetes? *Diabetes*, 49(1):1–7, 2000.
- [59] Sue Tsai, Afshin Shameli, Jun Yamanouchi, Xavier Clemente-Casares, Jinguo Wang, Pau Serra, Yang Yang, Zdravka Medarova, Anna Moore, and Pere Santamaria. Reversal of autoimmunity by boosting memory-like autoregulatory t cells. *Immunity*, 32(4):568–580, 2010.
- [60] Henrique Veiga-Fernandes, Ulrich Walter, Christine Bourgeois, Angela McLean, and Benedita Rocha. Response of naive and memory cd8+ t cells to antigen stimulation in vivo. *Nature immunology*, 1(1):47–53, 2000.
- [61] Charles F Verge, Roberto Gianani, Eiji Kawasaki, Liping Yu, Massimo Pietropaolo, H Peter Chase, George S Eisenbarth, and Richard A Jackson. Prediction of type 1 diabetes in first-degree relatives using a combination of insulin, gad, and ica512bdc/ia-2 autoantibodies. *Diabetes*, 45(7):926–933, 1996.
- [62] AD Wells, H Gudmundsdottir, and LA Turka. Following the fate of individual t cells throughout activation and clonal expansion. signals from t cell receptor and cd28 differentially regulate the induction and duration of a proliferative response. *Journal of Clinical Investigation*, 100(12):3173, 1997.
- [63] Yajun Zhou and Xiaowei Zhuang. Kinetic analysis of sequential multistep reactions. *The Journal of Physical Chemistry B*, 111(48):13600–13610, 2007.